

MASTER THESIS

Towards An Engineering Approach of Pool Fire Modelling with CFD

Jen-Wei(Luke) Liu

Faculty of Engineering Technology
Department of Thermal and Fluid Engineering

EXAMINATION COMMITTEE

Dr. Ir. J.B.W. Kok

Dr. S. Hajimolana

Dr. Ir. R. Hagmeijer

Jacques Vermeiden, M.Sc. (external member)

Khoi Vu, M.Sc. (external member)

August 26th 2020

UNIVERSITY OF TWENTE.

Abstract

The purpose of this project is to investigate a road towards an engineering approach of modelling pool fires with CFD. Modelling pool fires with CFD is challenging in terms of computational intensity. This project aims to investigate an engineering approach to the issue, meaning that attention will be placed on generating conservative results within a timely manner. The project starts with examining the most appropriate computer models for modelling pool fires. Multiple simulations are conducted and compared to published data for this purpose. The steady diffusion flamelet model is determined to be the most appropriate combustion model for this project in terms of practicality. After determining the most appropriate combustion model to use, a short comparison is done between the HE soot model and the Moss-Brookes-Hall soot model in terms of amount of soot produced, and in terms of effect on radiation. The purpose of this is to see how the completely empirical-based HE model behaves compared to the more theoretical-based Moss-Brookes-Hall model. The results show that the HE model has great potential and more investigation regarding the HE model is worthwhile. Finally, the mesh resolution study is carried out. In this study, the non-dimensional expression for mesh resolution, published by the National Institute of Standards and Technology, serves as the practical starting point. From experience, it is already known that this expression is only applicable to areas with no large gradients, in other words, with no flame. This project aims to derive a more general meshing approach from the starting point, and to start the investigation of whether the new approach can be applied to pool fires with different configurations. Five simulations with the same configuration but with different mesh resolutions are conducted in this study. The cell size used is compared to the macro length scale of turbulence to ensure that the turbulences are being resolved correctly in the domain. Analysis shows a good match between the mesh resolution and the macro length scale of turbulence, except in the limited region of flame surface. Nevertheless, results generated by different mesh resolution show good consistency. This demonstrates that, even with turbulences close to the combustion surface not entirely resolved, the results produced should be within an acceptable range of accuracy and will suffice for engineering purposes. The work done in the project uncovered a number of areas where investigation and additional validation would be useful.

Table of Contents

Abstract.....	i
Table of Figures	v
Nomenclature.....	vii
Acronyms.....	vii
Symbols	vii
1. Introduction.....	1
1.1 Background information	1
1.2 Problem statement and research objectives.....	1
1.3 Approach.....	2
2. Background information on pool fires.....	4
2.1 Definition of a pool fire	4
2.2 Characterization of pool fire.....	4
2.2.1 Flame height	4
2.2.2 Puffing frequency.....	5
2.2.3 Heat release rate.....	5
3. Theoretical components involved in pool fire modelling	7
3.1 Mesh resolution and the non-dimensional expression given by NIST as a starting point.....	7
3.2 Discretization.....	7
3.2.1 Spatial discretization	7
3.2.2 Temporal discretization.....	8
3.2.3 Angular discretization	8
3.3 A textbook case of nonpremixed combustion	9
3.4 Physical models	10
3.4.1 Flow models: RANS vs. LES	10
3.4.2 Combustion models.....	10
3.4.3 Radiation model.....	11
3.4.4 Soot model.....	12
3.5 Judging convergence.....	12
3.6 Judging safety distance from radiation contours	13
3.7 General procedures for modelling	14
3.8 Boundary and initial conditions used in simulations	15
4. Comparison of combustion models	17
4.1 Simulation setup	17
4.2 Unsteady Diffusion Flamelet model (UDF).....	18
4.3 Eddy Dissipation Concept model (EDC).....	19

4.4 Chemical Equilibrium model (CE) vs. Steady Diffusion Flamelet model (SDF).....	20
4.5 Results comparison among experiment, CE, and SDF	21
4.6 Planck Mean Absorption Coefficient (PMAC)	24
4.7 CE model with the user defined function.....	24
4.8 Conclusion from the combustion models.....	28
5. Comparison of soot models.....	30
5.1 Simulation setup	30
5.2 Theory of the soot model developed by Huygens Engineers (HE).....	31
5.3 Results of Moss-Brookes-Hall (MBH) model vs. HE model.....	32
5.4 Conclusion from soot models comparison	36
6. Mesh resolution study.....	38
6.1 Simulation setup	38
6.1.1 Configuration.....	38
6.1.2 Mesh.....	38
6.2 Results from the mesh resolution study	40
6.3 Examining macro length scale of turbulence	44
6.4 Results from examining macro length scale of turbulence	44
6.5 Further mesh refinement	45
6.6 Results from further mesh refinement.....	47
6.7 Conclusion from mesh resolution study.....	50
7. Conclusion	52
7.1 Comparison of combustion models	52
7.2 Comparison of soot models.....	52
7.3 Mesh resolution study	52
8. Discussion and recommendations	53
References.....	55
Appendix A. Theoretical background of computer models.....	58
A.1 Discretization.....	58
A.1.1 Spatial discretization	58
A.1.2 Temporal discretization: bounded second-order implicit time integration.....	60
A.2 LES simulation and the Wall-Adapting Local Eddy-Viscosity (WALE) model.....	60
A.3 The probability density function (PDF)	61
A.4 Chemical equilibrium model	62
A.5 Steady diffusion flamelet model.....	63
A.6 Eddy-dissipation concept model.....	65
A.7 Discrete ordinates model.....	66
A.8 Weighted sum of gray gas model.....	67

A.9 Moss-Brookes-Hall model.....	67
Appendix B. Code of user defined function	70
B.1 Hooking PMAC of methanol.....	70
B.2 The HE model.....	71

Table of Figures

Figure 1: Illustration of flame height fluctuations.....	4
Figure 2: Control angle overhang with (a)4x4 (b)5x5 (c)6x6 solid angles.....	9
Figure 3: Average temperature over time at location 0-0-2.....	13
Figure 4: Judging safety distance from radiation contour.....	13
Figure 5: Radiation contour from different moment in time.....	14
Figure 6: Boundary conditions for the domain	16
Figure 7: Boundary conditions for the pool and tanks.....	16
Figure 8: Domain setup for combustion models comparison	17
Figure 9: Grid used for the combustion models comparison	18
Figure 10: Simulation stopped at different number of iterations in RANS	19
Figure 11: Temperature contour produced by the EDC model, in RANS	19
Figure 12: Location of sampling in the CE vs. SDF comparison.....	20
Figure 13: Contour of scalar dissipation rate, SDF model.....	21
Figure 14: Heat of reaction, CE vs. SDF	21
Figure 15: Plot of mean radiation sampled at $z=0.303$ m, CE vs. SDF	22
Figure 16: Plot of mean temperature sampled along the centerline, CE vs. SDF	22
Figure 17: Plot of mean temperature sampled at $z=0.033$ m, CE vs. SDF	22
Figure 18: Plot of mean temperature sampled at $z=0.303$ m, CE vs. SDF	23
Figure 19: Plot of mean temperature sampled at $z=0.603$ m, CE vs. SDF	23
Figure 20: PMAC of (a) CO ₂ and H ₂ O (b) methanol	24
Figure 21: Heat of reaction, CE, SDF, and CE with user defined function	25
Figure 22: Plot of mean radiation sampled at $z=0.303$ m, CE, SDF, and CE with user defined function	25
Figure 23: Plot of mean temperature sampled along centerline, CE, SDF, and CE with user defined function.....	26
Figure 24: Plot of mean temperature sampled at $z=0.033$ m, CE, SDF, and CE with user defined function.....	26
Figure 25: Plot of mean temperature sampled at $z=0.303$ m, CE, SDF, and CE with user defined function.....	26
Figure 26: Plot of mean temperature sampled at $z=0.603$ m, CE, SDF, and CE with user defined function.....	27
Figure 27: Mass fraction of O ₂	27
Figure 28: Domain setup for soot models comparison	30
Figure 29: Temperature contour from the MBH model.....	32
Figure 30: Temperature contour from the HE model	33
Figure 31: Soot volume fraction generated by the MBH model	33
Figure 32: Soot volume fraction generated by the HE model, with different soot particle density	33

Figure 33: Plot of mean temperature sampled along the centerline, MBH vs. HE	34
Figure 34: Plot of mean temperature sampled at $z=1$ m, MBH vs. HE	35
Figure 35: Plot of mean temperature sampled at $z=3$ m, MBH vs. HE	35
Figure 36: Plot of mean temperature sampled at $z=5$ m, MBH vs. HE	35
Figure 37: Plot of mean radiation sampled at $z=2$ m, MBH vs. HE.....	36
Figure 38:Plot of mean radiation sampled at $z=2$ m zoomed in, MBH vs. HE.....	36
Figure 39: Pool and tanks configuration.....	38
Figure 40: (a) domain setup (b) grid setup for the mesh resolution study	39
Figure 41: Temperature contour of (a)1x (b)1.1x (c)1.3x (d)0.9x mesh	41
Figure 42: Plot of mean temperature sampled along the centerline, four sets of mesh	41
Figure 43: Plot of mean temperature sampled at $z=0.3$ m, four sets of mesh	41
Figure 44: Plot of mean temperature sampled at $z=1$ m, four sets of mesh	42
Figure 45: Plot of mean temperature sampled at $z=3$ m, four sets of mesh	42
Figure 46: Plot of mean temperature sampled at $z=5$ m, four sets of mesh	42
Figure 47: Plot of mean radiation sampled at $z=0.3$ m, four sets of mesh.....	43
Figure 48: Plot of mean radiation sampled at $z=0.3$ m zoomed in, four sets of mesh.....	43
Figure 49: Macro length of turbulence in the domain	44
Figure 50: Temperature contour, mesh resolution study in RANS	45
Figure 51: Attempted mesh resolution for further mesh refinement (units in mm)	46
Figure 52: Mesh resolution used for further mesh refinement (units in mm)	46
Figure 53: Temperature contour of the further refined mesh.....	47
Figure 54: Plot of mean temperature sampled along the centerline, with 1R mesh	47
Figure 55: Plot of mean temperature sampled at $z=0.3$ m, with 1R mesh	48
Figure 56: Plot of mean temperature sampled at $z=1$ m, with 1R mesh.....	48
Figure 57: Plot of mean temperature sampled at $z=3$ m, with 1R mesh.....	48
Figure 58: Plot of mean temperature sampled at $z=5$ m, with 1R mesh.....	49
Figure 59: Plot of mean radiation sampled at $z=0.3$ m, with 1R mesh.....	49
Figure 60: Plot of mean radiation sampled at $z=0.3$ m zoomed in, with 1R mesh.....	50
Figure 61: Illustration of discretization of a scalar transport equation	59
Figure 62: Illustration of a control volume consisting of both upstream and downstream.....	59
Figure 63: Illustration of probability density function.....	62
Figure 64: Stoichiometric mixture surface of a turbulent jet diffusion flame.....	64
Figure 65: User defined function for adding PMAC of methanol.....	70
Figure 66: User defined function for the HE model	71

Nomenclature

Acronyms

CE	Chemical Equilibrium
CFD	Computational Fluid Dynamics
DNS	Direct Numerical Simulation
DO	Discrete Ordinates
EDC	Eddy Dissipation Concept
HE	Huygens Engineers
LES	Large Eddy Simulation
MB	Moss-Brookes
MBH	Moss-Brookes-Hall
NIST	National Institute of Standards and Technology
PDF	Probability Density Function
PMAC	Planck Mean Absorption Coefficient
RANS	Reynolds-Averaged Navier-Stokes
RTE	Radiative Transfer Equation
SDF	Steady Diffusion Flamelet
SGS	Sub-Grid Scale
TCI	Turbulence Chemistry Interaction
UDF	Unsteady Diffusion Flamelet
URF	Under Relaxation Factors
WALE	Wall Adapting Local Eddy Viscosity
WSGGM	Weighted Sum of Grey Gas Model

Symbols

a_s	Absorption coefficient for soot	1/m
a_g	Absorption coefficient for gas	1/m
C_p	Thermal capacity	kJ/kg-K
Γ_φ	Diffusion coefficient for φ	m ² /s
δx	Nominal size of a mesh cell	m
D	Diameter of the fire	m

D^*	Characteristic fire diameter	m
ε	Rate of dissipation	m^2/s^3
ε_m	Emissivity	-
f	Puffing frequency	Hz
f_i	Elemental mass fraction of element i	-
$f_{i,OX}$	Elemental mass fraction of element i in the oxidizer	-
$f_{i,fuel}$	Elemental mass fraction of element i in the fuel	-
G	Gibbs energy	J
g	Gravitational force	m/s^2
H	Enthalpy	J
H_f	Flame height	m
$H_{c,eff}$	Heat of combustion	kJ/kg
I	Radiation intensity	W/sr
L	Non-dimensional mesh expression	-
Le_i	Lewis number	-
L_R	Macro length scale of turbulence	m
k	Turbulent kinetic energy	m^2/s^2
κ	Von Karman constant	-
λ_i	Lagrangian multipliers	-
\dot{m}	Mass loss rate	$kg/m^2\cdot s$
N	Soot particle number density	$Particle/m^3$
n	Refractive index	-
ζ^*	Length scale of fine scale	m
ρ	Density	kg/m^3
$\overline{S_{ij}}$	Deformation tensor for the resolved domain	-
s	Path length	m
σ	Stefan-Boltzmann constant	$W/m^2\cdot K^4$
σ_s	scattering coefficient	$1/m$
T	Temperature	K
τ^*	Time scale of fine scale	s
τ_{ij}	Subgrid stress tensor	-
μ_j	Chemical potential (Gibbs free energy) per kg-mole of species j	J

μ_t	Subgrid scale turbulent viscosity	m^2/s
V	Cell volume	m^3
v	Volume fraction	-
ν'	Stoichiometric coefficient	-
W	Molecular weight	kg/kmol
Ω	Solid angle	sr
\dot{Q}	Heat release rate of fire	kW
χ	Scalar dissipation rate	1/s
Y	Mass fraction	-
Y_i^*	Fine scale mass fraction	-
Z	Mixture fraction	-

1. Introduction

1.1 Background information

This project initiated when Huygens Engineers was approached by a customer in September 2018, who was interested in exploring the possibilities of pool fire simulation. Huygens Engineers was commissioned to simulate the radiation contour with CFD in case of a pool fire occurring at an ethanol storage complex in North Holland. The storage complex is comprised of a large number of tanks, contained within an enclosed area by walls.

The main reason why the customer initiated this investigation was because of a fire safety regulation newly introduced in 2018, which requires any company that is operating a fuel storage complex to prove that, in case of a large scale pool fire, the responding fire brigade would be able to handle the incident safely. If large scale pool fires cannot be safely handled by the firefighting personnel, new fire-extinguishing infrastructures must be installed on site, with far-reaching operational consequences for the company. The conventional analytical prediction methods, most often based on empirical data from small scale pool fires, were deemed of limited predictive capability when applied to large scale pool fires with complex geometry, also by the scientific advisor of the governing safety agency. Without predictive model, this leaves the fire-fighting personnel in potentially great danger when dealing with large scale pool fire, which is why the possibility of modelling pool fires with CFD is being sought. Since the ultimate goal is to protect the safety of firefighters with CFD modelling, the capability of CFD needs to first be proven before it can be applied to the industry.

This project aims for being the first step toward investigating the issues mentioned above. Industrial pool fires usually occur on very large scale and with a complex geometry, which is difficult and time-consuming to model if accurate data were to be obtained. The customer wishes to pursue practical approaches to obtain answers. This is why this project aims at outlining an engineering approach over a scientific approach. In an engineering approach, the focus is placed on obtaining conservative results rather than accurate results, using existing scientific methods rather than developing new methods, and this needs to be done within a realistic time frame.

This project was completed at Huygens Engineers, with Huygens' facilities and technical support. Experiences gained by Huygens from the previous project made an immense contribution to this project.

1.2 Problem statement and research objectives

Many questions remain unanswered regarding the accuracy of pool fire modelling, more generally, regarding scaling behavior of pool fires. These questions range from the fundamental aspects of a pool fire such as the different behaviors between small and large scale pools, the effect of structures and the complexity of structures within the pool, soot formation, radiation, all the way to difficulties encountered in simulation such as the differences in combustion models, soot models, mesh resolution influence, domain size influence...etc. While building upon a fundamental understanding of a pool fire, this report aims to focus on three questions regarding pool fire simulation. Namely,

1. What are the realistic options for combustion models and what is the level of validity they offer?

Multiple combustion models exist within CFD, and several are available within the commercial software ANSYS Fluent. However, the complexity of these models ranges quite dramatically and different assumptions are made in these different models. Some models replicate many detailed aspect that occur within the chemistry of combustion, and may produce results that are accurate in given

situations, but their drawback is the rapid increase in calculation time. For practical reasons, results must be produced in a timely manner, yet the quality of results must remain meaningful. Aspects of this trade-off have been investigated in this study.

2. What are the realistic approaches to soot formation prediction?

Soot influences radiation dramatically, yet soot formation is a complex phenomenon that potentially requires substantial calculation time on its own. Here, again, the study focuses on models that can produce useful results within an industrial perspective. Among the large number of existing soot models, a few soot models are available in Fluent. This report aims to compare one of the precursor-based soot models to the empirical reaction-progress-based soot model developed by Huygens Engineers. Two simulations will be conducted for this topic and the results will be compared to published data.

3. Can a suitable meshing approach be derived from the background work published by NIST in the FDS user's manual as a starting point?

Determining the appropriate grid size for simulating pool fires is a great challenge. The National Institute of Standards and Technology (NIST) has published a non-dimensional expression for the recommended grid resolution for fire simulations. However, from previous experiences, it is already known that the resulted meshes are too coarse locally. This project wishes to investigate the possibility of establishing a more suitable approach that builds on the existing work. Another question that follows is whether this approach can be applied to pool fires with structures inside [1]. This project also started the investigation of this question. The non-dimensional expression can be found in chapter 3.1 of this report.

1.3 Approach

This report starts by giving a brief overview of pool fires and some background regarding CFD modelling in chapter 2 and 3, respectively. In chapter 2, the definition of a pool fire is given, along with some other variables that quantify a pool fire. The goal of this chapter is not to give an extensive description of a pool fire. Rather, only those variables that are most relevant and are used extensively in the modelling work are introduced. In chapter 3, all the elements of modelling a pool fire are briefly explained. The non-dimensional expression for mesh resolution, which is the cornerstone of the mesh resolution study in chapter 6, is given here. A brief qualitative description of all the computer models used is given in chapter 3. Methods used to interpret the generated results are also given in this chapter. In the end, some tips are given regarding how to simulate a pool fire, since this task is not always straightforward.

Before starting the investigation of the stated objectives, one combustion model must be chosen. Multiple combustion models are available in ANSYS Fluent, and deciding which one to use requires some effort itself. Chapter 4 of the report describes the process of picking out the most appropriate combustion model. Numerous simulations were conducted in order to determine the advantages and disadvantages of each model. The results generated are compared to published data when possible. Pros and cons of these models are briefly discussed. A more complete theoretical background of these models are provided in Appendix A. A quick conclusion will be drawn before moving onto the main objectives of the project.

Chapter 5 aims to answer the second objective of the report. Two simulations were conducted to test the behavior of two different soot models. The two soot models tested are the HE model, developed by Huygens Engineers, and the Moss-Brookes-Hall model, which is available in Fluent. The simulations are set up the same way as the experimental setup, with some simplifications to save

computation time. The results are compared to published data and also to each other. This is to check the predicting capabilities of both models, and also to check if the two models agree with each other. This is important because the HE model was only recently developed and its capability has not been verified. HE model is the most straightforward model in comparison to all the models available in Fluent, both in terms of formulation and execution. If the HE model yields acceptable results, it could potentially save a lot of effort in modelling for any future projects.

The aim of chapter 6 is to examine the non-dimensional expression for mesh resolution published by NIST and to derive a new approach from it. This project examines the case where there are four units of fuel containers inside a pool fire. A total of five simulations will be conducted with five different mesh resolution. Ideally, the coarser the mesh that is required the better, because this will save a large amount of computation time. The results of these simulations will only be compared among themselves because no experimental data could be found where pool fires are burned with structures inside.

After the results of all the simulations are presented, some discussion and recommendations will be offered. In a way, this report does not and cannot offer any conclusive results. Predicting the behavior of pool fire with CFD is a field that still requires much more investigation, especially large scale pool fires and pool fires with structures inside. Rather than drawing a conclusion, this report offers directions and recommendations for further research.

2. Background information on pool fires

2.1 Definition of a pool fire

A pool fire occurs when combustible liquid is accumulated to form a pool and this pool is ignited. This is a broad definition and pool fires can in fact take many forms. Pool fires can take place both on top of the surface of liquid or of ground. Large scale pool fires are often disastrous and difficult to control [2]. The fire that broke out in Jaipur, India in 2009 is a good example of a disastrous pool fire. This fire broke out at a facility that consists of 12 large fuel storage tanks. Nearly one hundred thousand cubic meter of fuel was burned [3]. The fire burned for 11 days after the outbreak [4].

A pool fire is a diffusion flame, meaning that the fuel and the oxidizer are not mixed before they come to the reaction zone. The process of mixing must happen quick enough in order to sustain the combustion [5]. A pool fire sustains itself by feeding the vaporized fuel to the fire. The fuel vaporizes because of the thermal radiation it receives from the flame. The vaporized fuel is mixed with the oxygen from the surrounding, then ignited by the existing flame. It is this repeating process that sustains the pool fire.

2.2 Characterization of pool fire

Pool fire is a special form of combustion which exhibits many unique characteristics. Some of its characteristics that are most relevant to this project are introduced in this section. These characteristics are crucial for determining many factors of the simulations such as many of the inputs of the simulation, the size of the domain...etc. Furthermore, these characteristics are also important for judging the convergence of the simulation.

2.2.1 Flame height

Determining the size of domain for a pool fire simulation is challenging. No guideline yet exists to indicate how large the domain should be for this type of simulation. Hence, it is extremely helpful if the flame height is known before the modelling starts. In this report, the size of the domain is merely dependent on the diameter of the pool, the flame height, and the best of judgement.

Pool fires have a pulsating behavior. As the flame develops, the total height of the flame elongates. The elongation occurs to a certain degree, then a plume of hot gases would rise and detach from the main body of the flame. After the detachment, the height of the flame is reduced to its original state, then the flame develops again and the process repeats. This phenomenon is illustrated in Figure 1 below.

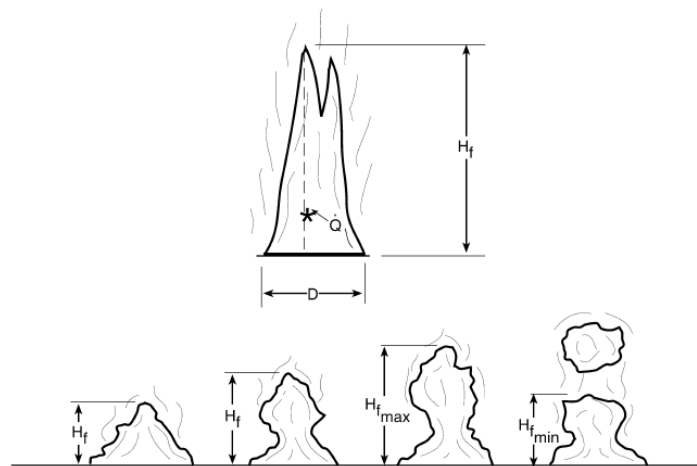


Figure 1: Illustration of flame height fluctuations

Because of this pulsating behavior, the height of flame can only be estimated. The expression for determining the flame height is given below [6],

$$H_f = 0.235\dot{Q}^{\frac{2}{5}} - 1.02D \quad (1)$$

where

H_f = flame height [m]

\dot{Q} = heat release rate of the fire [kW]

D = diameter of the fire [m]

The flame height prediction is also important when the mesh needs to be refined in certain regions in the model. For all the simulations that are presented in this report, the mesh is refined where there is flame to account for the large gradients. This would be difficult if the expression above were not available. If the expressions were not available, then the flame height needs to be determined directly from the simulation, which is also difficult since the flame has a pulsating behavior.

2.2.2 Puffing frequency

Another important factor regarding pool fire is the puffing frequency of the flame. Pool fires are unsteady by nature and are constantly pulsating. The expression for determining the puffing frequency is given as [6]:

$$f = 1.5D^{-0,5} \quad (2)$$

where the frequency is given in hertz and D again stands for the diameter of the pool, given in meter.

This factor is particularly important for judging how many seconds of data should be collected. For example, for the mesh resolution study presented in chapter 6, it is determined that five cycles of data should be collected for each simulation. To determine how many seconds of data this is, the diameter of the pool, 2 meter, is plugged into the expression above, then the result is converted from hertz to seconds. This result would be one cycle of data. Multiplying this result by 5 would give roughly 4.7 seconds of data. Of course, collecting this many cycles of data does not mean that the solution has converged. This still needs to be judged from the behavior of the flow field. However, knowing the puffing frequency is a good way to estimate when is a good point to stop the simulation and how long the simulation will take.

2.2.3 Heat release rate

The \dot{Q} in Eq. 1 above stands for the total heat release rate, which is expressed as [6]

$$\dot{Q} = \dot{m}\Delta H_{c,eff} \quad (3)$$

where

\dot{m} = mass loss rate (kg/m²-s)

$\Delta H_{c,eff}$ = heat of combustion (kJ/kg)

the mass loss rate measures how much in weight is the fuel lost while it is burning, and the heat of combustion measures how much energy is released when one unit mass of fuel is burned.

Since it is difficult to model the fuel lost during a combustion, the fuel source is modelled as a constant fuel inflow in all the simulations presented. The mass inflow of fuel is the product of the mass loss rate and the area of the pool. Multiplying this by the heat of combustion would yield the total heat release rate of the pool fire. The total heat release rate is another important parameter that could be used

to check the validity of the simulation. The mass loss rate and heat of combustion are both experimental data which were taken from the SFPE Handbook [6].

3. Theoretical components involved in pool fire modelling

All the aspects regarding the modelling of a pool fire are described in this chapter. First, the non-dimensional expression for mesh resolution is given in this chapter. This expression is the cornerstone of the study conducted in chapter 6. Next, a short description of the schemes used for discretization is given. This is essential to any CFD modelling work. A short description of all the models is given following the section for discretization. This includes the description for the combustion models, the soot models, and the radiation model. Some procedures used to judge the convergence of the flow field and to judge the safety distance from the results produced are also mentioned. Finally, some tips are offered regarding the overall procedure of modelling a pool fire.

3.1 Mesh resolution and the non-dimensional expression given by NIST as a starting point

In their publication, the Fire Dynamics Simulator User's Guide, the NIST recommends the following non-dimensional expression for determining the appropriate mesh resolution when conducting pool fire simulations [1].

$$\frac{D^*}{\delta x} = L \quad (4)$$

where

$$D^* = \left(\frac{\dot{Q}}{\rho_{\infty} c_p T_{\infty} \sqrt{g}} \right)^{2/5} \quad (5)$$

D^* = characteristic fire diameter

\dot{Q} = total heat release rate [kW]

ρ_{∞} = air density [kg/m³]

C_p = air thermal capacity [kJ/kg-K]

T_{∞} = ambient air temperature [K]

g = gravitational force [m/s²]

dx = nominal size of a mesh cell

L = non-dimensional mesh expression

In the validation study sponsored by the U.S. Nuclear Regulatory Commission, L ranged from 4 to 16 [7]. This range will serve as a benchmark for this report.

From experiences gained from the previous project, it is already known that regions with large gradients require a much finer mesh than the recommended resolution. This report has two major aims. One, based on this expression, to derive a more general approach to meshing, and two, to investigate whether this new approach can be applied when there are objects inside the burning pool, which is often the case in reality.

3.2 Discretization

3.2.1 Spatial discretization

Mainly two schemes are used for the spatial discretization: the bounded central differencing scheme and the QUICK scheme. The momentum equation is calculated with the bounded central

differencing scheme. This scheme is second-order accurate and provides improved accuracy for LES simulation. The bounded central differencing scheme is developed based on the central differencing scheme. The central differencing scheme is known to produce unbounded solutions which can lead to issue with stability in the model. The bounded central differencing scheme is developed to correct this issue, hence is used here. Most of the other equations are solved with the QUICK scheme. This is because the QUICK scheme offers third-order accuracy [8]. These two schemes are explained in more details in Appendix A.1.1.

The radiation equation is the only equation discretized with the first-order upwind scheme in this project. This is an attempt to smooth out the unrealistic overhangs present in the radiation contour, as will be seen in chapter 3.6. The first-order upwind scheme assumes that the value for any field variable is the same throughout the cell. In other words, the face value in a cell is assumed to be the same as the value at the cell center. This is a coarse assumption, hence this scheme only offers first-order accuracy [8]. However, experiences from Huygens has shown that results generated by this scheme is not far off from a second-order scheme in the radiation contour from a practical point of view.

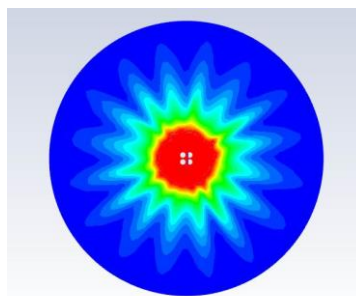
3.2.2 Temporal discretization

Since LES is used, the equations must be discretized in time. The bounded second-order implicit time integration method is used for all the LES simulations conducted. This scheme is frequently used for LES simulations. Essentially, it ensures the second-order accuracy, and at the same time provides better stability to the model by bounding the variables so that numerical errors are less likely to occur [9]. The mathematical formulation of this scheme is provided in Appendix A.1.2.

3.2.3 Angular discretization

For all the simulations presented in this report, a 4x4 solid angle is used. This means that each octant in the 4π angular space is discretized into 4x4 solid angles. This is a compromise made between the accuracy of the data and the computation time. In a research conducted by Ferng and Lin, it is stated that 6x6 solid angles are sufficient [10]. 5x5 solid angles were tested in this project. However, this resulted in calculation time more than two times longer than the simulation using 4x4 solid angles. Due to time constraint, the investigation was conducted with 4x4 solid angles. More information about the method of angular discretization can be found in the ANSYS theory guide [8].

The biggest drawback of using 4x4 solid angles is the control angle overhang that can clearly be seen in the radiation contour. This is demonstrated in Figure 2.



(a)

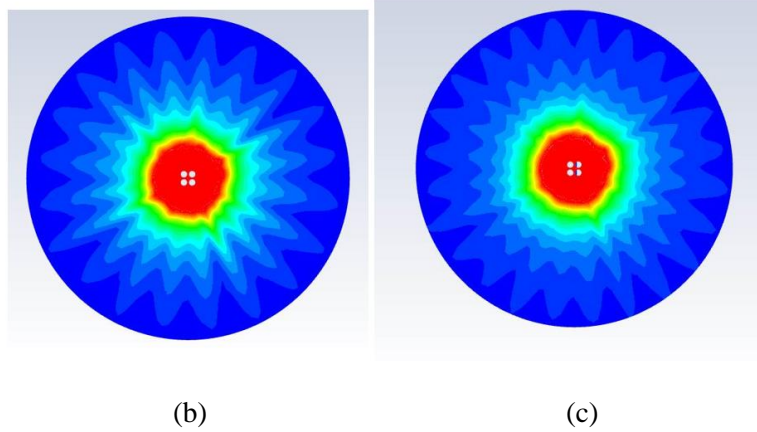


Figure 2: Control angle overhang with (a) 4x4 (b) 5x5 (c) 6x6 solid angles

As can be seen in Figure 2(a), a lower number of solid angles resulted in overhangs that are very obvious. The number of overhangs increased when the number of solid angles increased. It can also be seen that, the more the number of solid angles increases, these pointy overhangs start to be smeared out. However, it was determined that the errors generated by the 4x4 solid angles are acceptable for the purpose of this project.

3.3 A textbook case of nonpremixed combustion

Since the fuel and the oxidizer are not mixed before combustion, pool fire is categorized as nonpremixed combustion. In a pool fire, the thermal radiation released by the flame feeds back to the pool of fuel, gasifies the fuel, the fuel is mixed with the surrounding oxidizer, and the process of combustion continues. Pool fires are dominated by buoyancy, which is a major reason for its unsteady nature. Another name for nonpremixed combustion is diffusive combustion. This is because diffusion is the rate-controlling factor in this type of combustion. Compared to the chemical reactions, diffusion and convection, which are the two factors responsible for turbulent mixing, typically occur much slower. Hence, assuming infinitely fast chemistry is often acceptable for diffusive combustion [11].

The mixture fraction variable is an important variable used in nonpremixed combustion modelling to simplify the complicated chemical reactions involved. The mixture fraction is denoted Z in this report [8]. It is derived from the global reaction equation. After relating the mass fraction of the fuel and the oxidizer to the molecular weights and the stoichiometric mass ratio between oxygen to fuel, the combustion process could be represented by a single variable where the mass fraction of the fuel and oxidizer represent the burnt and unburnt state of the process [11]. The mixture fraction has the expression below

$$Z = \frac{f_i - f_{i,OX}}{f_{i,fuel} - f_{i,OX}} \quad (6)$$

where f_i represents the elemental mass fraction of element i and the subscript OX denotes the oxidizer. This expression is derived based on the assumption that the diffusion coefficient is the same for all the species. Through this variable, the atomic elements are conserved, hence reducing a complicated chemical problem down to a mixing problem. The difficulties of balancing the stiff equations associated with the chemical mechanisms could be avoided through this approach and significantly speed up the calculation time [8].

3.4 Physical models

Many computer models are tested or used throughout this project. Different models are needed to calculate different variables. This chapter offers short descriptions of all the models used. Their main functions and the main assumptions made in these models are mentioned. The theoretical background of these models is offered in Appendix A.

3.4.1 Flow models: RANS vs. LES

The main type of simulation used in this project is the large eddy simulation (LES). The Reynolds-averaged Navier-Stokes (RANS) simulation is only used in a couple occasions when the combustion model used is only compatible with RANS simulation, or when LES is posing too many difficulties.

From a practical point of view, in order to generate results in a timely manner, LES simulation is not preferred because of its long calculation time compared to RANS simulation. However, this isn't possible for this project due to the fact that pool fires are highly unsteady. In RANS simulation, the solutions are calculated using the time-averaged Navier-Stokes equations. As can be imagined, applying a time-averaged solution to an unsteady flow field does not yield accurate results. Although it is not the main aim of this project, RANS simulation was used in a small part of this project and very poor results were obtained, indirectly ruling out the possibility of conducting more simulations with RANS. LES simulation, on the other hand, does produce results at every time step in the flow field, hence being the more appropriate method for pool fire modelling. The subgrid-scale model (SGS) used in this project is the wall-adapting local eddy-viscosity model (WALE). More details about the LES simulation and WALE model can be found in Appendix A.2.

3.4.2 Combustion models

Multiple combustion models are tested in this report. This section aims to give a short description about each model used before the results are presented. The more detailed theoretical background of these models is offered in Appendix A.4 to A.9.

3.4.2.1 *Chemical equilibrium (CE) model*

The CE model, as its name has indicated, assumes all reactions are in chemical equilibrium. The model achieves this through the method of Gibbs energy minimization, which will be explained in more details in Appendix A.4. In this model, the complicated calculation regarding chemistry is reduced down to one variable, which is called the mixture fraction. This is a major advantage because solving the stiff equations of every chemical species is a very time-consuming task.

Another advantage of this model is that no Chemkin code is required. In terms of using the software, the Chemkin code is simply something to be loaded into the model. However, determining the right Chemkin code to use in fact requires some knowledge in the field of chemical reaction mechanisms. The mechanisms often turn out to be more complicated than expected, which could potentially mean longer calculation time, yet reducing the mechanisms is not an easy task and the reduced code is not always available. While not requiring the Chemkin code is an advantage, the drawback of this is that the user has less control over the mechanisms when desired.

3.4.2.2 *Steady diffusion flamelet (SDF) model*

Same as the CE model, the SDF model also uses the mixture fraction parameter to reduce the calculation regarding chemical reactions. The biggest difference between the CE and SDF model is that, while still assuming all reactions are fast chemistry, the SDF model takes the non-equilibrium effects

caused by aerodynamic strain into account. The model incorporates the aerodynamic effect by calculating the scalar dissipation rate [8]. More details of this model can be found in Appendix A.5.

The SDF model does require the Chemkin code input since the model does take the chemical mechanisms into account. This allows the user some more flexibility in tweaking the chemical mechanisms if the user wishes to.

3.4.2.3 Unsteady diffusion flamelet (UDF) model

The UDF model stands somewhat between the CE and SDF model mentioned above, and the EDC model which will be mentioned in the next section. Like the CE and SDF model, the UDF model also reduces the chemistry calculation. However, like the EDC model, it is able to predict the slow-forming species such as the gaseous pollutants during the process of combustion through a probability approach, without solving for the stiff conservation equations of each chemical species [8].

The ability to predict slow-forming species is a major advantage compared to all the other nonpremixed combustion models tested in this report because all the other models either treat the combustion as a process that is in chemical equilibrium or a process that is close to equilibrium. Such assumptions are not ideal when the presence of pollutants such as SO_x, NO_x, or soot plays a role in the investigation because these species are not formed in a chemical equilibrium condition. Since the presence of soot is a major factor of the radiation contour, the UDF model could potentially be very useful. However, the drawback of the UDF model is that the calculation is post-processed on a steady flow field. This is a major drawback because pool fires are highly unsteady by nature and never reach a steady state.

3.4.2.4 Eddy dissipation concept (EDC) model

The three models mentioned above all model pool fires through the mixture fraction approach. Pool fires can also be solved with the species transport equations. One of the model placed under the species transport and finite-rate chemistry category is the EDC model. The EDC model, unlike other models that utilize the mixture fraction parameter, takes the detailed chemical mechanisms into account and solves for the mass balance equations of all the species involved [8]. The EDC model is the most complete model in the sense that all chemical reactions on all different time scales are included in the calculation. The drawback is that solving for these stiff mechanisms is very expensive in terms of calculation time. Another reason why the EDC model is expensive to use is that it solves the chemistry on a certain time and length scale, which can both be very small in reality. More details about the EDC model can be found in Appendix A.6.

3.4.3 Radiation model

The discrete ordinates (DO) radiation model is used throughout this project. There are multiple radiation models available in Fluent. However, since it is not the main focus of this project to compare different radiation models, one model is used throughout in order to reduce the number of variables. The DO model was chosen because it is applicable to all optical thickness, which is an important factor since very clear and very sooty flames are both used in this project.

The DO model solves for the radiative transfer equation (RTE) for a finite number of vector direction \vec{s} , defined by the number of discrete solid angles. The DO model does this by transforming the RTE into a transport equation which solves for the radiation intensity in the global Cartesian system (x,y,z). This implies that the DO model solves for as many transport equations as there are vector direction \vec{s} , making it a computationally expensive model [8]. Details about this model can be found in Appendix A.7.

The weighted sum of grey gases model (WSGGM) is used throughout the project to calculate the emissivity of the gas. This model is a compromise between the oversimplifying gray gas model and other models that take into account the spectral information of gases, which are expensive [8]. For engineering problems, this model is computationally cheap and has shown decent accuracy. In Fluent, only CO₂ and H₂O are taken into account when calculating the emissivity [12]. Details about the WSGGM can be found in Appendix A.8.

3.4.4 Soot model

Two soot models are used and compared in this report. The first one is named the HE model because it is recently derived by Huygens Engineers. The HE model is completely empirical-based. There is published data available, listing how many grams of CO, CO₂, and soot is produced when one gram of fuel is burned. This data is available for many different types of fuel. The HE model predicts the amount of soot produced based on the assumption that CO and CO₂ both eventually turn into soot. The mathematical formulation of this assumption is rather straightforward, making this model easy to apply. One drawback of this model is that empirical data for pollutant formation isn't always available for the type of fuel used. This model is explained in more details in chapter 5.2.

The other model used, the Moss-Brookes-Hall (MBH) model, is more theoretical. The model assumes that the soot particles inception rate is eight times the formation rate of two-ringed (C₁₀H₇) and three-ringed (C₁₄H₁₀) aromatics, which are formed from the precursor species acetylene (C₂H₂), benzene (C₆H₆), and phenyl radical (C₆H₅). It takes into account the rate of nucleation, surface growth and oxidation when calculating the soot mass concentration. Details of this model can be found in Appendix A.9.

3.5 Judging convergence

Since pool fires are unsteady by nature, how to judge the convergence of these simulations is a major concern. The first method is to monitor the residuals of the simulation like all other CFD simulations. All the residuals should reach a certain value in each iteration. The second method used here is to monitor the average temperature at multiple locations in the flame over time. When the average temperature is plotted over time, it should more or less be constant.

For practical reasons, the simulations conducted were all planned to complete five cycles of pulsation. When the simulations have completed five cycles, the average temperature is plotted to judge the convergence of the mean. If the plot shows a straight line toward the end of data collection, then the simulation is deemed complete. If not, then the simulation must be continued. Multiple locations in the flame is monitored to ensure the quality of this judgement. An example is given below.

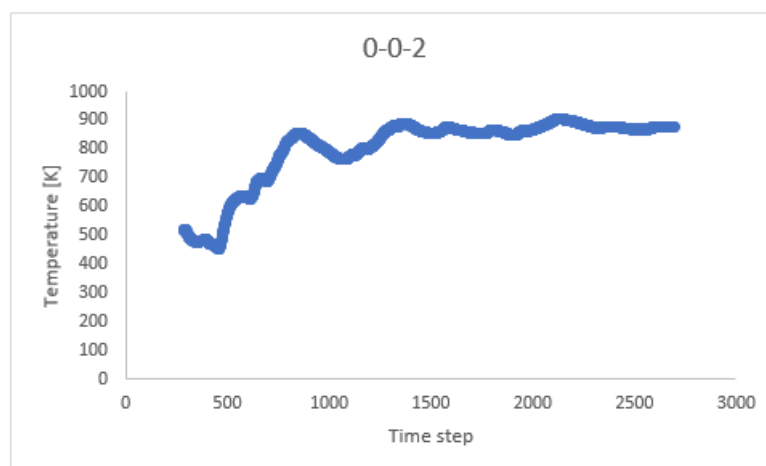


Figure 3: Average temperature over time at location 0-0-2

The mean temperature at the location 0-0-2 is plotted in Figure 3. This location is at the centerline of the flame, 2 meters above ground. As can be seen, at the beginning of data collection, the mean temperature is not stable. At about the 2200th time step, the mean temperature becomes constant. At this stage, it can be judged that the simulation has more or less converged for the mean, since the mean flame temperature at a certain location does not vary in large magnitude anymore. As can be seen, the data was not collected at the beginning of the simulation. This is because the flame takes some time to be started. During this period, the simulation itself is highly unstable. The data is not collected during this period so that the average data is not contaminated by the chaotic data generated by the start of the flame.

3.6 Judging safety distance from radiation contours

Although not one of the research objectives, one of the ultimate goals of modelling pool fires with CFD is to map the safety distance from a pool fire for the fire brigade. A good way to visualize this is through the radiation contours. However, because of the issues with the overhang mentioned above, pinpointing the exact safety distance is difficult. To be safe, it is better to consider the worst case scenario. This is to say to use the tip of the overhangs as a reference for the safety distance instead of the grooves between the overhangs or something in between. This is demonstrated in the figure below.

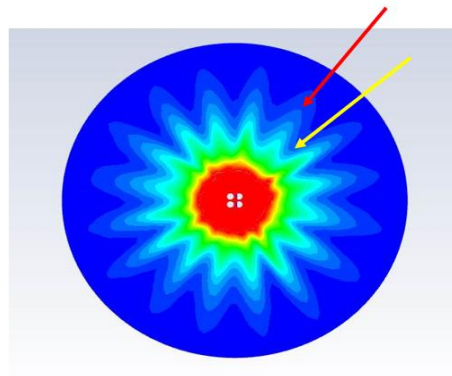


Figure 4: Judging safety distance from radiation contour

The red arrow points to the tip of the overhang, the yellow arrow points to the groove. Both arrows point to roughly the same radiation intensity. For the size of this domain, which is 30 meters in diameter, the difference may not be that large. However, if this were a much larger domain, the difference could be a couple of meters.

Another factor to take into account when viewing the radiation contour is the pulsating behavior of pool fires. Below are two radiation contours of the same flame, but at different moments in time.

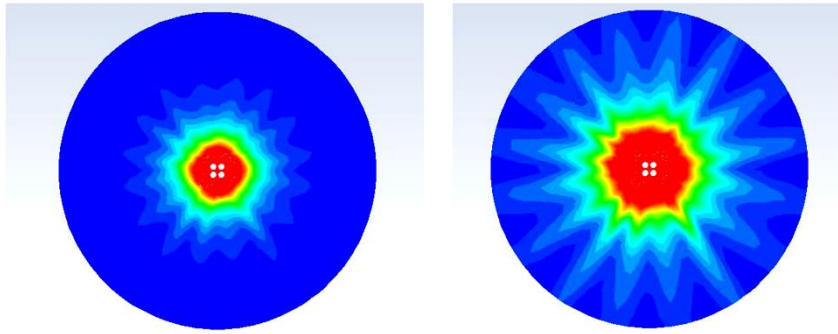


Figure 5: Radiation contour from different moment in time

This is a top view from the flame, with a height of 0,3 meters above ground. The pool shown in the figure is 2 meters in diameter, and the domain is 30 meters wide. The maximum value is set to 5 [kW/m²] in these contours. As can be seen, the contour varies quite dramatically. Because of the unsteady nature of pool fires, most often only the averaged value is checked. For example, when checking for the convergence of these simulations, the average temperature is checked, not the static temperature at different moment in time. This should not be the case when mapping safety distance from the radiation contours. The moment in time when the flame is emitting the most radiation should absolutely be an important factor when mapping the safety distance.

It can be seen that many uncertainties exist in the work of mapping safety distance. This is why, besides applying the safety precautions recommended above when judging a safety distance from the radiation contours, a safety factor should also be used. This could be done in different ways. The safety factor can be applied to the acceptable level of radiation, then to check the safety distance for this radiation intensity. Or, apply the safety factor directly to the safety distance. Since modelling pool fires with CFD is a field that still requires much investigation and a lot of uncertainties exist, a large safety factor may be needed.

It is not within the scope of this project to establish any guidelines for mapping out the safety distance from the CFD results. The purpose of this chapter is to simply point out some matters that have been noticed during the work of modelling. In fact, with the limited results produced so far, it is a long road ahead before any guidelines regarding safety can be established. The recommendations above should under no circumstances to applied for practical uses.

3.7 General procedures for modelling

Starting a pool fire in LES simulation requires some attention. No clear rules exist for this procedure. Some guidelines exist, but these guidelines are often ambiguous and the detail is different for pools with different configurations. The procedure described below is the procedure used in this project, which mainly comes from the experience of Huygens.

At the very beginning of the simulation, a large time step is used. For the diameter tested in this project (0,3-2,0 meters), 1 second is used as the initial time step size. Approximately five time steps are run with this time step size, with 20-25 iterations per time step. The under relaxation factors (URF) are set to default, or a little lower than the default value at this stage. Next, half of the initial time step size is used for approximately five time steps. The residuals are supposed to decrease when a smaller time step size is used. If this is not the case, the simulation should be returned to the state before the solution failed to converge, and the URF corresponding to the residual that is not decreasing, should be decreased. The time step size is decreased by a factor of two every time it is decreased. This process is repeated until the CFL number is approximately 1 or smaller everywhere in the flow field. For the grid sizes used

in this project, a time step size of 1 or 2 milliseconds are sufficient. During this process, many judgement calls have to be made. For the most part, five time steps are used. However, this largely depends on the behavior of the flow field. Depending on the pattern of the residuals, 10, 20, or even more time steps may be necessary to make sure that the solutions are converging. The number of iterations per time step is also a judgement call. When the solutions are converging correctly, but not quite reaching the satisfactory values, then the number of iterations could be increased. 30 iterations per time step is normally sufficient for this project.

The process described above could be a tedious process. When the duration of one time step is long, it also becomes a very time-consuming process. To save time, the computationally-intensive models are not turned on during this process, namely, the radiation and the soot models. The radiation model is turned on when the residuals have reached the appropriate values, and the soot model is turned on after the residual of radiation has reached its appropriate value. It normally takes longer for the radiation residual to stabilize. 50-100 time steps may be necessary when the number of cell counts is high in the model.

3.8 Boundary and initial conditions used in simulations

The boundary conditions of the simulations are illustrated below. Figure 6 shows the pool and tanks in the domain. There are no tanks present for the simulations conducted in chapter 4. Only simulations conducted in chapter 5 and 6 have tanks present in the pool.

The top of the boundary is modelled as a pressure outlet, while the boundary surrounding the domain is modelled as a pressure inlet. The choice of using pressure inlet instead of outlet at the surrounding of the domain is an attempt made to make the computer model more stable, as a model with only an outlet but no inlet may lead to instabilities. In fact, the pressure at both locations are set to atmospheric pressure, so the domain is modelled as if the pool is located in a windless open area. The area at the bottom of the domain but outside of the pool is modelled as a wall with no thickness. The same condition applies to the rim of the pool and the tanks. This simplification can be made because the heat transfer in the walls is of no interest to this project. Furthermore, it is assumed that the radiation emitted by these walls would be of negligible intensity.

The fuel inlet is modelled as a mass inflow. This is a major simplification made in this project. In reality, as the fuel burns, the level of fuel in the pool would decrease. However, how to model this phenomenon is yet unknown, hence the simplification must be made. The amount of inflow is calculated by taking the mass loss rate of a fuel, which is normally given in $[\text{kg}/\text{m}^2\text{-s}]$, and multiply it by the area of the pool. The physical meaning of this calculation is that the amount of fuel being supplied to the pool is the same amount of fuel being burned. The data of the mass loss rate of different types of fuel is taken from [13].

The flow fields are initialized with zero mixture fraction, zero velocity, atmospheric pressure, and at 300 [K]. This initial condition works well for all the models that use the mixture fraction variable. For the EDC model, the flow field was initialized with the correct percentage of oxygen in the air, and a small amount of oxygen and CO_2 . Without the small amount of fuel and CO_2 in the initial condition, the flame could not be started. The exact amount of fuel and CO_2 needed to start the fire is undetermined. A trial and error method was used in this project. Nevertheless, this method only worked for starting a fire in RANS simulation. How to start a fire with the EDC model in LES simulation is yet unknown. This will be discussed more in chapter 4.3.

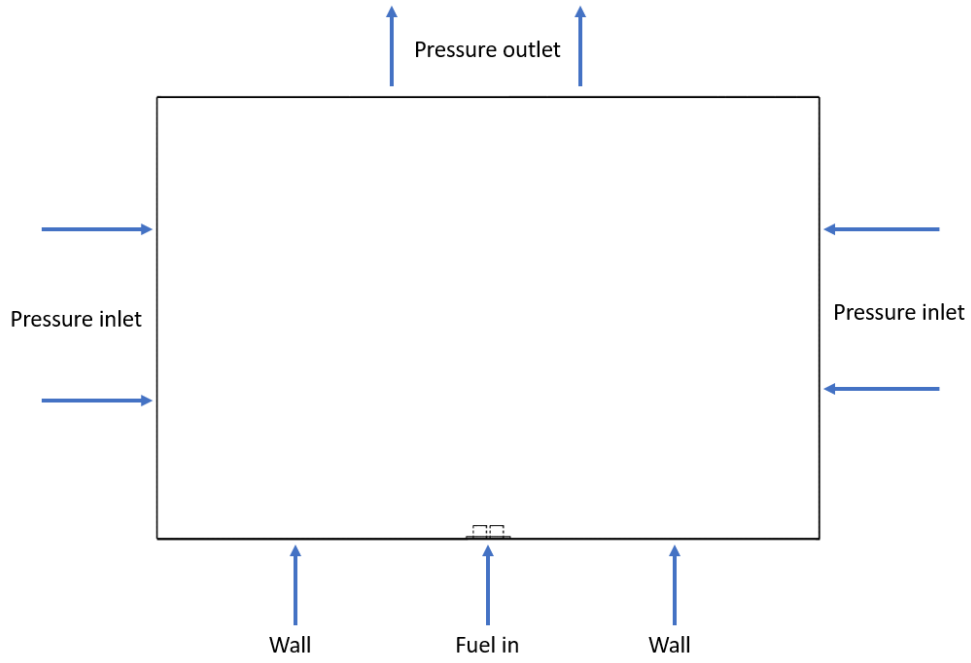


Figure 6: Boundary conditions for the domain

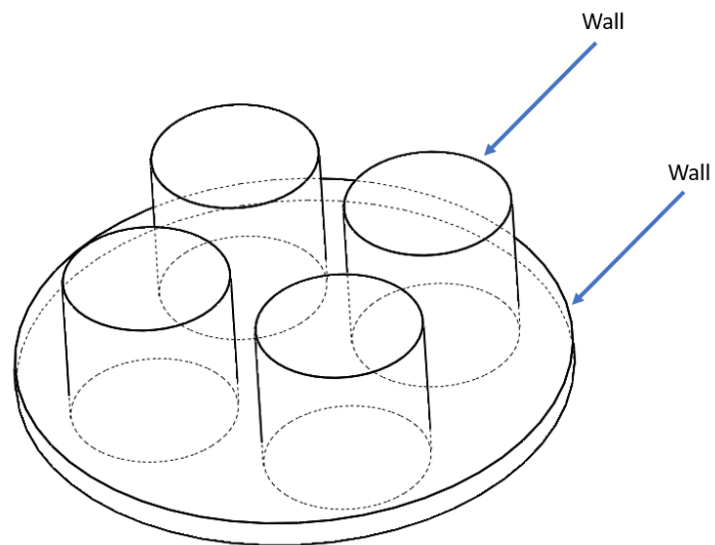


Figure 7: Boundary conditions for the pool and tanks

4. Comparison of combustion models

There are many combustion models available in ANSYS Fluent. These combustion models are grouped into Species Transport and Finite-Rate Chemistry, Non-Premixed Combustion, Premixed Combustion, and Partially Premixed Combustion. The purpose of this chapter is to compare a couple suitable models and to determine which one to use throughout the rest of the project. The main focus is put on the models available under the group Non-Premixed Combustion, since this is the type of combustion that a pool fire is. The benefit of non-premixed combustion models is that the variable mixture fraction is used. Through the mixture fraction variable, the thermochemistry is greatly reduced down to one variable. The EDC Model, which lies under the Species Transport and Finite-Rate Chemistry group, is also tested in this chapter. Instead of using the mixture fraction approach, the conservation equation for every chemical species involved in the combustion process is solved in the EDC model. Solving the stiff chemistry in the EDC model is computationally intensive and time-consuming. However, it does provide more control over the chemical mechanisms when desired [8].

4.1 Simulation setup

The results generated with different combustion models are compared to empirical data for validation when possible. The detailed experimental setup could be found in reference [14]. The simulation setup is shown in Figure 8 below

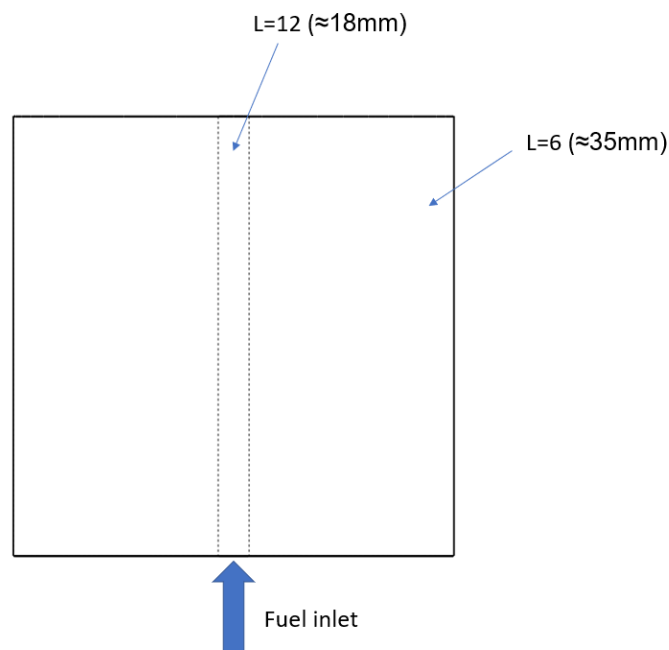


Figure 8: Domain setup for combustion models comparison

The diameter of the pool is 0.3m. The width and height of the domain are 10 times the diameter of the pool, hence 3m for both parameters. The cylindrical volume in the middle of the domain is the volume directly above the fuel inlet. A finer mesh resolution is used in this region since the flame will result in sharp gradients of temperature, density, velocity...etc. Outside of this region a coarser mesh is used. This is mainly for the purpose of reducing the cell count, hence reducing the calculation time. The non-dimensional value L is calculated according to Eq. 4. Both L values fall in the range recommended by NIST. In order to accommodate the really large gradients close to the combustion surface, the mesh is further refined. This is shown in Figure 9.

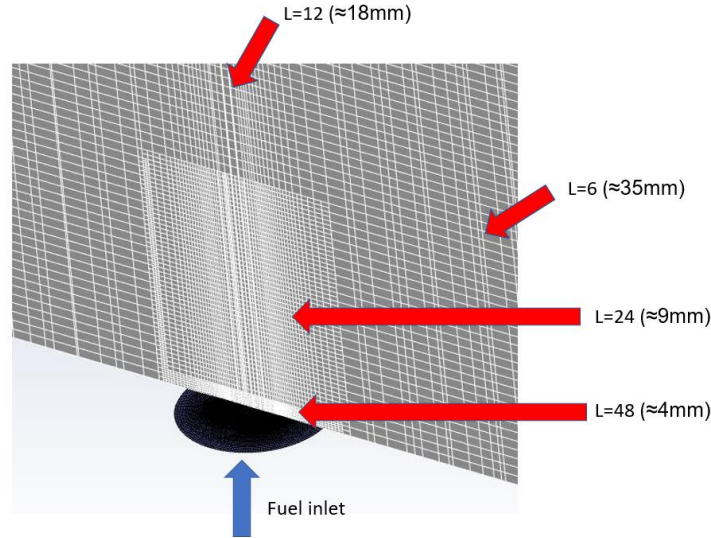


Figure 9: Grid used for the combustion models comparison

The mesh is further refined from $L=12$ to $L=24$ where the flame is burning. The height of this zone is determined by the theoretical flame height, calculated with Eq. 1. The mesh is further refined to $L=48$ just above the combustion surface to ensure that the drastic change in gradients does not result in any calculation errors. This decision is made based on experiences for it is already known that the region with the most intense reaction requires the finest mesh.

For most of the simulations conducted in this chapter, methanol is burned as the fuel, following the experiment. The only exception is the unsteady diffusion flamelet model presented in chapter 4.2, which burns kerosene. This is because the biggest advantage of the unsteady diffusion flamelet model is its capability of predicting the formation of soot. If methanol were burned in this test, it could be difficult to see the model's capability since methanol does not form much soot.

A list of simulations conducted in this chapter is provided below for clarity.

Table 1: List of simulations conducted in chapter 4

Number	Model	Fuel	Pool diameter [m]	Fuel mass inflow [kg/s]
1	UDF	Kerosene	0.3	0.002757
2	EDC			0.001202
3	CE			
4	SDF			
5	CE+user defined function	Methanol		

Note that the UDF and EDC models were not actually compared to the experimental data in the end. This is because neither simulations could be conducted in LES simulation, hence it was deemed unnecessary for the comparison. The process and results from these simulations are included in the report nonetheless for the purpose of recording the difficulties encountered. A discussion of the possible causes and possible solutions to these difficulties is given after the results are presented.

4.2 Unsteady Diffusion Flamelet model (UDF)

The UDF model is not compatible with a non-steady flow field, hence the investigation was carried out in RANS simulation. The figures below show the temperature contour of a fire stopped at

different number of iterations. It can be seen that when the simulation is stopped at different iterations the fire looks very differently. This shows that pool fires do not reach a steady-state result, hence the UDF model cannot be applied. The fuel burnt in this simulation is kerosene instead of methanol as done in the experiment. This however does not affect the fact that pool fires are highly unstable by nature.

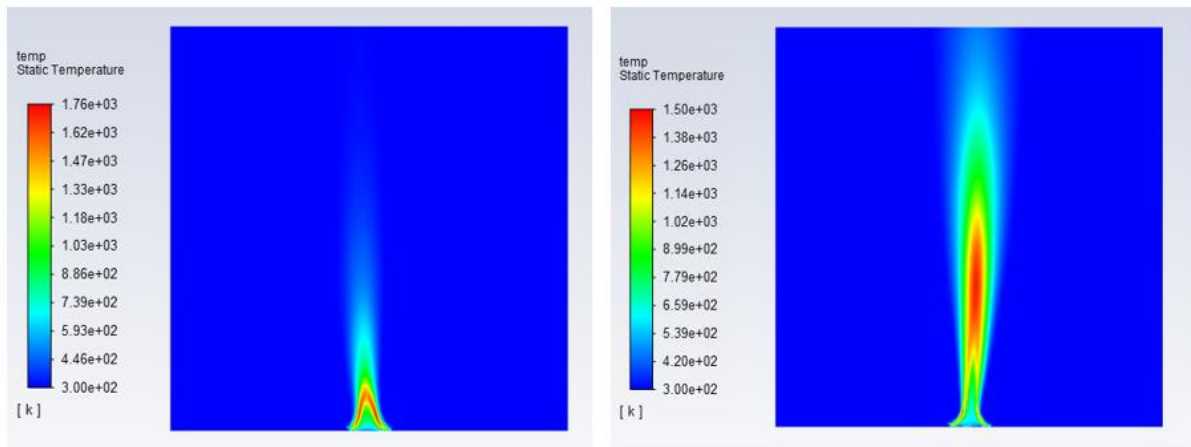
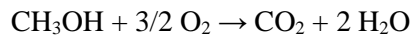


Figure 10: Simulation stopped at different number of iterations in RANS

4.3 Eddy Dissipation Concept model (EDC)

Numerous difficulties were encountered while attempting to ignite a pool fire with the EDC model. The investigation started with LES simulation. After much endeavors without any success, it was attempted to start a fire in RANS simulation first, then, if successful, the simulation will be switched to a LES simulation. Only one governing reaction was used in this attempt, namely,



This is in order to keep the chemistry simple at this stage so that the effort could be focused on starting a fire. In reality, the combustion of methanol is an extremely complicated process which involves 50+ species and 300+ elementary reactions [15].

A fire was started in RANS simulation and the temperature contour is shown in Figure 11.

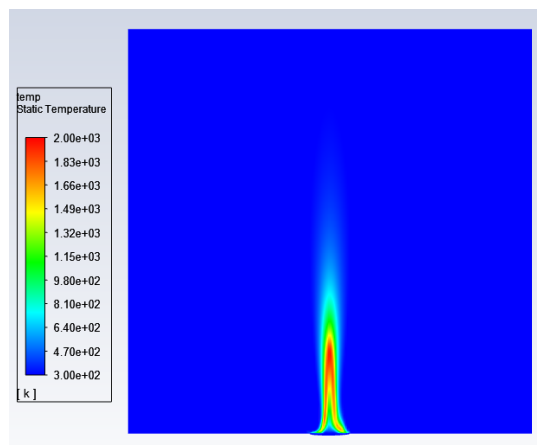


Figure 11: Temperature contour produced by the EDC model, in RANS

Unfortunately, the fire extinguished when the model was switched to LES simulation. Due to time constraint, no further investigation was conducted. However, two possible causes were drawn from the available results. These hypothesis could be investigated further if enough computing power is available.

1. Very fine mesh is needed because mixing occurs at the scale of small eddies

The EDC model assumes that all reactions occur within the fine scales. A more detailed explanation can be found in Appendix A.6. It is hypothesized that the modelled fine scales must be on the same scale as the length scale where the reactions occur in reality, otherwise the reactions won't occur. This involves two challenges. First, how small is the fine-scale where reactions occur in reality is unknown. Second, after knowing the physical size of these scales, modelling them could be very challenging in terms of computational power. For example, assuming these reactions occur on the scale of 0.1 [mm], this could be considered extremely small in a domain of a couple meters. Modelling these small structures will result in a very high number of cell counts, which is a very limiting factor for further research.

2. Very small time step is needed because some reactions occur very fast

Combustion involves many reactions, where the reaction time could vary from the scale of 10^0 [s] to 10^{-8} [s]. It is hypothesized that, in order to capture the fast reactions, a small enough time step size must be used in the model. This again could be very challenging in terms of computational power. For example, assuming a time step size of 10 nanoseconds is used and 5 seconds of data must be collected, this implies that half a billion time steps will be required. Assuming each time step takes two minutes of calculation time, it will take roughly 1900 years to collect 5 seconds of data.

4.4 Chemical Equilibrium model (CE) vs. Steady Diffusion Flamelet model (SDF)

Figure 12 shows the locations where data are sampled in the flame. The vertical line is at the center at the flame. The other three horizontal lines are at $z=0.033$ [m], 0.303 [m], and 0.603 [m].

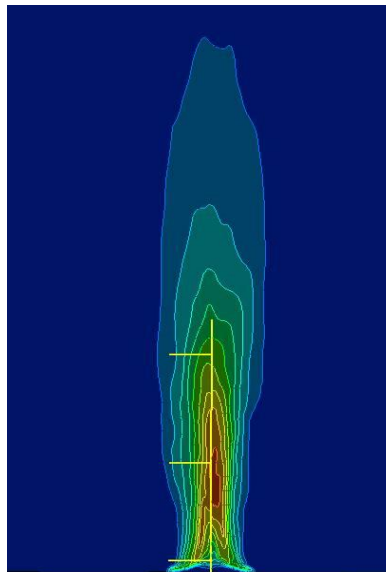


Figure 12: Location of sampling in the CE vs. SDF comparison

The scalar dissipation rate is examined since the biggest difference between the CE and SDF model is that the SDF model takes the scalar dissipation rate into account. The contour of the scalar dissipation rate of the SDF model is shown in Figure 13 below.

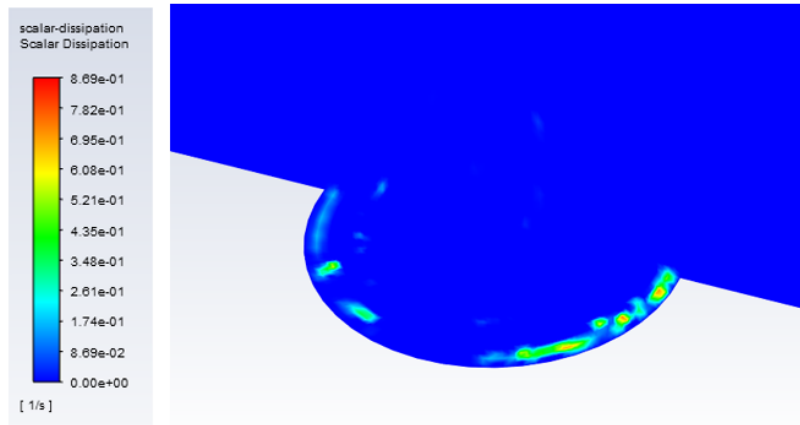


Figure 13: Contour of scalar dissipation rate, SDF model

Shown in the figure is the fuel inlet because this is the only area in the domain exhibiting scalar dissipation. The maximum value of scalar dissipation rate shown in the contour is about 0.87 [1/s]. This is quite a small rate. To put matters into perspective, a Sandia D flame with a jet velocity of 49.6 [m/s] would produce scalar dissipation rate as high as 100 [1/s] [16] [17].

4.5 Results comparison among experiment, CE, and SDF

The heat of reaction and temperature profile sampled at different locations in the flame are reported in Figure 14 through Figure 19 below.

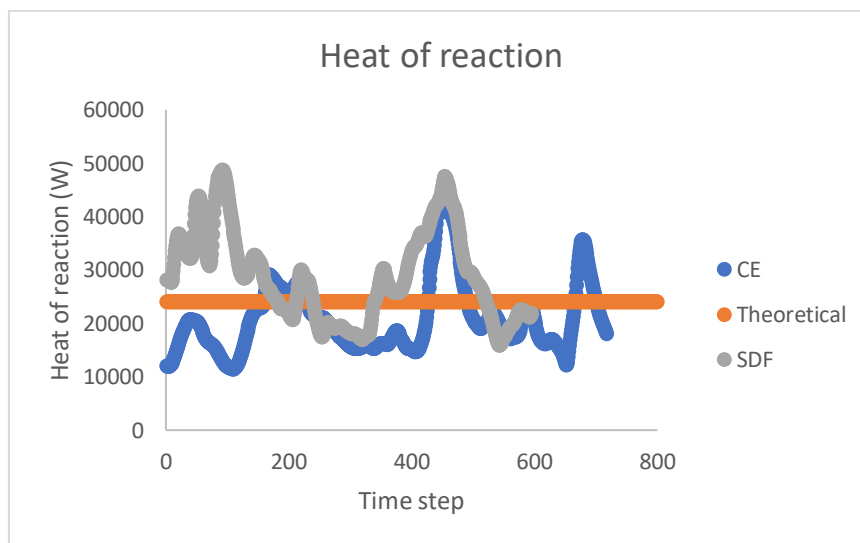


Figure 14: Heat of reaction, CE vs. SDF

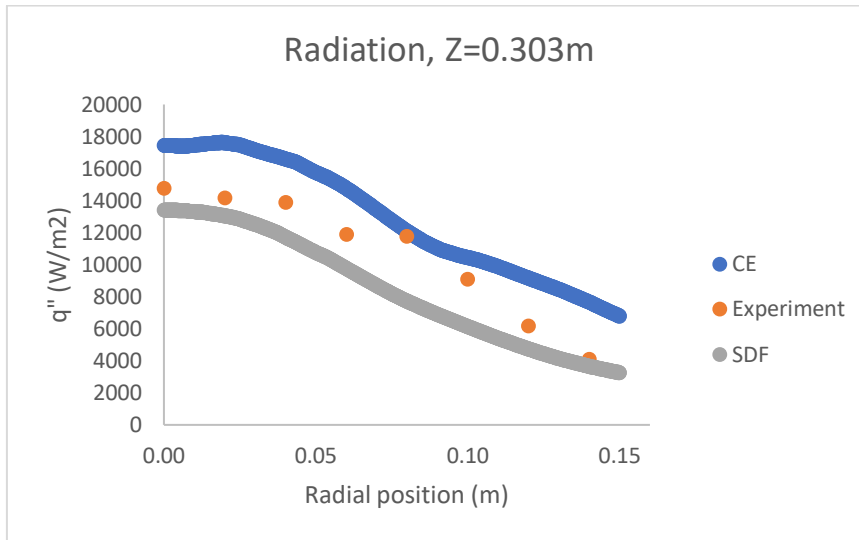


Figure 15: Plot of mean radiation sampled at $z=0.303$ m, CE vs. SDF

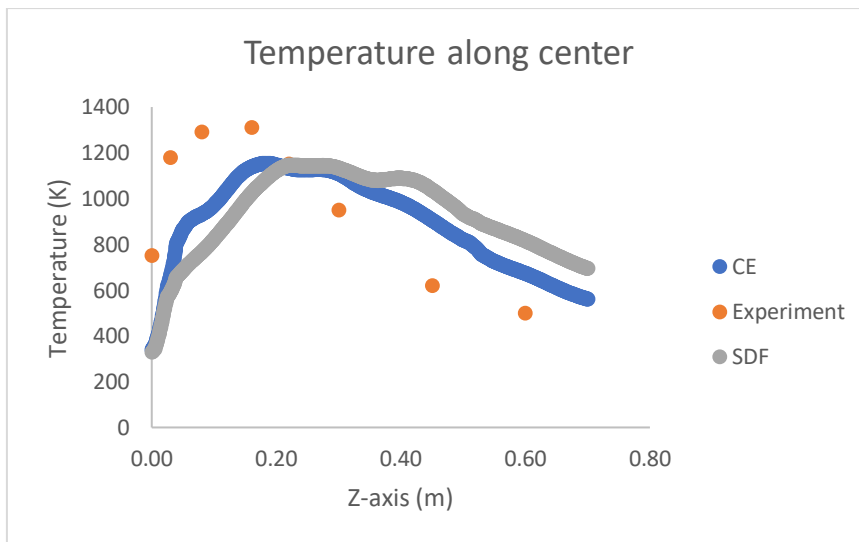


Figure 16: Plot of mean temperature sampled along the centerline, CE vs. SDF

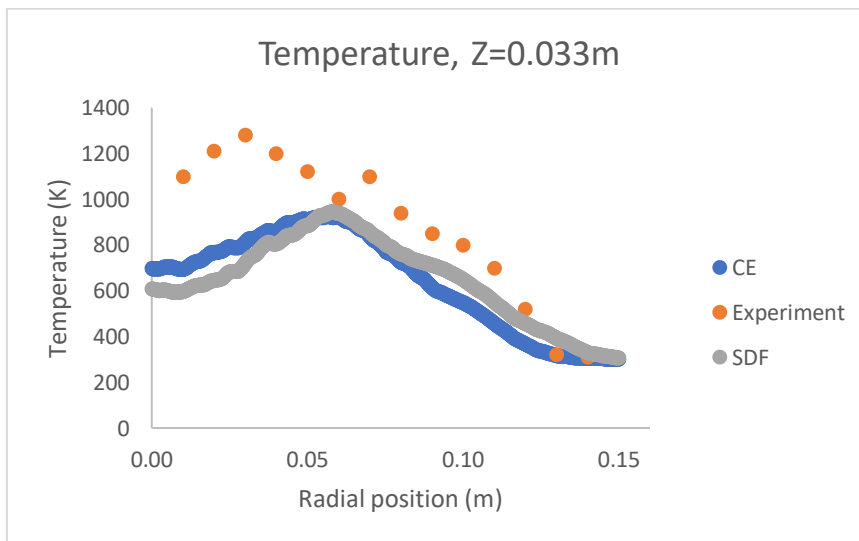


Figure 17: Plot of mean temperature sampled at $z=0.033$ m, CE vs. SDF

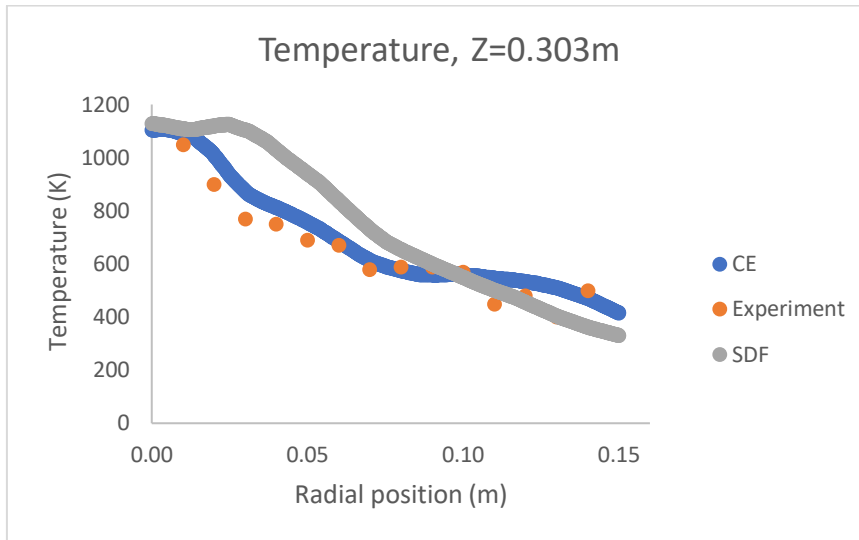


Figure 18: Plot of mean temperature sampled at $z=0.303$ m, CE vs. SDF

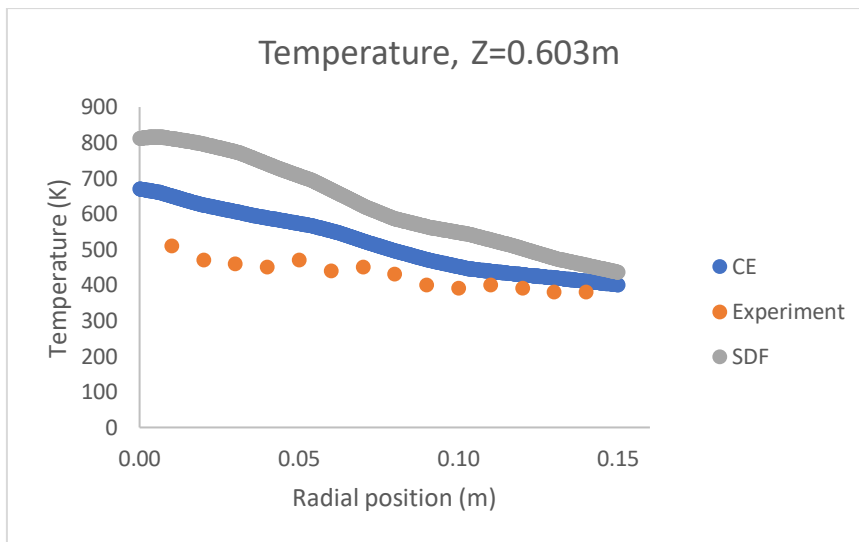


Figure 19: Plot of mean temperature sampled at $z=0.603$ m, CE vs. SDF

The theoretical value for the heat of reaction is 24.000 [W]. The averaged value produced by the CE model is 20.887 [W], and the SDF 28.745 [W], which translates to 13% and 20% percent error, respectively. It can be seen that the CE model underpredicts, and the SDF model overpredicts. Judging from the percent error, the CE model performed better.

Looking at the temperature contours, it appears that the models perform better some distance away from the combustion surface. A possible explanation to this phenomena is that the large gradients close to the combustion surface are more difficult to predict. Further away, at $z=0.603$ [m], both models start to overpredict the temperature. The most deviations are shown close to the combustion surface. This could be seen from Figure 16 and 17. From these two figures it can be seen that, the profiles have a similar trend compared to the empirical data. However, close to the combustion surface, especially close to the center of the combustion surface, both models underpredict the temperature significantly. It is hypothesized that this could be the result of Fluent only taking the absorption coefficient of water and carbon dioxide into account regarding radiation calculation. It was attempted to add the absorption coefficient of methanol to the calculation so that the core of the flame would absorb more radiation

emitted by the flame, hence increasing the temperature, which would make this a more accurate model. Details of this attempt is reported in the next section.

4.6 Planck Mean Absorption Coefficient (PMAC)

The absorption coefficient is a parameter that varies significantly with the spectrum. This means that, if it is desired to include an accurate absorption coefficient of a certain substance in the calculation, the absorption coefficient throughout the entire spectrum needs to be included. However, doing this requires much knowledge in this particular field and is beyond the scope of this project. This project approaches the issue by using a mean absorption coefficient. Namely, the Planck Mean Absorption Coefficient (PMAC). The PMAC expresses the absorption coefficient of a medium as a mean value and expresses it as a function only of temperature, which significantly simplifies the problem [18].

Before proceeding to include the PMAC of methanol in the simulation, the PMAC of methanol is found in literature and compared to the PMAC of water vapor and CO₂. This is to make sure that the PMAC of methanol indeed plays a major role in the calculation of radiation absorption. The PMAC of CO₂ and water vapor are also found in literature and reported below [19] [20].

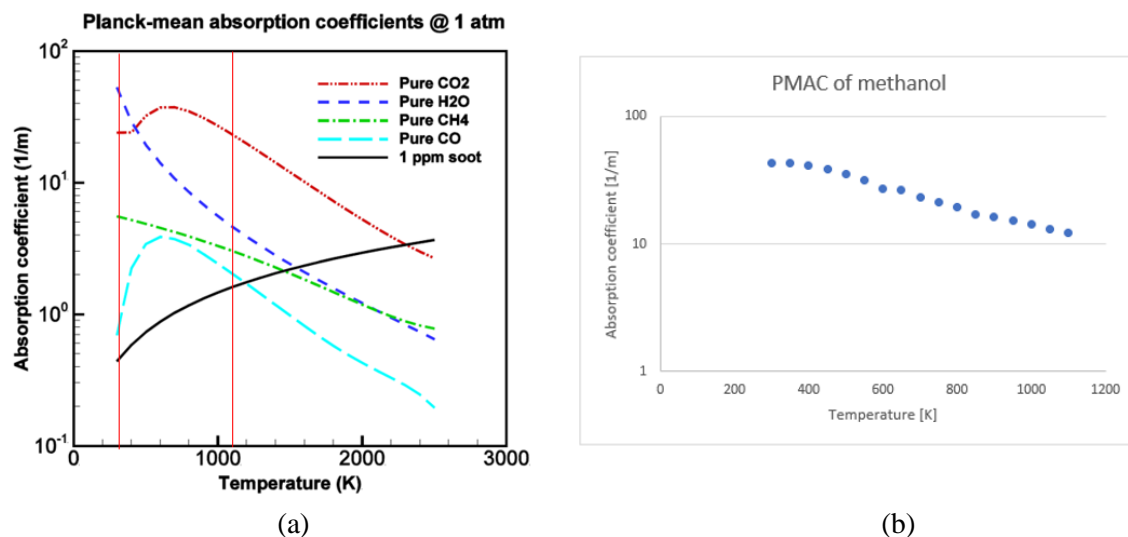


Figure 20: PMAC of (a) CO₂ and H₂O (b) methanol

The original data for the PMAC of methanol was found in reference [20]. The data shown here has been adjusted to have the same unit as the data shown in Figure 20(a) for comparison. The two red vertical lines in Figure 20(a) show the range of data available for methanol, since the data is only available up to 1200 [K] for methanol. It can be seen that the PMAC of methanol is in the same order of magnitude with CO₂, both falling roughly between the range of 20 to 60 [1/m]. The PMAC of methanol and H₂O fall within the same order of magnitude at lower temperature, roughly between 300-500 [K]. This comparison shows that methanol is a major source of radiation absorption and adding it to the radiation calculation could be one way of improving the flame burning too cold at the center as predicted by the CE and SDF model.

4.7 CE model with the user defined function

In order to include the PMAC of methanol in the calculation, a user defined function must be written and be hooked to the model in Fluent. The user defined function is shown in Appendix B.1. The user defined function is tested with the chemical equilibrium model. The results are shown in Figure 21 through Figure 26 below. The results of the user defined function are shown as the yellow lines in the

figures, and is called CE-UDF in the legend. This is not to be confused with the unsteady diffusion flamelet model.

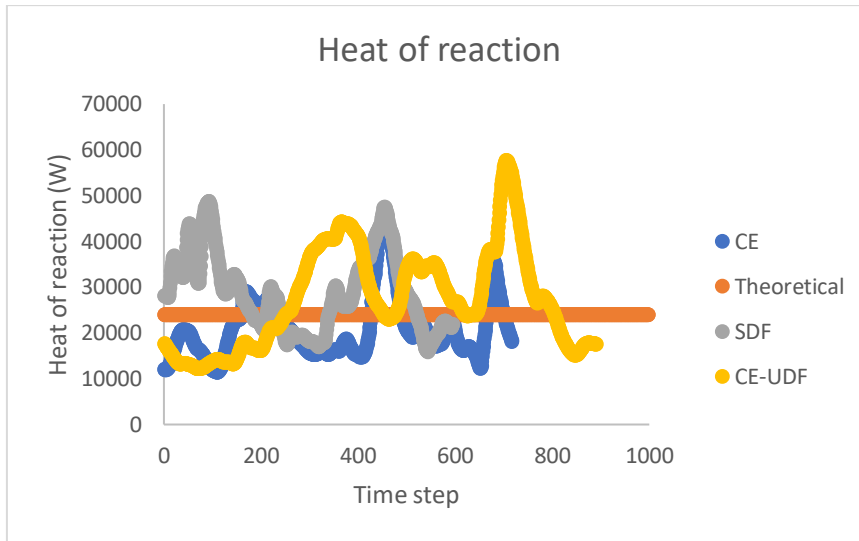


Figure 21: Heat of reaction, CE, SDF, and CE with user defined function

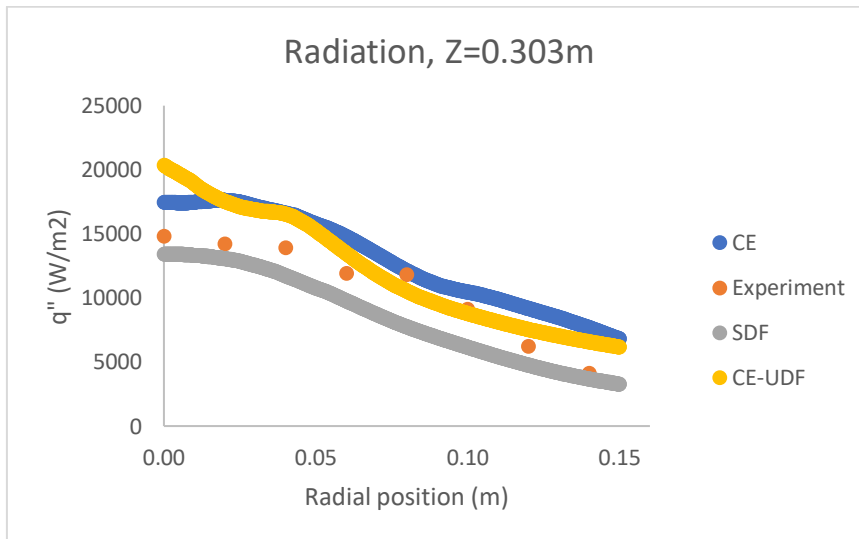


Figure 22: Plot of mean radiation sampled at $z=0.303$ m, CE, SDF, and CE with user defined function

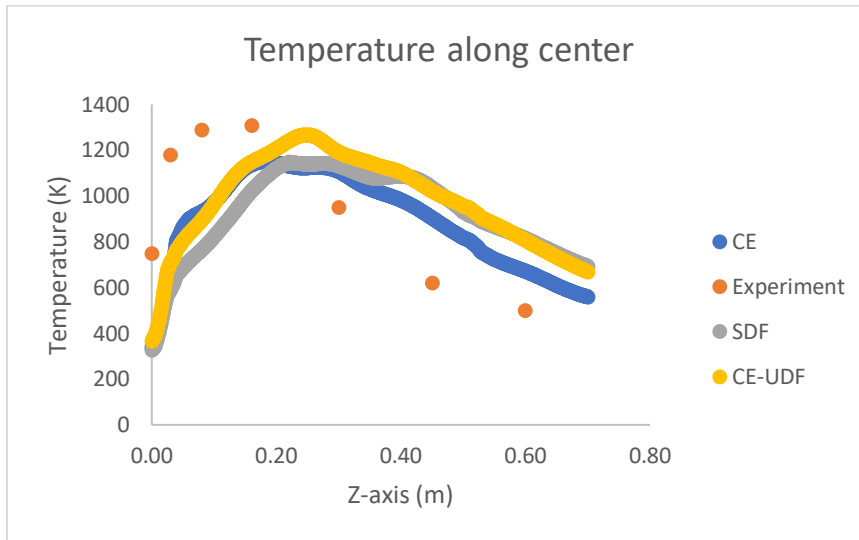


Figure 23: Plot of mean temperature sampled along centerline, CE, SDF, and CE with user defined function

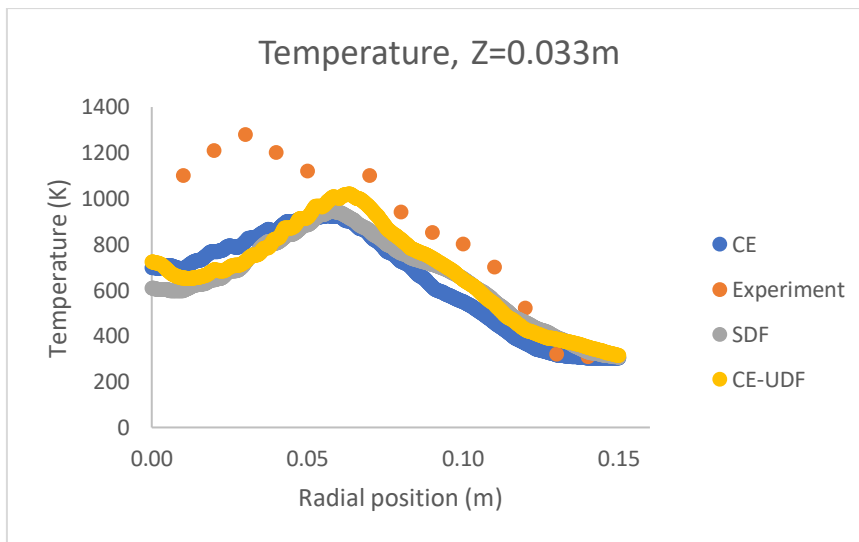


Figure 24: Plot of mean temperature sampled at $z=0.033$ m, CE, SDF, and CE with user defined function

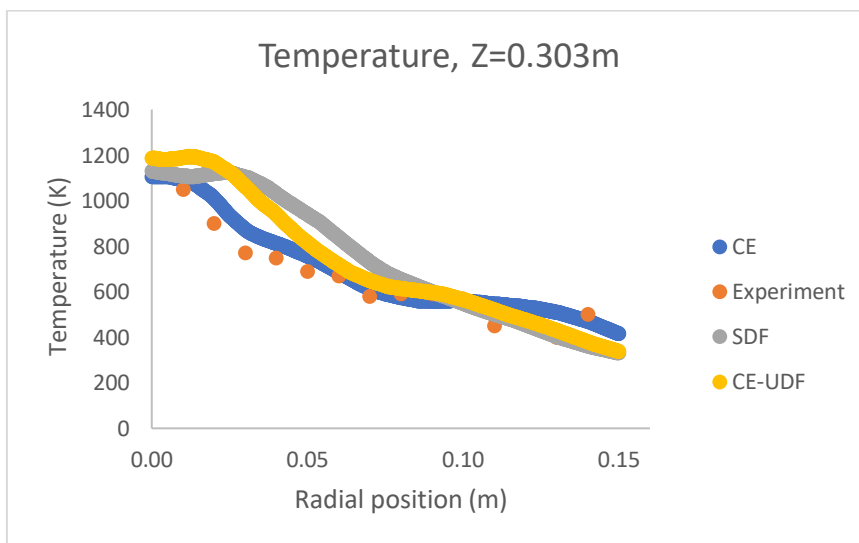


Figure 25: Plot of mean temperature sampled at $z=0.303$ m, CE, SDF, and CE with user defined function

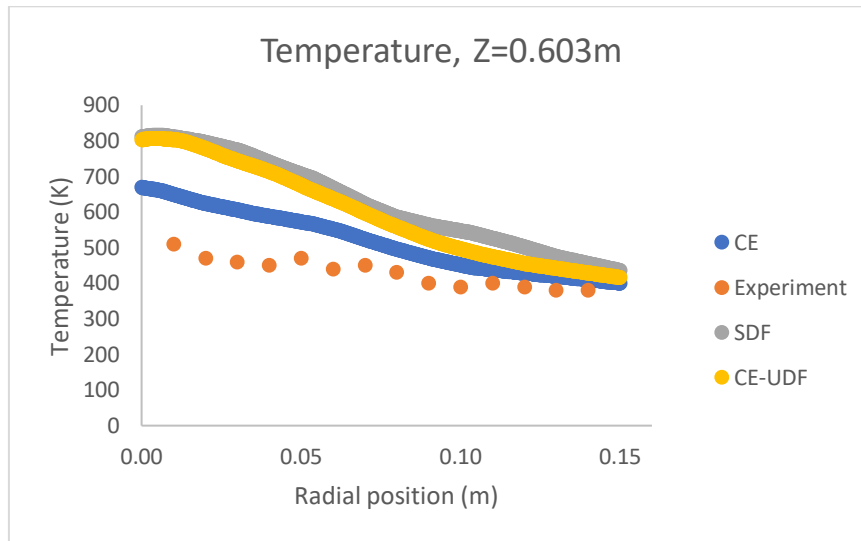


Figure 26: Plot of mean temperature sampled at $z=0.603$ m, CE, SDF, and CE with user defined function

Judging from the temperature contours, the user defined function did not solve the issue of the flame burning too cold close to the combustion surface. It can be seen that the UDF function has slightly raised the flame temperature close to the center in Figure 24. However, looking at Figure 23, it does not appear that the UDF code has improved the accuracy of the model significantly. The effect of adding the PMAC of methanol is also reflected in Figure 22, where the flame appears to be emitting more radiation from $z=0$ [m] to $z=0.02$ [m]. Nevertheless, this effect fades away as the sampling moves away from the combustion surface in the radial direction.

There are a couple possible reasons why the flame still burns too cold at the center close to the combustion surface. One possible reason is that oxygen is not being mixed enough with the fuel inside the flame. This could be seen in Figure 27 below.

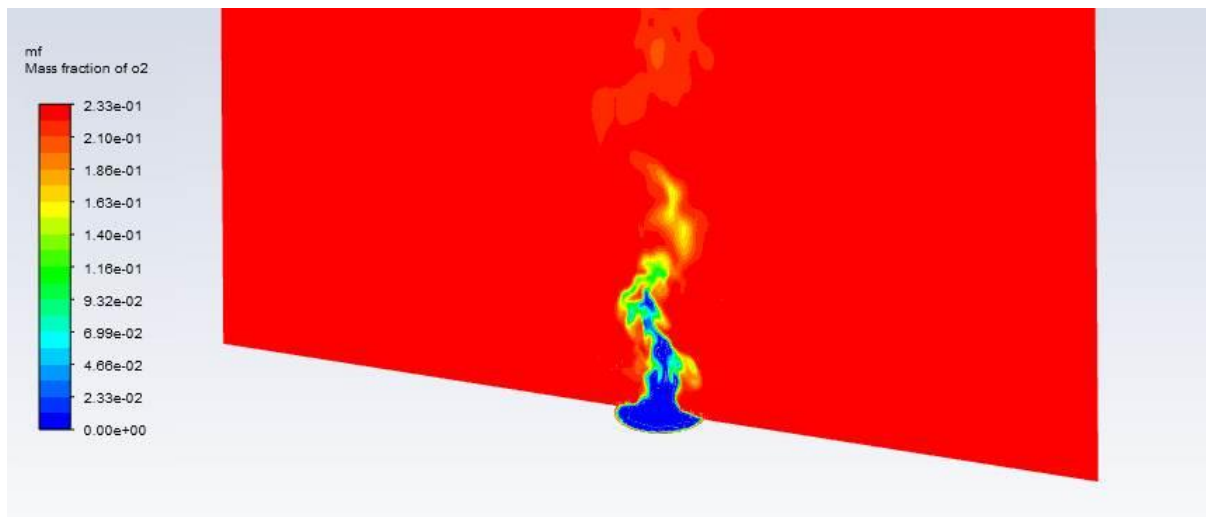


Figure 27: Mass fraction of O₂

Another reason is that there are in fact some discrepancies between the computer model and the actual experimental setup. Firstly, in the experiment, there is an actual pool of fuel, which is not present in the computer model. In the simulation, the fuel present is simply a mass inflow of methanol vapor. This is because, as the fuel burns, the fuel level would decrease. This phenomenon is in fact very

difficult to model. Another discrepancy is that the rim of the pool is omitted in the computer model. This was a measure taken to simplify the model, since the heat transfer in the rim was not of any interest. However, literature research has shown that the rim could in fact have a big impact on the flame, as the rim would feed thermal radiation back to the fuel [21].

4.8 Conclusion from the combustion models

The study concentrated mostly on the nonpremixed combustion models: unsteady diffusion flamelet (UDF), chemical equilibrium (CE) model, and the steady diffusion flamelet (SDF) model. The eddy-dissipation concept model (EDC) is not in the nonpremixed combustion group, but in the species transport group. The results were presented in the order of UDF, EDC, CE, and SDF in order to reflect the increasing order of importance for the study.

Results from the UDF model, which had to be run in RANS, was disappointing, as was more or less expected due to the heavily unsteady nature of pool fires; no stable solution emerged. No satisfactory results were produced from the EDC model within the time allowed, but the EDC model has attractive features, and appears to be worth more investigation. The potential advantage of EDC is that it includes detailed time-dependent chemistry, and it therefore allows modelling of soot based on soot-precursors, with soot having huge effect on radiation contours. The draw-back of EDC is that the computational intensity is orders of magnitude higher than models based on fast chemistry, and that detailed chemical data of the reactions involved is necessary. Furthermore, since the UDF model is not compatible with LES simulation, it is the only model that's capable of predicting the slow chemistry in a combustion process among all the models tested in this report. This could be very useful if details about the formation of soot were to be investigated.

The results from the CE vs. SDF comparison did not make a clear indication which model is superior. Although temperature patterns correspond to experiment, and although temperatures some distance away from the center correspond reasonably with experiment, temperatures around the center and close to the inlet deviate substantially. The attempt of adding the PMAC of methanol to the simulation to better simulate radiation absorption close to the inlet and thereby get a better prediction of temperature close to the pool did not yield significant improvement either. In order to improve the accuracy of simulations, a couple directions could be assessed. The physical reality simulated in the computer should better reflect the actual experiment, meaning that the rim should be added in the computer model, and the fuel pool should be included, if possible. When these two objects are included, the absorption and emission coefficients of these two objects should also be included in order to account for the heat transfer between them and the flame.

Disappointingly, only minor changes are reflected in the results when the user defined function is hooked to the simulation, and temperature in the fire-center remains too low. Two approaches could be taken to potentially solve this issue. First, instead of using the PMAC, the effect of using a more accurate method could be investigated. This is to say that the spectral information of each species can be included in the calculation. Second, instead of only including the absorption coefficient of CO_2 , H_2O , and methanol, the absorption coefficient of more species could be included, or at least the most dominant species could be included. Hypothesis development as to the reason for low temperature in the center area in the simulation merits to be elaborated further.

For the remainder of this report, the SDF model will be used throughout. This is a practical choice: the SDF model grants more access to the different soot models. For example, in Fluent, the Moss-Brookes-Hall (MBH) model is only available when the species C_2H_2 , C_6H_6 , C_6H_5 , and H_2 are present in the system. The user has less control in the CE model and these species are often not present

in the species list when CE is utilized. Hence, in order to include soot modelling possibilities, the SDF model must be used.

5. Comparison of soot models

A total of two simulations are conducted in this section of the report. The main focus of this chapter of the report is to run two simulations with two different soot models, and to compare the results to published data. The main goal here is not to produce accurate data, but rather, to learn about the capabilities of the available soot models. The data generated here should serve as a place to start future projects instead of being treated as conclusive results.

5.1 Simulation setup

After testing a smaller pool fire with a 0.3 [m] diameter as seen in the previous chapter, it was determined that testing a larger pool would produce more practical results since pool fires are rarely as small as 0.3 [m] in the industry. The pool simulated for the remainder of the report is a circular pool with a diameter of 2 [m] and the fuel being burned is JP8. The mass loss rate of JP8 is unavailable. Hence, the mass loss rate of JP5 is used, which is $0.054 \text{ [kg/m}^2\text{-s]}$ [13]. This value multiplied by the area of the pool gives the mass inflow of 0.1696 [kg/s] .

A 2 meter pool is in fact still not considered large in a practical sense. However, experiments are rarely conducted with a pool of 2 [m] or above hence the available data is quite scarce. For this reason, a 2 [m] pool will be burned. The experimental setup can be found in reference [22].

The domain size used here is 10 times the height and 15 times the width of the pool. This is larger than the ratio used previously in the methanol pool fire, which is 10 times the height and 10 times the width. This is because JP8 has a much higher heat release rate and the size of the flame is much larger than a methanol flame. In order to make sure that the safety distance regarding the thermal radiation is taken into account, the width of domain is enlarged to 15 times the width of the pool. The domain and mesh used are shown below.

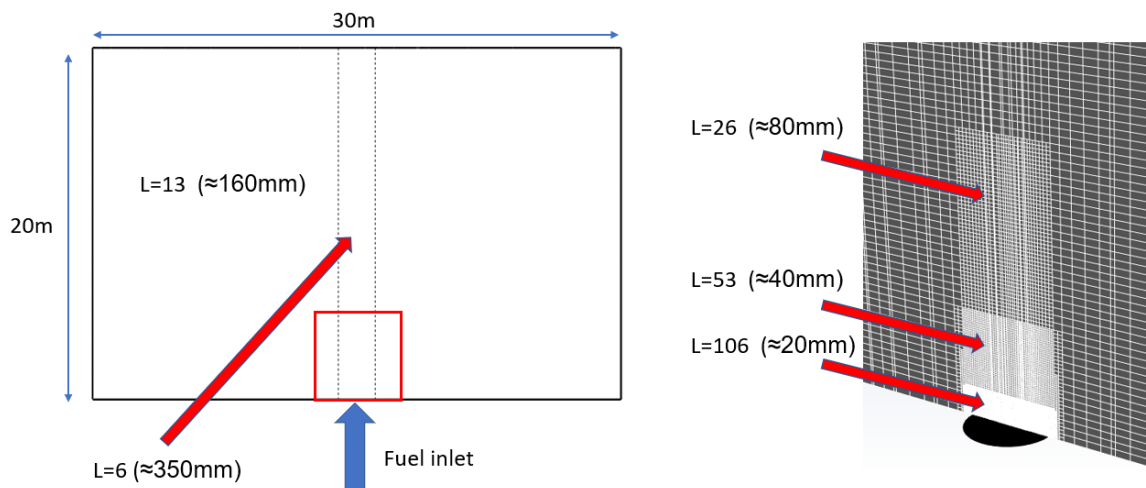


Figure 28: Domain setup for soot models comparison

The mesh used for the domain is similar to the one used in chapter 4, where one size is used for most of the domain, and mesh is refined in the cylindrical volume in the center. The area indicated by the red box on the left is enlarged and shown on the right, where the mesh is refined further in order to accommodate the flame. When compared to Figure 9, it can be seen that one extra refined layer is added, and that the height of the finest layer is increased. This is an attempt made to fix the issue of the flame burning too cold at the center, and to make sure that there is no jump too large in the cell size which may lead to instabilities in the model.

5.2 Theory of the soot model developed by Huygens Engineers (HE)

Various soot models are available in Fluent. However, these models are all developed differently and may not always be applicable to all situations. Or, it could be possible that one model provides superior accuracy, but a certain parameter is unknown to the user and cannot be inserted to the model. For these reasons, Huygens Engineers derived a simple soot model, which will be called the HE model in this report. This model takes an empirical approach to the soot formation problem. The aim of this model is not to predict soot formation accurately, and the purpose of testing it here is not to improve it further. Rather, having moderate accuracy would be considered satisfactory for this model, and the purpose of testing it here is to see how it performs relatively compared to other existing models.

The goal of the HE model is to calculate the absorption coefficient of soot. The expression used to calculate the soot absorption coefficient is taken directly from the ANSYS Fluent theory guide and is repeated here [8]

$$\alpha_{g+s} = \alpha_g + \alpha_s \quad (7)$$

$$\alpha_s = b_1 \rho_g Y_{soot} [1 + b_T (T - 2000)] \quad (8)$$

α_g = absorption coefficient for gas mixture

α_s = absorption coefficient for soot

ρ_g = gas mixture density [kg/m³]

Y_{soot} = soot mass fraction

$b_1 = 1232,4 \text{ m}^2/\text{kg}$

$b_T = 4,8 \times 10^{-4} \text{ K}^{-1}$

where b_1 and b_T are empirical values found in experiments. The only unknown parameter left is the soot mass fraction. The calculation of soot mass fraction is the part developed by HE, and is shown below,

$$Y_{soot} = \frac{0,042}{2,83} * Y_{CO_2} + \frac{0,042}{2,83} * \frac{44}{28} * Y_{CO} \quad (9)$$

the value 0.042 and 2.83 used are retrieved from the SFPE Handbook of Fire Protection Engineering [6]. Part of the table is shown in Table 2 below

Table 2: Yield of fire production and chemical, convective, and radiative heats of combustion for well-ventilated fires

Material	ΔH_T (kJ/g)	Y_{CO_2}	Y_{CO}	Y_{ch}	Y_s	ΔH_{ch}	ΔH_{con}	ΔH_{rad}
		(g/g)				(kJ/g)		
<i>Common gases</i>								
Methane	50.1	2.72	—	—	—	49.6	42.6	7.0
Ethane	47.1	2.85	0.001	0.001	0.013	45.7	34.1	11.6
Propane	46.0	2.85	0.005	0.001	0.024	43.7	31.2	12.5
Butane	45.4	2.85	0.007	0.003	0.029	42.6	29.6	13.0
Ethylene	48.0	2.72	0.013	0.005	0.043	41.5	27.3	14.2
Propylene	46.4	2.74	0.017	0.006	0.095	40.5	25.6	14.9
1,3-Butadiene	44.6	2.46	0.048	0.014	0.125	33.6	15.4	18.2
Acetylene	47.8	2.60	0.042	0.013	0.096	36.7	18.7	18.0
<i>Common liquids</i>								
Methyl alcohol	20.0	1.31	0.001	—	—	19.1	16.1	3.0
Ethyl alcohol	27.7	1.77	0.001	0.001	0.008	25.6	19.0	6.5
Isopropyl alcohol	31.8	2.01	0.003	0.001	0.015	29.0	20.6	8.5
Acetone	29.7	2.14	0.003	0.001	0.014	27.9	20.3	7.6
Methylethyl ketone	32.7	2.29	0.004	0.001	0.018	30.6	22.1	8.6
Heptane	44.6	2.85	0.010	0.004	0.037	41.2	27.6	13.6
Octane	44.5	2.84	0.011	0.004	0.038	41.0	27.3	13.7
Kerosene	44.1	2.83	0.012	0.004	0.042	40.3	26.2	14.1
Benzene	40.1	2.33	0.067	0.018	0.181	27.6	11.0	16.5

The data for JP8 is not available. However, since JP8 is kerosene based, the data for kerosene is used instead. The data used indicates how many grams of a certain substance is produced per grams of fuel burned. For example, every gram of kerosene that is burned, 2.83 [g] of CO₂ will be produced. The ratio 0.042/2.83 [g/g] indicates how many grams of soot will be produced per grams of kerosene burned. The 44/28 ratio is an assumption that all the CO will eventually turn into CO₂, hence the ratio of 0.042/2.83 in front of the term stays the same. This formulation assumes that all soot particles come from the presence of CO and CO₂. The mass fraction of CO and CO₂ are standard outputs of Fluent. The user defined function is presented in Appendix B.2.

5.3 Results of Moss-Brookes-Hall (MBH) model vs. HE model

The results generated by the HE model are compared to results generated by the MBH model. The MBH model was chosen because it has a less empirical background compared to the other models available in Fluent, namely the one-step or the two-step models [8]. Since the HE model is an empirical model, it was deemed beneficial if it was compared to a less empirical model. One big advantage of the MBH model is that it was developed for higher hydrocarbon fuels, which is the fuel burned in these tests. The model that it was based on, the Moss-Brookes model, can only be applied to methane-air combustion. More details about the MBH model can be found in Appendix A.9.

The temperature contours from both simulations are presented below. These pictures are snapped at the moment the simulations were stopped.

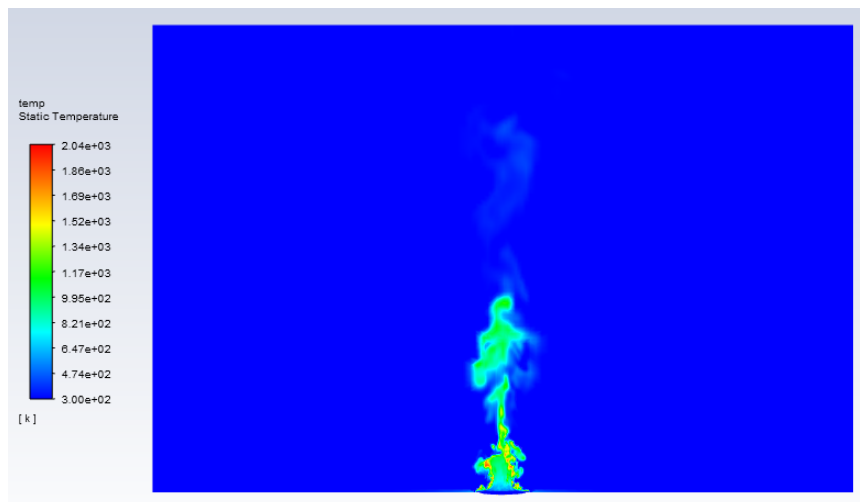


Figure 29: Temperature contour from the MBH model

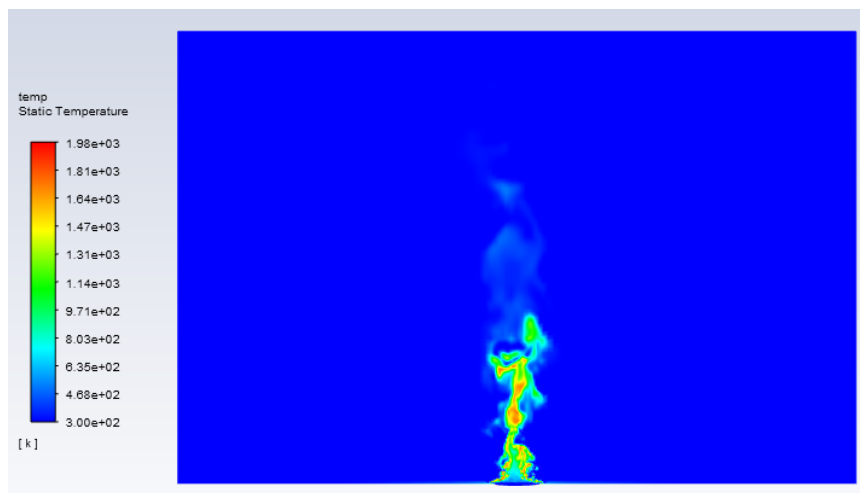


Figure 30: Temperature contour from the HE model

The unsteady nature of pool fires can be clearly seen in these two figures. When compared to the contours that are generated in RANS simulation, these two contours are exhibiting a lot more detailed structures of the flame, rather than the blurred out structure generated through an averaging method. In Figure 29, the pulsating effect of pool fire can be seen, where a plume of hot gases is just about to be detached, or has just detached, from the main body of the flame.

Soot volume fraction predicted by both models are compared to published data found in [22]. Five cycles of data were collected, which equals to roughly 4,7 seconds of data. The data was sampled at coordinate (0,1-0-1,27), same as the experiment.

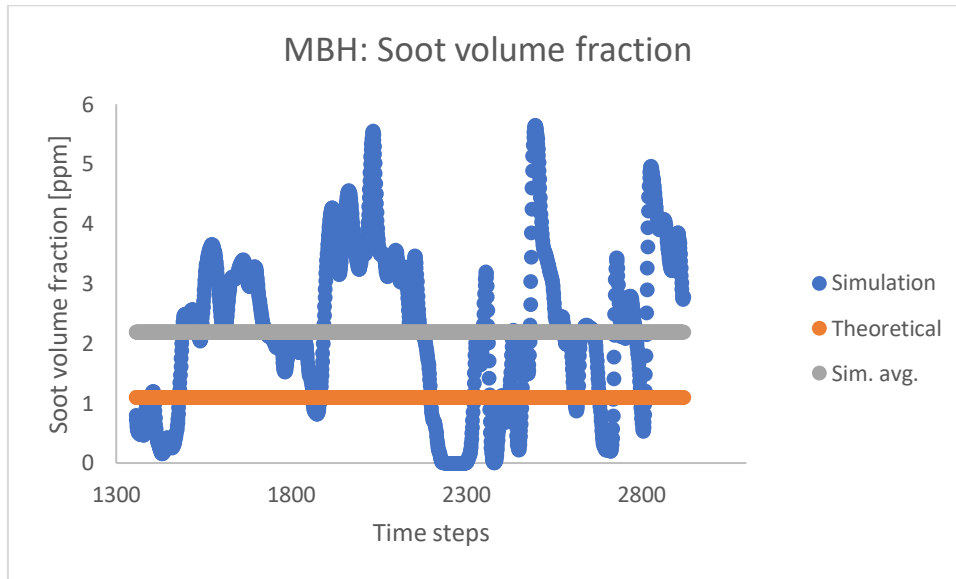


Figure 31: Soot volume fraction generated by the MBH model

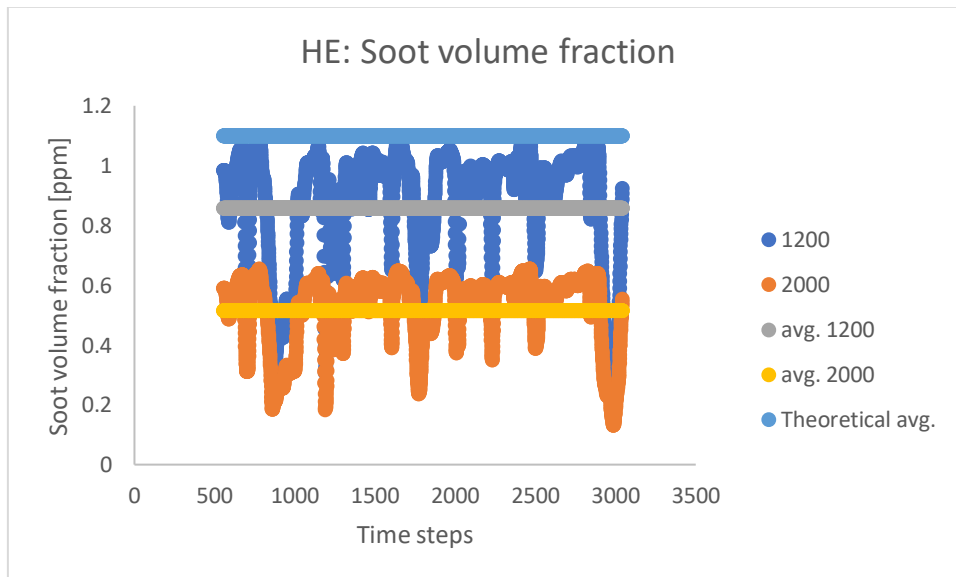


Figure 32: Soot volume fraction generated by the HE model, with different soot particle density

In Figure 31, the blue line is the collected data. The orange line is the average value for experimental data, which is 1,1 [ppm], and the gray line is the average value for the collected data, which is 2,2 [ppm].

Since the HE model only calculates the soot mass fraction, the value needs to be post-processed and translated to soot volume fraction. This is done through the following expression

$$v = Y * \frac{\rho_{tot}}{\rho_1} \quad (10)$$

v = volume fraction

Y = mass fraction

ρ = density

ρ_{tot} is the density of the gas mixture, ρ_1 is the density of species 1, which is soot in this case [23].

The soot volume fraction predicted by the HE model is shown in Figure 32. Here two sets of sampled data are shown, with the name 1200 and 2000. These represent the different volume fraction obtained when different values for the soot particle density is used. The value 1200 [kg/m³] comes from reference [24]. The source states that soot particle density ranges from 300-1200 [kg/m³]. The 2000 [kg/m³] is the value assumed by the MBH model, which is the number originally assumed by the developers of the model. The gray and yellow lines represent the averaged value of the data set 1200 and 2000, which are 0,86 [ppm] and 0,51 [ppm]. The light blue line represents the average value from the experimental data, which is 1,1 [ppm].

The reference experiment did not report the temperature nor radiation data. However, the temperature and radiation contours are compared between the two models to see if one model behaves differently from the other. These results are shown below.

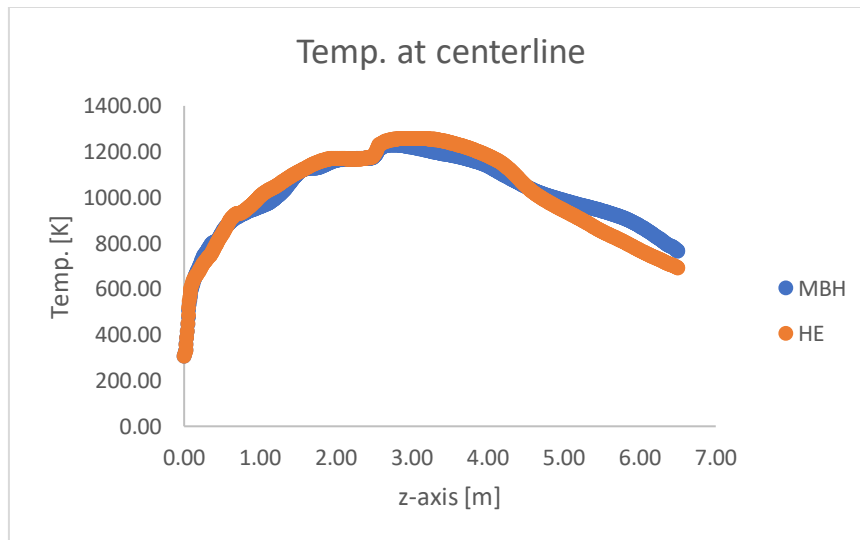


Figure 33: Plot of mean temperature sampled along the centerline, MBH vs. HE

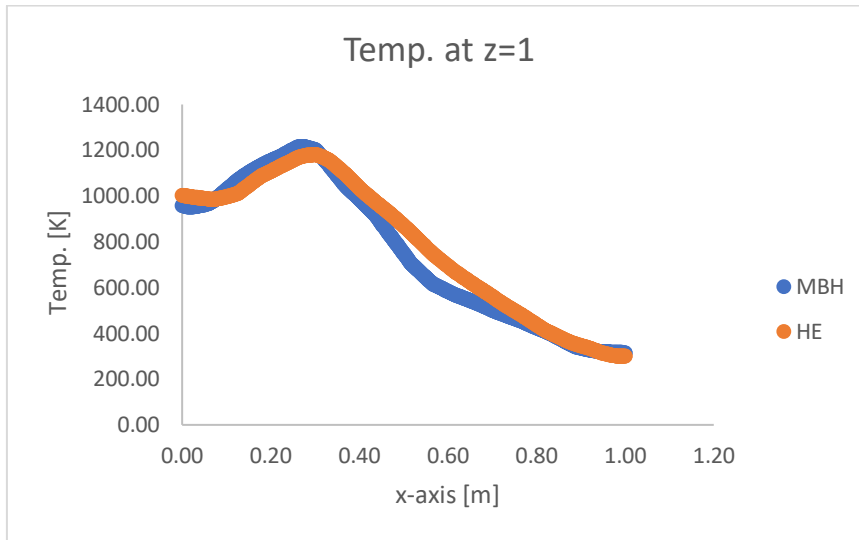


Figure 34: Plot of mean temperature sampled at z=1 m, MBH vs. HE

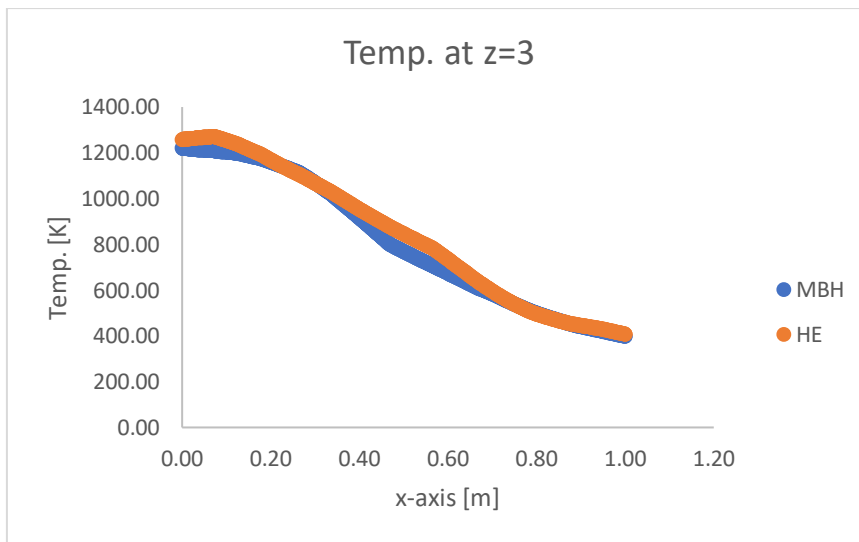


Figure 35: Plot of mean temperature sampled at z=3 m, MBH vs. HE

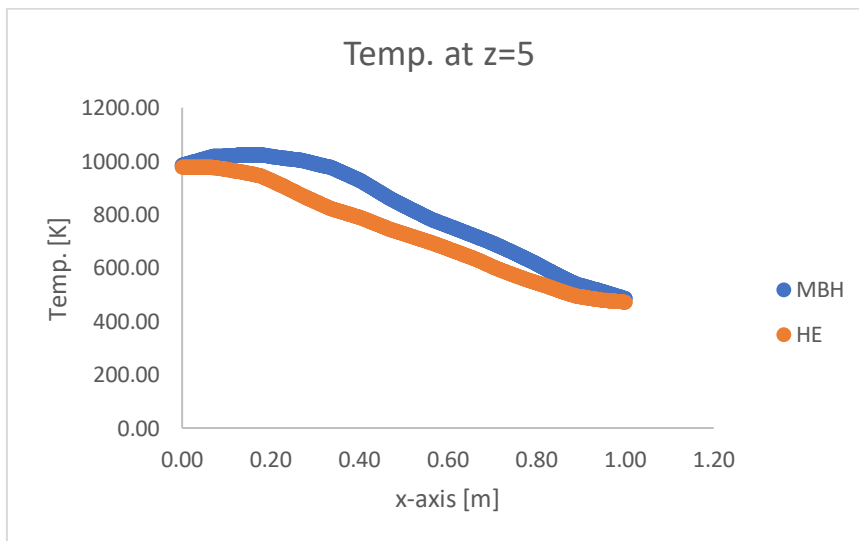


Figure 36: Plot of mean temperature sampled at z=5 m, MBH vs. HE

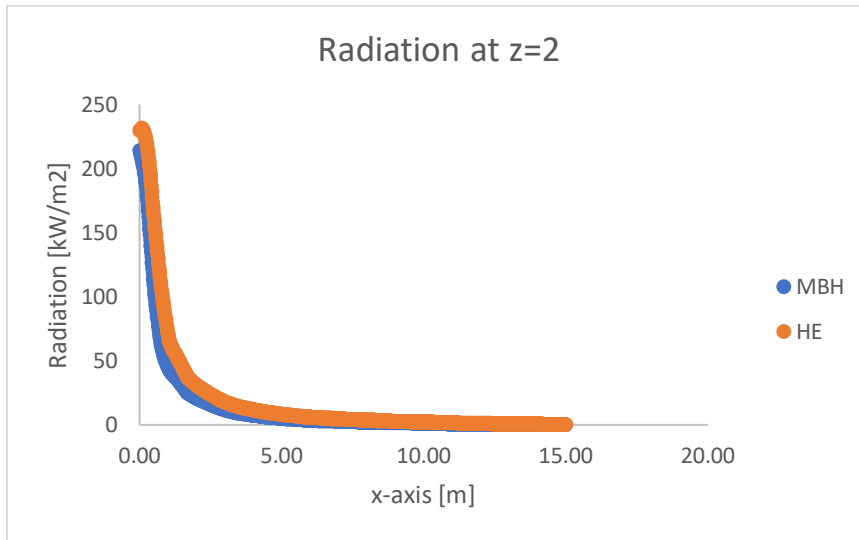


Figure 37: Plot of mean radiation sampled at $z=2$ m, MBH vs. HE

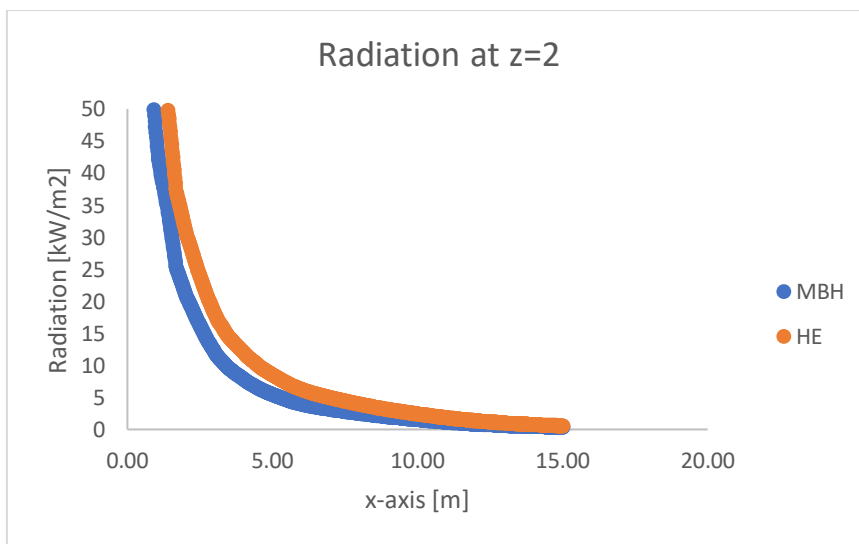


Figure 38: Plot of mean radiation sampled at $z=2$ m zoomed in, MBH vs. HE

Figure 38 is Figure 37 zoomed in on the y-axis in order to see the discrepancy between the two sets of data more clearly.

5.4 Conclusion from soot models comparison

Generally speaking, the HE and the MBH model agree with each other quite well in terms of pattern, judging from the temperature and radiation contours. Figure 36 shows the most discrepancy regarding the temperature. This behavior has been observed previously in the smaller pool fire, where more discrepancies between the models appear further away from the combustion surface. The results show that the HE model predicts the amount of soot present in the system more accurately than the MBH model. The reason why there is only one value for the radiation from the HE model is that the radiation is calculated from the soot mass fraction instead of volume fraction. It appears that perhaps the MBH model could be “tuned” to match empirical data by changing the soot particle density, which has a rather large range in possible values. This statement holds true for both soot models.

The HE model in fact performed beyond expectancy. This is exciting because the HE model requires less input than the MBH model. The MBH model requires the presence of C_2H_2 , C_6H_6 , C_6H_5 ,

and H₂ in the system. This requirement itself is a restriction on the combustion model available and the Chemkin code used. From experience, when using the CE model where the user does not have control over what species to include in the species list, these species never appear in the species list at the same time. Even when using the SDF model, this requirement is a big constraint on the Chemkin code used because normally only a very complete Chemkin code would include all the four species above, and these Chemkin codes may not always be available.

Although the HE model performed well, the remaining simulations were still conducted with the MBH model. The MBH model, although performed worse in this experiment, has been developed and used for decades. On the contrary, the HE model is a very young model and much more investigation is needed before it can be considered a reliable model.

6. Mesh resolution study

A total of five simulations were conducted for the mesh resolution study. These are five simulations with the exact same configuration, but different mesh size.

6.1 Simulation setup

6.1.1 Configuration

The configuration of the pool and the domain remain essentially the same from chapter 5. The diameter of the pool is still 2 meters, and the domain is 15 times the width and 10 times the height. The biggest difference is that now structures are added inside the pool. A top view of the configuration is given below.

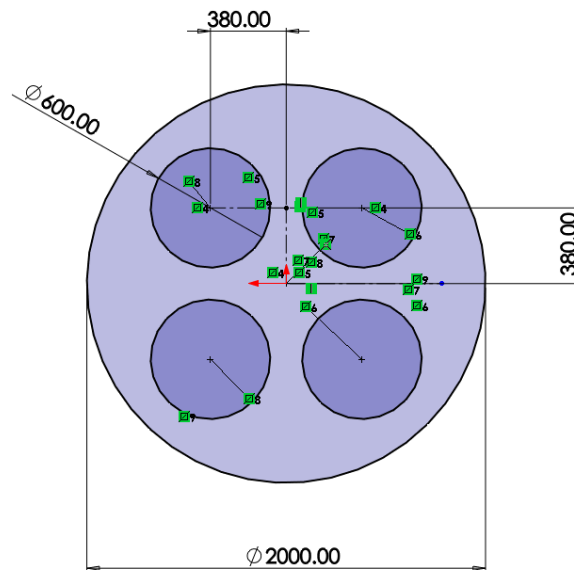


Figure 39: Pool and tanks configuration

This configuration is more or less modelled after an existing fuel storage facility in Schiphol airport. The diameter of the tanks are determined from how much area would be covered by the tanks in the pool. In the facility in Schiphol, 50% of the pool area is covered by the tanks. When this ratio is applied to the 2 meter pool here, the tanks would have a diameter of 700 millimeter. However, this resulted in a configuration where there are not enough space between the tanks and between the tanks to the wall, which may restrain the necessary airflow for combustion. Eventually, the diameter of the tanks are reduced to 600 millimeter, and the tanks are placed so that they are equidistant from each other and to the wall of the pool. The height of the tanks are also 600 [mm]. This is because the tanks in the Schiphol facility have a one to one height to diameter ratio.

The fuel and diameter of the pool are the same as from the previous chapter. However, since there are structures inside the pool now, the area of the pool has decreased, hence also the mass inflow. Taking this into account, the mass inflow used in this chapter is 0.1086 [kg/s].

6.1.2 Mesh

Figure 40 shows how the zones are constructed in the domain, and Table 3 tabulates the size of mesh used in each zone.

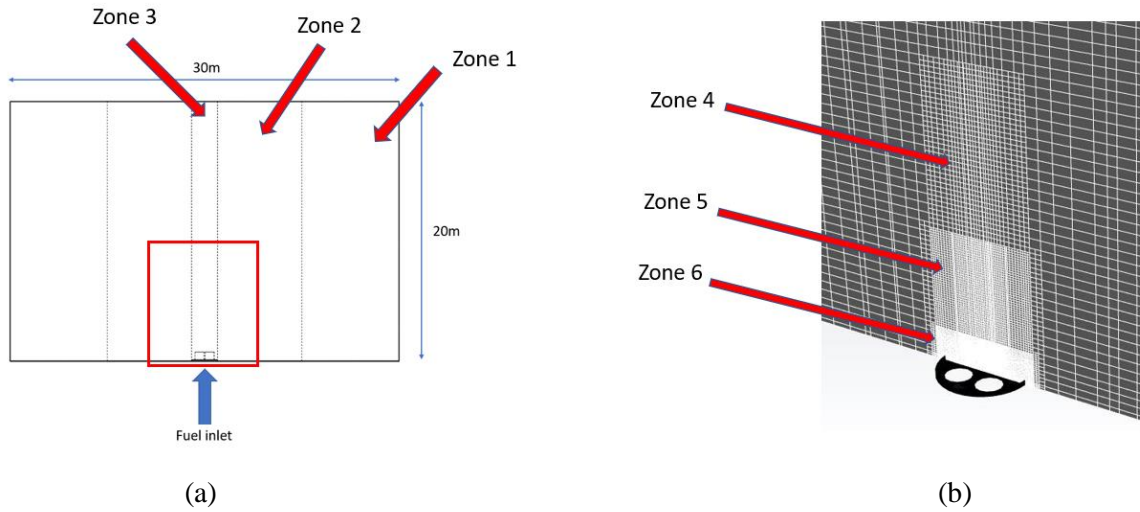


Figure 40: (a) domain setup (b) grid setup for the mesh resolution study

Table 3: Size of mesh used in each simulation

Simulation	zone	L	min. length in a cell [mm]
1,3x	1	3	682,5
	2	5	455
	3	10	208
	4	20	107
	5	41	52
	6	84	25
1,1x	1	4	577,5
	2	6	385
	3	13	176
	4	26	88
	5	52	44
	6	104	22
1x	1	4	525
	2	6	350
	3	13	160
	4	26	80
	5	52	40
	6	104	19
0,9x	1	4	472,5
	2	7	315
	3	15	144
	4	29	72
	5	59	36
	6	124	17

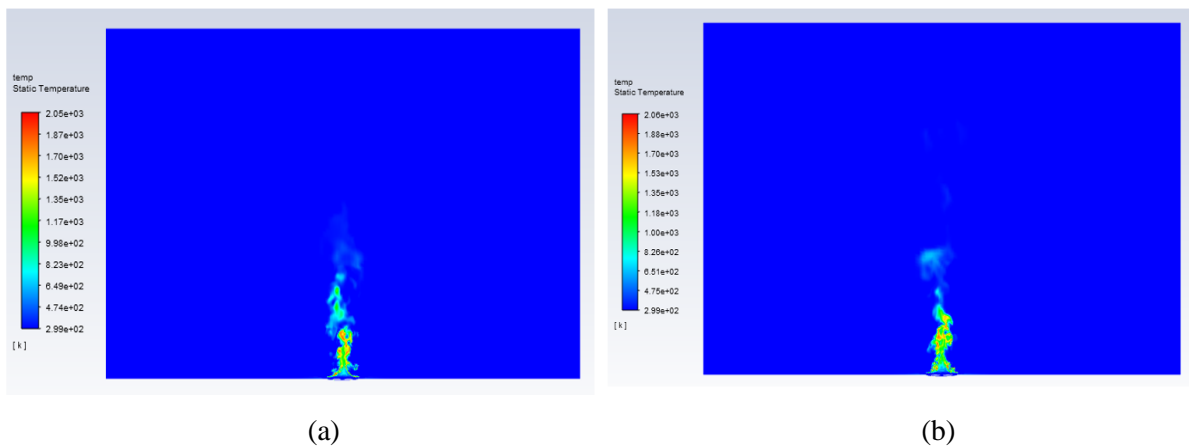
The L values shown in Table 3 are determined based on the recommendation of NIST, who conducted a validation study where the L value is between 4-16 [1], and of Ferng and Lin, who pointed out in their paper that a L value of 13 should suffice [10]. This is why in the 1x mesh, the L values for zone 1, 2, and 3 are between 4-13. However, based on the experience gained by Huygens from previous projects, this guideline will not suffice for regions with large gradients. This is why zone 4, 5, and 6, which are the zones where the flame is, are further refined. The refinement work is done by dividing the minimum length of a cell by 2. For example, in the 1x mesh, when going from zone 3 to 4, the minimum length of a cell goes from 160 [mm] to 80 [mm]. Unlike the mesh used previously for chapter 4 and 5, where the mesh is refined once in the flame area and another time very close to the combustion surface, the mesh used here is refined one more time between the two zones. This is to avoid having too large of a transition in cell size which may cause errors in the calculation.

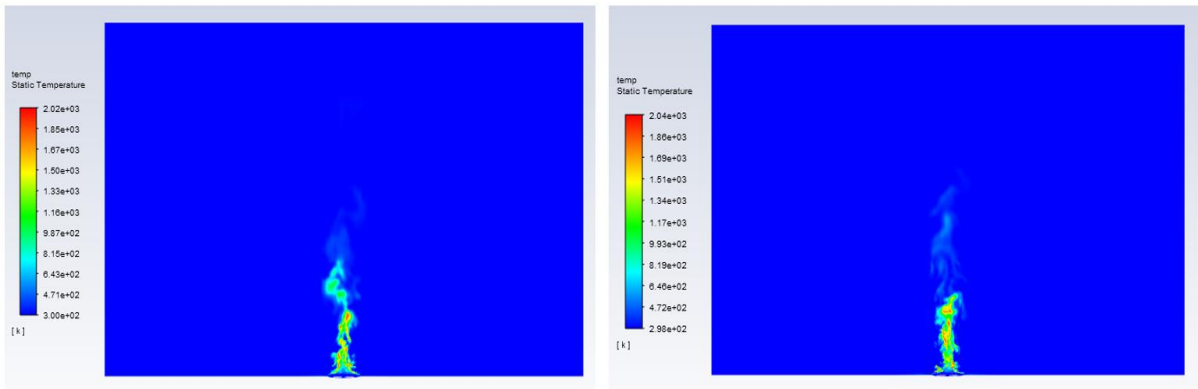
The 1x mesh simulation was the first simulation conducted and acts as a reference in this report. The 1.1x means that the mesh is coarsened by 10 percent from the 1x mesh. Taking the minimum length of a cell in zone 1 from the 1.1x simulation as an example, this value is simply the value from zone 1 of the 1x simulation multiplied by 1.1. The same rule applies to the rest of the simulations, hence the 0.9x simulation is a refinement study from the 1x simulation. Going coarser than the recommended value is avoided. This is why in most cases the lowest L value used is 4, except for the coarsest 1,3x mesh where the lowest L value used is 3. In areas where there are no flame, it is avoided to use a L value larger than 16. This is to avoid using unnecessary fine grid, which will result in a high number of cell counts.

As can be seen, the domain is divided into more zones than the mesh used previously. This is an attempt made to reduce the total number of cells in the model. However, this attempt did take into consideration that fine mesh is needed in the flame area, and the recommended 4-16 L value is taken into account as explained in the previous paragraph.

6.2 Results from the mesh resolution study

The temperature contours generated by the four different grids are shown below for demonstration purposes.





(c)

(d)

Figure 41: Temperature contour of (a)1x (b)1.1x (c)1.3x (d)0.9x mesh

When compared to the flames shown in Figure 29 and 26, the flames here appear to be smaller. This is because of the structures present inside the pool, which resulted in a smaller mass inflow of fuel.

Four sets of data are generated. The results are presented below.

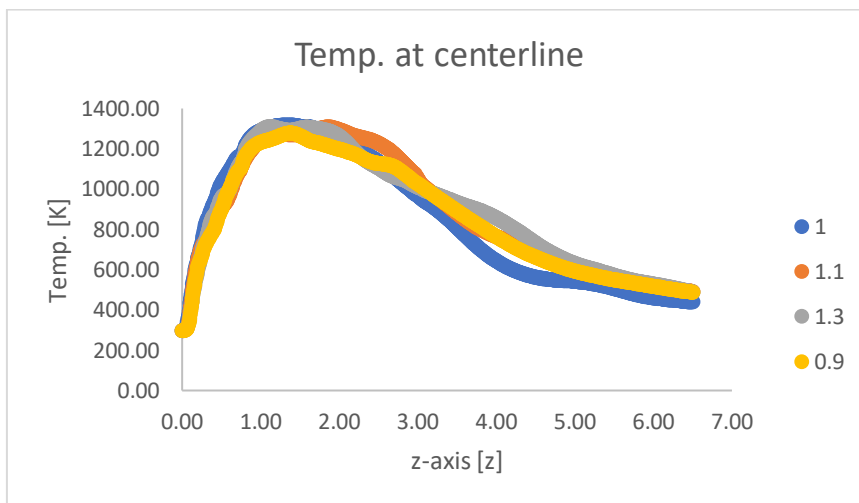


Figure 42: Plot of mean temperature sampled along the centerline, four sets of mesh

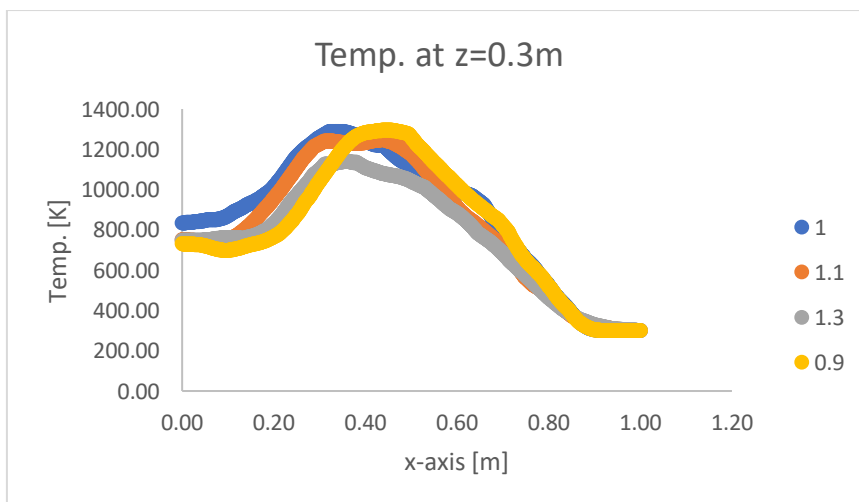


Figure 43: Plot of mean temperature sampled at $z=0.3$ m, four sets of mesh

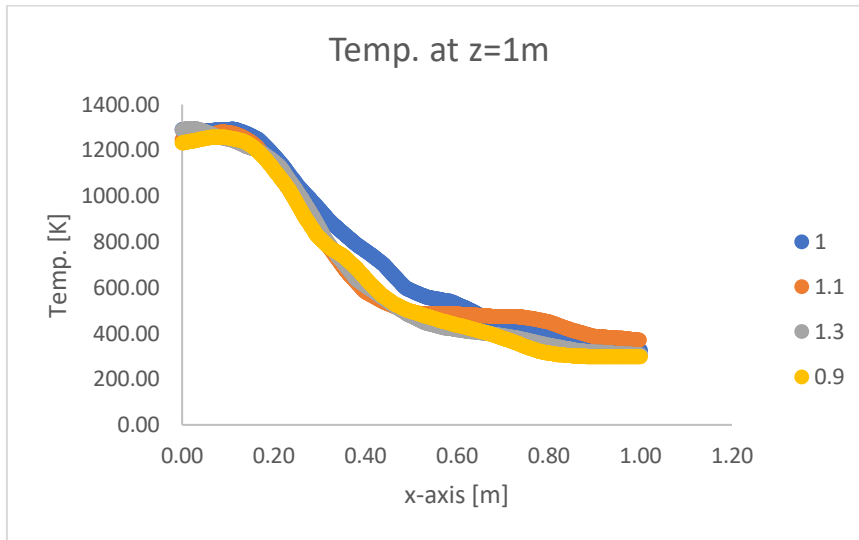


Figure 44: Plot of mean temperature sampled at $z=1$ m, four sets of mesh

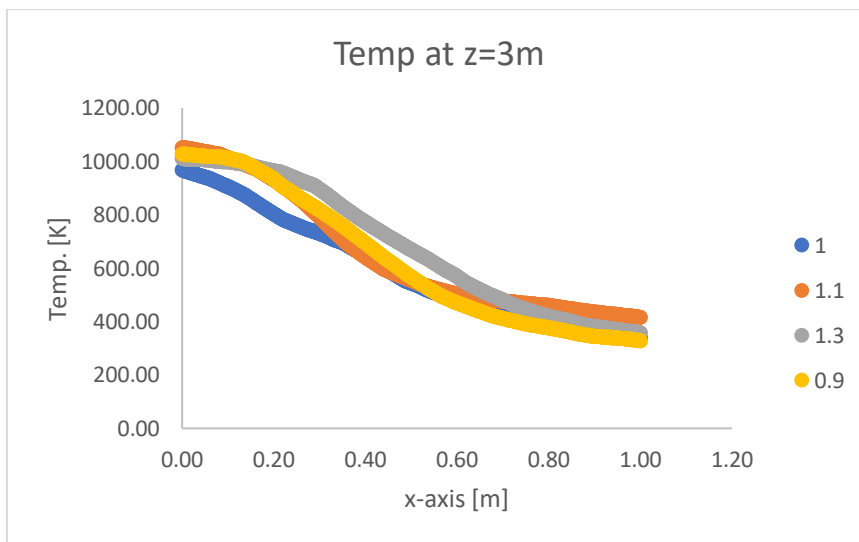


Figure 45: Plot of mean temperature sampled at $z=3$ m, four sets of mesh

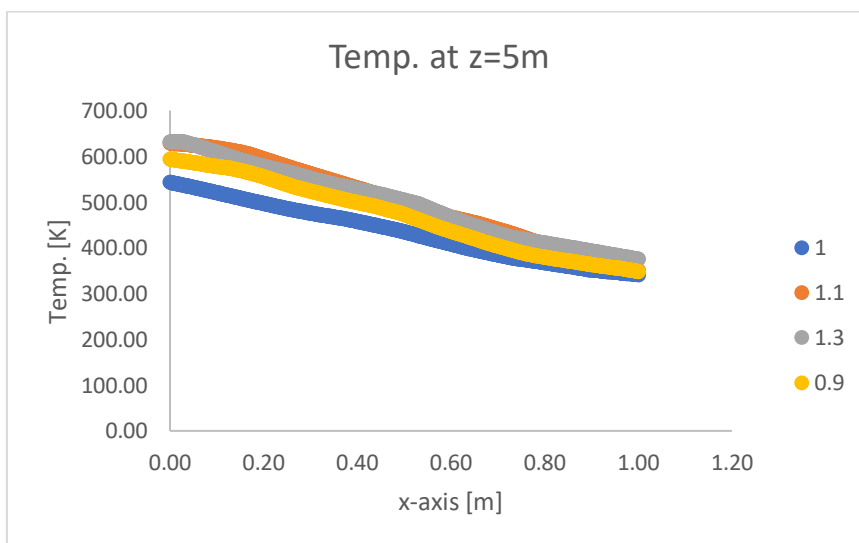


Figure 46: Plot of mean temperature sampled at $z=5$ m, four sets of mesh

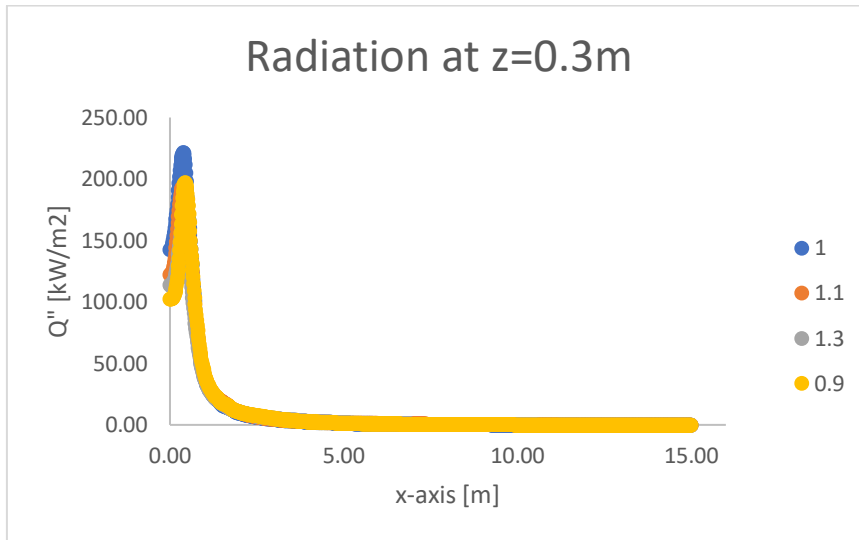


Figure 47: Plot of mean radiation sampled at $z=0.3$ m, four sets of mesh

The y-axis of the radiation contour in Figure 47 is adjusted to be in logarithmic scale in Figure 48 to examine more closely how well the results agree with each other. A horizontal red line is drawn at 3 [kW/m²]. This is because this value is a threshold used in experiments regarding the protecting capabilities of firefighting clothing [25].

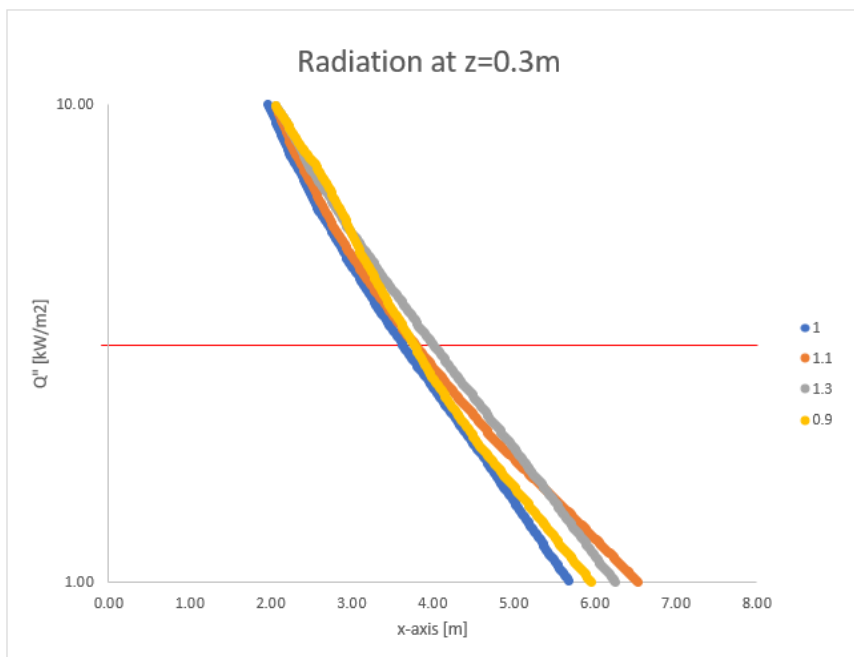


Figure 48: Plot of mean radiation sampled at $z=0.3$ m zoomed in, four sets of mesh

The distance where 3 [kW/m²] is sampled in each mesh is tabulated in the table below. The table is arranged so that the mesh goes from coarse to fine from left to right.

Table 4: Safety distance predicted by different mesh

Safe radiation intensity [kW/m ²]	Safety distance for different mesh resolution			
	1.3x	1.1x	1x	0.9x
3	4.1	3.87	3.71	3.83

In the radiation plot, the results agree with each other well closer to the fire. More discrepancies start to show at about 5 [m] in the radial direction. However, this is of minor concern since 3 [kW/m²] is the amount of radiation that a firefighter can safely withstand with protective clothing, and pass 5 [m] the radiation is already at a safe level and more discrepancy in the data is acceptable.

Generally speaking, the pattern of results agree with each other well between the four different mesh size. Theoretically speaking, the finest mesh would produce the most accurate result. However, mesh convergence is not observed and it is not clear here which mesh is generating the most accurate result. When going from the coarser 1.3x mesh to the finer 1x mesh, the safety distance seems to be converging to 3.71 [m]. However, when looking at the 0.9x mesh, the safety distance diverges. In order to investigate which result is the most accurate, or rather, if all of these results make sense at all, the macro length scale of the turbulences are examined and compared to the mesh sizes. If the mesh size proves to be smaller than the macro length scale of turbulences, then it can be concluded with more confidence that the results presented here show some predictive capability.

6.3 Examining macro length scale of turbulence

In order to confirm the validity of the results generated above, the macro length scale of turbulence is examined. The expression for the macro length scale of turbulence is given below:

$$L_R = \frac{k^{\frac{3}{2}}}{\varepsilon} \quad (11)$$

where k is the turbulent kinetic energy, and ε is the rate of dissipation. This is simple to execute in Fluent in the case of a RANS simulation where k- ε model is used for turbulence modelling. In this case, both variables are modelled and are standard outputs of the k- ε model, which can be directly used to calculate the length scale in the entire domain. However, this is not the case for a LES simulation. For a LES simulation, k and ε both need to be estimated, both in resolved and unresolved domain. This proves to be a challenging task from an execution point of view. For the purpose of this project, it is assumed that the macro length scale of turbulence should be similar in a domain, no matter the simulation is conducted in RANS or LES. A RANS simulation will be conducted with the configuration used in the mesh resolution study to estimate the macro length scale in the domain.

6.4 Results from examining macro length scale of turbulence

The macro length scale of turbulence of the entire domain is shown in Figure 49 below,

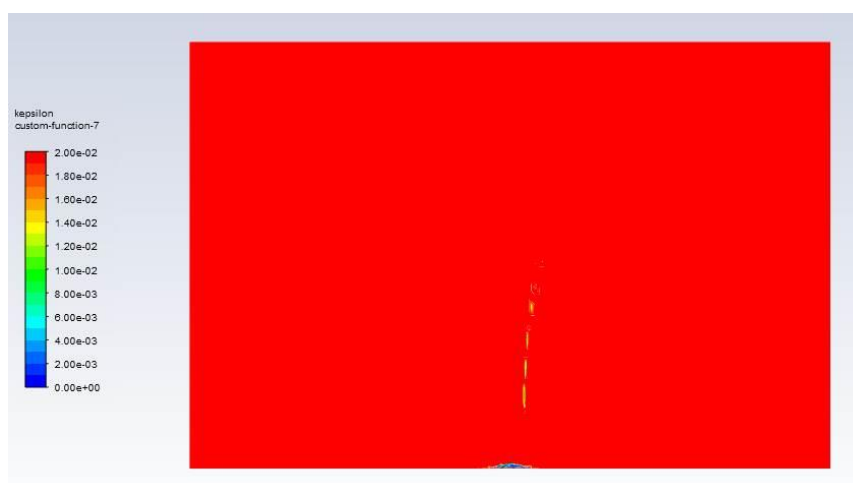


Figure 49: Macro length of turbulence in the domain

The maximum value is set to 20 [mm] in this figure, which is the finest mesh size used in the 1x mesh from the mesh size study. This is done to focus on the area where the smallest length scale should be, which is the area of the flame. As can be seen, the length scale is in fact smaller than the grid size very close to the combustion surface. Other parts of the domain are also examined and for the most part the turbulence is larger than the mesh size used, except for the small yellow spots that can be seen in the figure. These yellow small spots are on the edge of the flame and they are either small turbulences at this location, or they could be some calculation error in the domain.

It must be mentioned that the validity of these results are in fact highly questionable. The residual of the simulation is very poor, indicating that this simulation could be very far from the reality. The reason is again believed to be the unsteady nature of pool fires. Pool fires simply cannot be predicted by a RANS simulation. Another evidence indicating that this simulation could be very wrong is the predicted flame height, which is shown in Figure 50

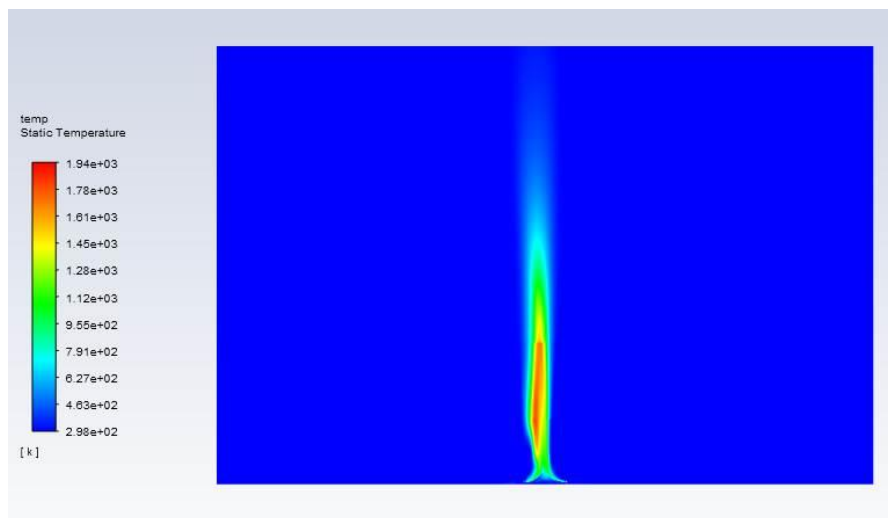


Figure 50: Temperature contour, mesh resolution study in RANS

The flame height in this simulation appears to be more than 10 meters. This is much taller than the theoretical value, which is about 6 meters. The temperature is also a lot higher than the theoretical value, which is about 1000°C for kerosene-based fuels [13].

Although the above results are unsatisfactory, this project proceeds with investigating the area just above the combustion surface that is most likely to have cells that are inadequately small. The mesh is refined again in certain areas until the computer resources are depleted and another run of simulation is conducted. The results produced will be compared to the four simulations conducted previously to examine the validity of the results.

6.5 Further mesh refinement

The result from section 6.4 show that the smallest length scale of turbulence close to the combustion surface is about 0.9 [mm]. This poses difficulties in modelling as generating cells this size would result in a very high total number of cell counts. Multiple attempts were made to push the cell size to this scale. However, a compromise must be made between the cell size and the exceedingly long calculation time resulted from a high number of cell counts. The first attempt was to generate a mesh as the diagram depicts below

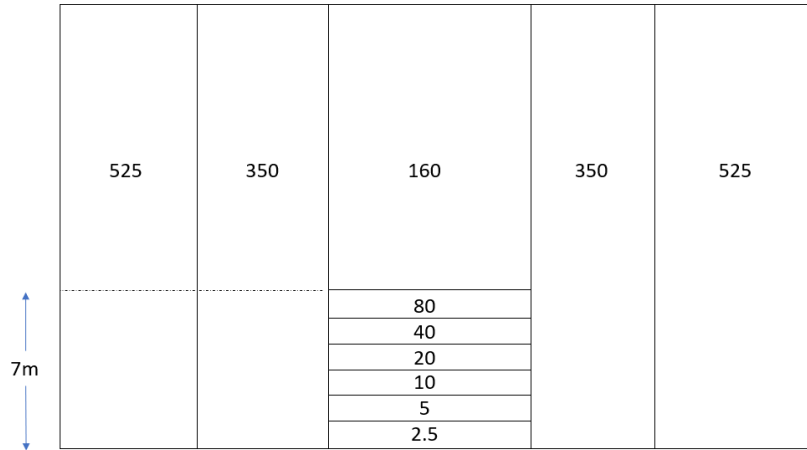


Figure 51: Attempted mesh resolution for further mesh refinement (units in mm)

The numbers shown in the figure represents the minimum length of a cell used in that zone. This mesh setup is based on the 1x mesh, with the flame area further refined. The first layer of mesh in the flame area is 2.5 [mm] high, which is roughly the height of the problematic area shown in Figure 49. The reason for generating so many layers is to avoid a sudden jump of sizes between layers. As can be seen, the finest layer composed of 2.5 [mm] cells, which are still quite a lot larger than the target 0.9 [mm]. The configuration is set up this way because, based on experience, 0.9 [mm] cells are most likely not achievable with the computing power in hand. Nevertheless, this attempt still ended in an exceedingly high number of total cell count. After generating the 5 [mm] layer, the total cell count was already at 170 million cells. The computer available in hand crashed when the 2.5 [mm] layer was being generated due to insufficient RAM. Furthermore, a simulation with 170 million cells would take years to collect 5 cycles of data.

Many attempts followed to slowly coarsen the mesh, which all ended in cell counts that were deemed too high. In the end, the simulation was conducted with the mesh shown below

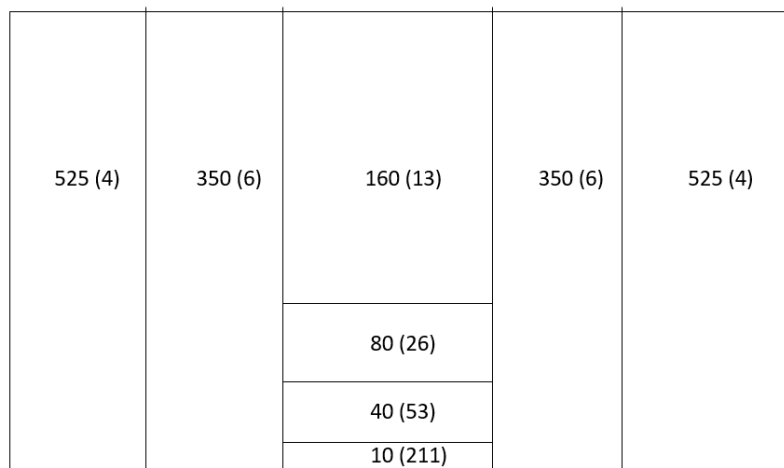


Figure 52: Mesh resolution used for further mesh refinement (units in mm)

The values shown in the parentheses are the corresponding L values. The size of the finest layer is 10 [mm], which is far from the 0.9 [mm] target. However, this was a necessary compromise made between the fineness of cells and the time available in hand. This configuration resulted in a total of 4.4 million cells. Although not achieving the ideal cell size, this simulation will be composed of the finest mesh in this project. It is expected that the blue area shown in Figure 49 will not be completely resolved.

Nevertheless, it is important to see whether the results still show a similar trend. Or, if differences exist between this grid, how large is the difference between this grid and the other grid.

6.6 Results from further mesh refinement

The temperature contour generated from this grid is given in Figure 53 for demonstration purposes.

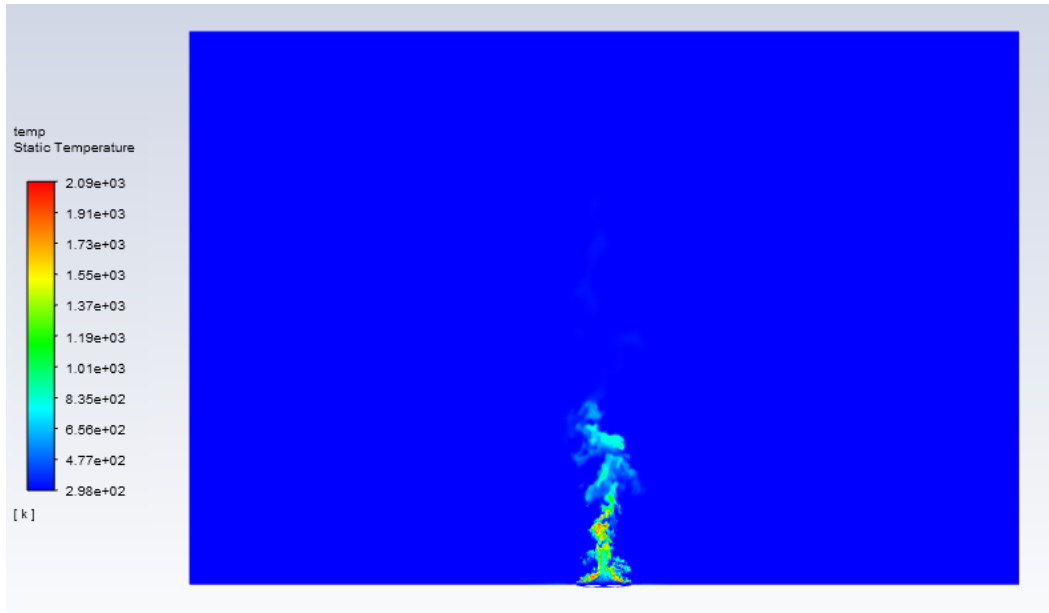


Figure 53: Temperature contour of the further refined mesh

The results produced by this mesh is presented below. The results are plotted together with the results from the mesh resolution study for comparison. The results from this simulation have been denoted 1R, because it is a grid refined from the 1x mesh.

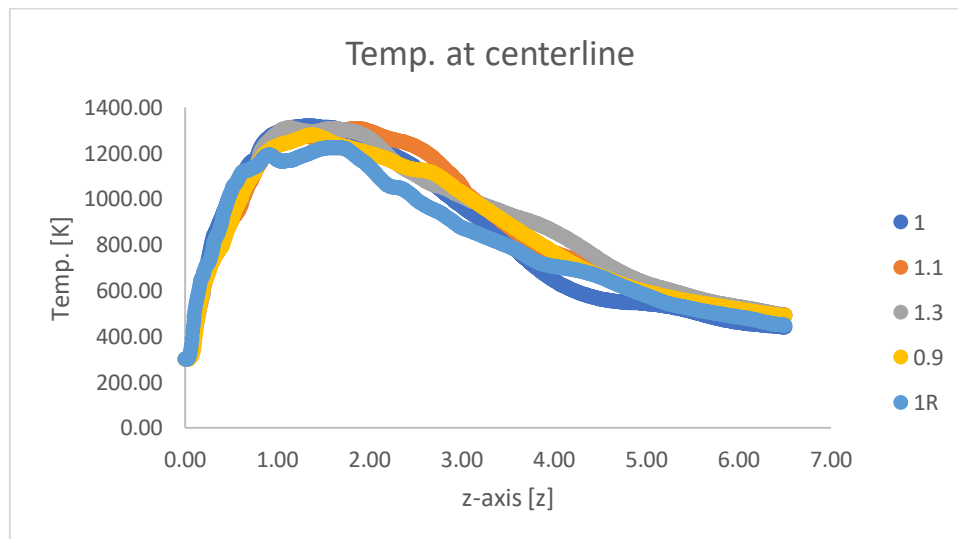


Figure 54: Plot of mean temperature sampled along the centerline, with 1R mesh

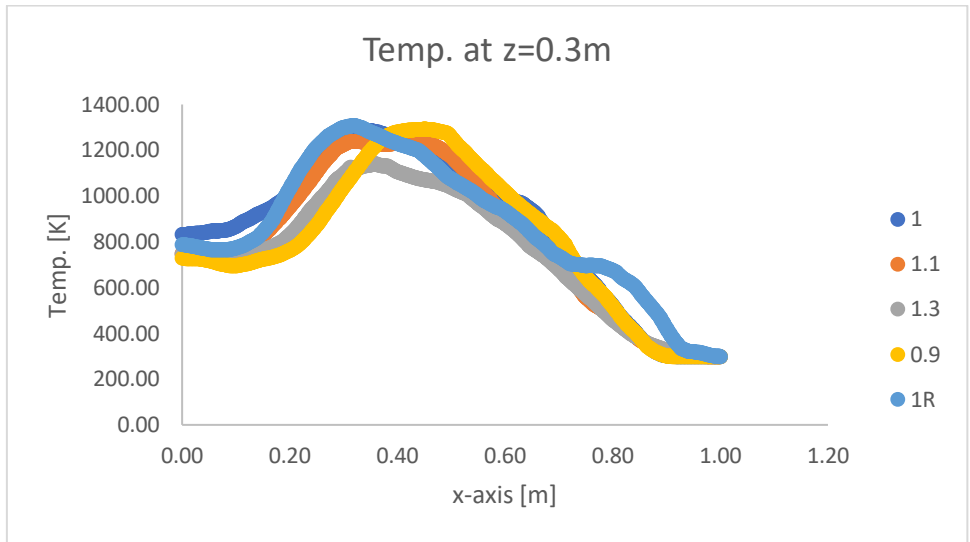


Figure 55: Plot of mean temperature sampled at $z=0.3$ m, with 1R mesh

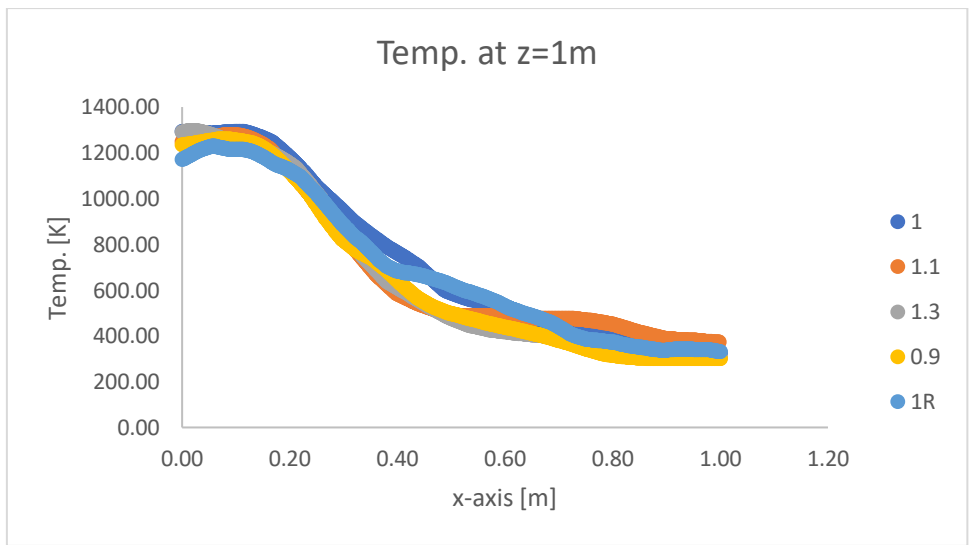


Figure 56: Plot of mean temperature sampled at $z=1$ m, with 1R mesh

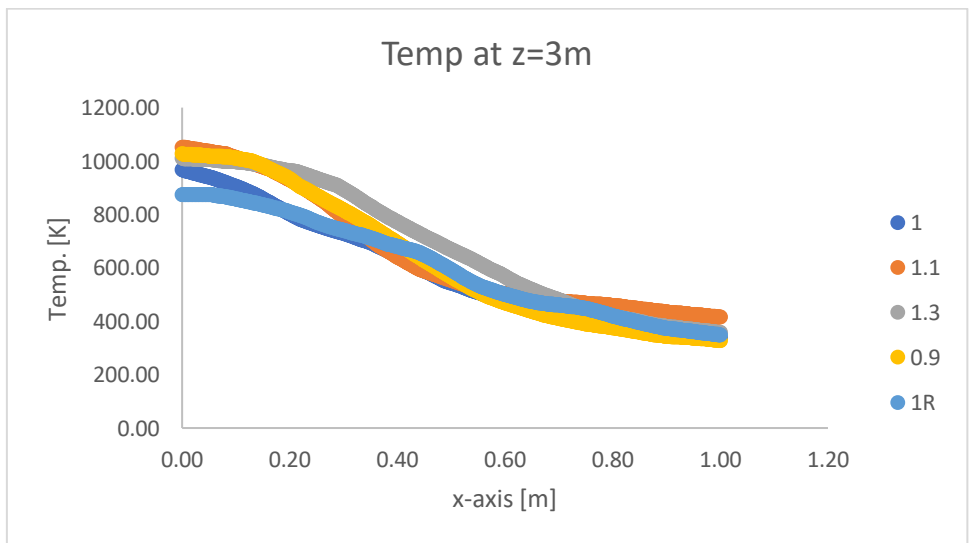


Figure 57: Plot of mean temperature sampled at $z=3$ m, with 1R mesh

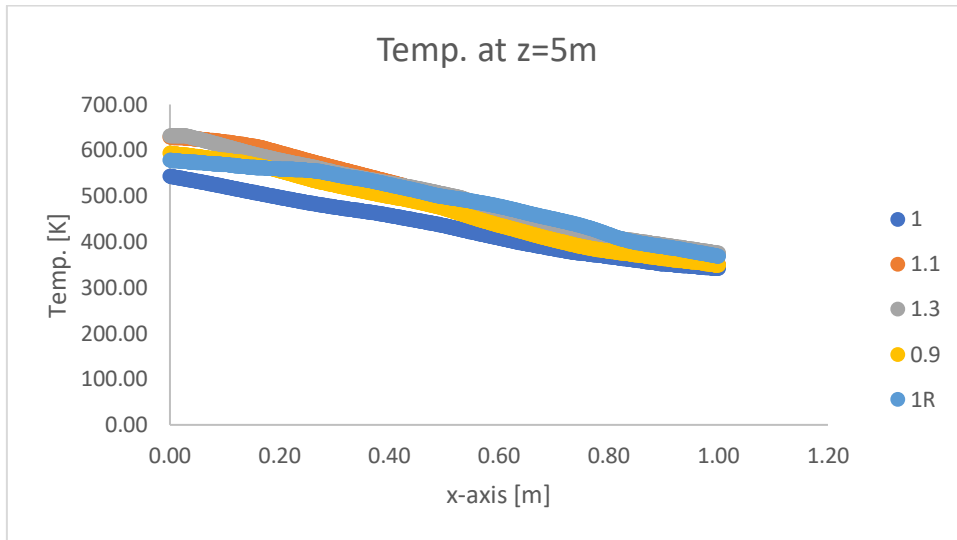


Figure 58: Plot of mean temperature sampled at $z=5$ m, with 1R mesh

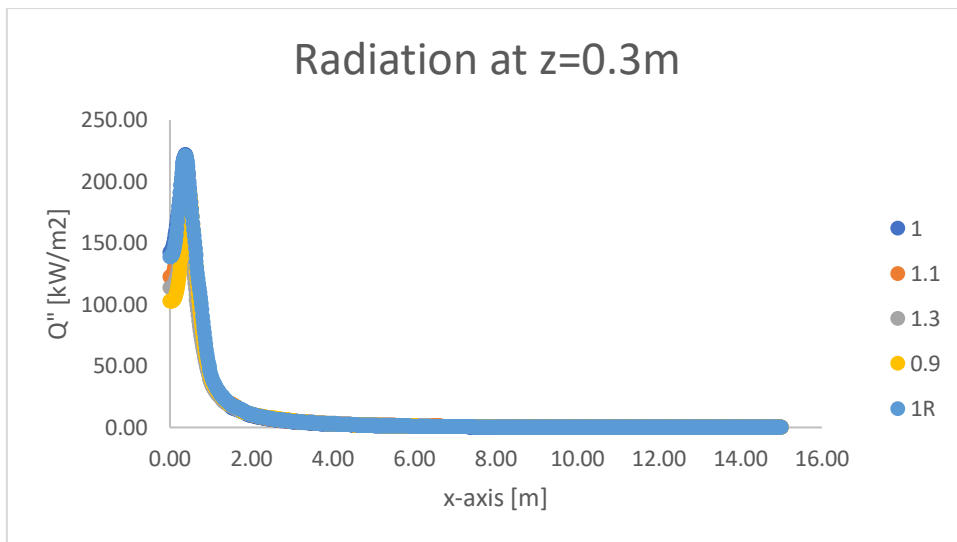


Figure 59: Plot of mean radiation sampled at $z=0.3$ m, with 1R mesh

The scale of Figure 59 is adjusted so that the 3 [kW/m²] can be seen more clearly. This is shown in Figure 60.

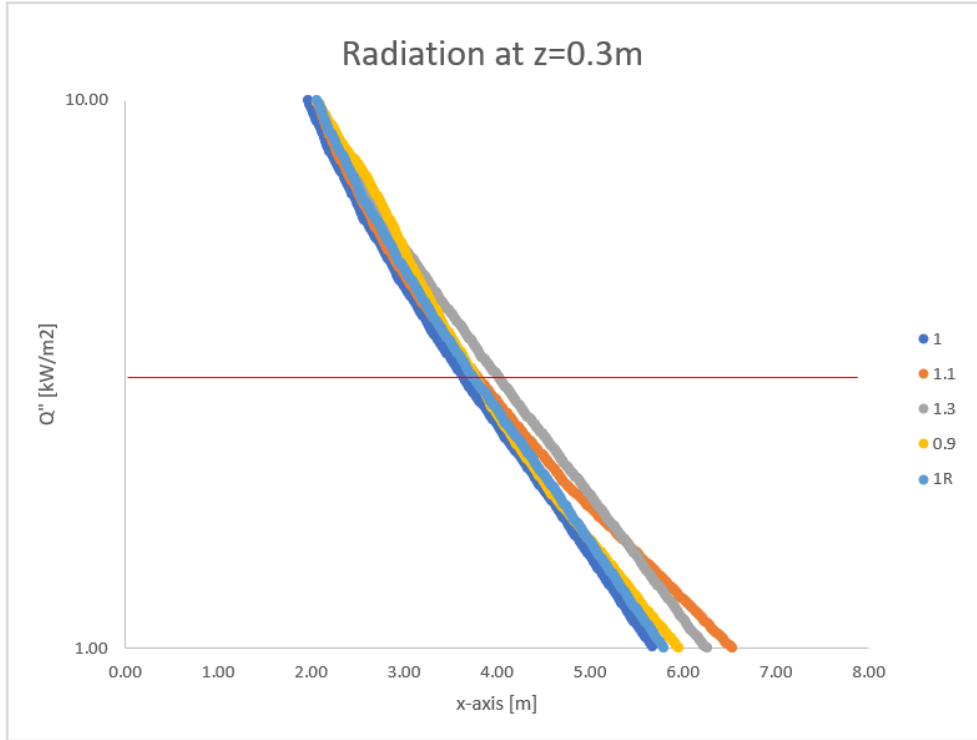


Figure 60: Plot of mean radiation sampled at $z=0.3$ m zoomed in, with 1R mesh

The data for the radiation intensity at $3 \text{ [kW/m}^2\text{]}$ is tabulated and shown below for better judgement. The distance where $3 \text{ [kW/m}^2\text{]}$ is sampled in each mesh is tabulated in Table 5.

Table 5: Safety distance predicted by different mesh, with 1R mesh

Safe radiation intensity [kW/m ²]	Safety distance for different mesh resolution				
	1.3x	1.1x	1x	0.9x	1R
3	4.1	3.87	3.71	3.83	3.83

From the table, it can be seen that the result from the 1R mesh agrees with the 0.9x mesh. This is a sign that results are starting to converge. The largest discrepancy exists between the 1x and the 1,3x mesh. The 1x mesh predicts the radiation to be at $3 \text{ [kW/m}^2\text{]}$ at a distance 3.71 [m] away from the center of the pool, and the 1.3x mesh predicts a distance 4.10 [m] away. This discrepancy should be dealt with a safety factor.

6.7 Conclusion from mesh resolution study

The five different mesh resolution all demonstrated similar trends. This is surprising as the coarsest mesh was expected to behave quite differently from the finest mesh, considering how much finer the finest mesh used is. Mesh resolution was smaller than the macro length scale of turbulence everywhere but at the lower flame-surface close to the pool. It was a pity that the ideal mesh resolution cannot be reached to ensure that the mesh resolution is smaller than the macro length scale of turbulence everywhere in the flow field. However, from the current results, convergence seems to appear in the results when the 1R mesh is used when looking at the $3 \text{ [kW/m}^2\text{]}$ radiation intensity. No large difference in the safety distance is expected even if a finer mesh is used, considering that the current mesh is already quite fine and the fact that the area with unresolved turbulence is rather small.

In all the models used above, a coarse mesh is used for area further away from the flame. This decision appears to be acceptable as long as the L number stays within the value recommended by NIST. In the 1,3x mesh simulation, the lowest L number used is 3 and the results produced still followed the same trend as all the other results. This demonstrates that the mesh resolution need not be very fine further away from the combustion. This is helpful when the total number of cell counts needs to be kept low.

At the regions with flame, the finest mesh used ranges from L equals 84 to 211. Although it is known that turbulences are not completely resolved close to the combustion surface even with L=211, the results did not show large disagreement among each other. This is an indication that, for engineering purposes, a small amount of turbulences not being correctly resolved may be acceptable.

7. Conclusion

7.1 Comparison of combustion models

Although not intended originally, it was confirmed that the details of pool fire cannot be captured by RANS simulation. Figure 10 demonstrated that pool fires do not reach a steady-state and cannot be modelled by RANS simulation. This eliminates the future endeavors of using the UDF model to predict the behavior of pool fires even though it is able to predict the slow-forming substances through a statistical approach. If the formation of these substances must be predicted, models under the species-transport category must be used.

This project did not unveil the full capabilities of the EDC model. The EDC model is the most complete model in the sense that it makes no simplifying assumptions in its calculation regarding chemistry, hence offering the most flexibility in terms of control over the chemical process for the user. However, this does imply that a certain level of chemical knowledge may be required to correctly manipulate this model. Nevertheless, if the target of investigation were soot formation and the accuracy of data is important, then the EDC model may become the only model available capable for this purpose.

The comparison between the CE and SDF did not conclusively show which model is more accurate. Before the results were compared, it was expected that the SDF model will be more accurate than the CE model since it takes the chemical mechanisms and the scalar dissipation rate into account. One possible reason why this isn't the case is because the pool tested here is only a 0,3 [m] pool. It is suspected that a pool this size would not cause much air entrainment, resulting in a small scalar dissipation rate as was shown in Figure 13. Since the scalar dissipation rate is small, one of the biggest advantages of the SDF model is diminished. The project went ahead with the SDF model simply because it allows more control over the chemical process and enables more availability of the soot models.

7.2 Comparison of soot models

The soot models comparison showed unexpected results. The HE model managed to predict soot volume fraction more accurately than the MBH model. This is exciting because the HE model is simple to use in terms of software execution. However, the HE model is a new model and more tests should be conducted before it can be treated as a valid model. The results of the soot models comparison have shown that it is perhaps possible to tune these models to match the results of experiments. This of course also requires more tests before it can be done with confidence.

7.3 Mesh resolution study

The current results of the mesh resolution study are rather positive. Although some discrepancies do exist between the results produced by different grid, the trend of these results agree with each other and the discrepancies are not in unacceptable magnitude. The results are starting to show sign of convergence when the 1R mesh is used. It was unfortunate that the ideal mesh resolution cannot be reached in the study of further mesh refinement. However, as the contour of macro length scale of turbulence has shown, most of the turbulences in the domain are properly resolved. It is unlikely that the results produced by a finer mesh will be drastically different from the current results. Nevertheless, for practical purposes, the uncertainties mentioned here will be covered by a safety factor to ensure the safety of firefighting personnel. Based on these results, it appears that the non-dimensional expression for mesh resolution, published by NIST, could be used for the majority of the flow field, with the area close to the surface of combustion further refined.

8. Discussion and recommendations

Throughout the report, the convergence of results are checked with the “five cycles rule”. It must be emphasized that the “five cycles rule” is determined simply because of the limitation in time and computational power available. Intuitively speaking, five cycles of pulsation is an extremely short period of time for a fire to burn and data should definitely be collected over a longer period of time when possible. Even though in this report the aforementioned methods of checking convergence are applied to almost all the simulations and these simulations have passed this check, it doesn’t necessarily mean that these simulations have all converged statistically. Because of the unsteady nature of pool fires, it is possible for simulations to diverge again later in time. There is no clear guideline indicating how long this type of simulations should run. Nevertheless, a much longer period of data collection is needed in order to have more confidence in the results.

Although computationally expensive, the EDC model is a very powerful model that is capable of capturing the slow chemical processes such as the formation of the pollutants. This is an important feature if future projects are formed to investigate the formation of soot in pool fires. This is potentially a very important issue to be investigated since soot is known to be related to the thermal radiation, which ultimately affects the safety of the fire brigade. In order to execute this investigation, the reason for flame extinguishment in a LES simulation with the EDC model must first be found. A good place to start would be to use time steps that match the chemical time scales in reality. Fast chemical processes happen at a time scale that ranges between 10^{-6} to 10^{-8} second [26], and time step this size may be needed to correctly model combustion with the EDC model. Another option is to try grid size that is much finer, on the scale these chemical reactions actually occur. As can be imagined, testing either of these possibilities may require extensive computational power.

The CE and SDF models comparison conducted in this report did not show clear signs which model is more accurate. One possible alternative is to conduct the comparison again, but with a bigger pool. It is suspected that a pool that is 0,3 meter in diameter does not result in much air entrainment, hence not producing a high rate of scalar dissipation, as was seen in Figure 13. In this situation, the major advantage of the SDF model over the CE model is diminished.

The newly developed HE model has shown promising results in this project. However, as mentioned before, more tests should be conducted before it could be considered a trustworthy model. First of all it should be applied to different fuels. JP8 is a very sooty fuel, it would be beneficial to see how the model performs with a less sooty fuel. It would also be valuable to see how this model performs when it is applied to different size of pools. For one, the dominant mode of heat transfer is different when the diameter of the pool is different [6]. It is important to confirm that the model will perform as expected under different circumstances. Secondly, since this model is newly developed, it is good to apply this model to different configurations to build up a database of its own to see its strength and weakness. All these suggestions are best done when experimental data is available so that the results can be compared.

One of the next steps of the mesh resolution study would be to make the pool larger and the geometry more complicated, both in favor of making the computer models more realistic. Fuel storage facilities in reality could contain 10+ tanks, with diameters larger than 10 meters. Reaching this goal may require a lot of intermediate steps such as gradually increasing the pool diameter, gradually increasing the number of tanks and so on because the tips mentioned in chapter 3.7 may not directly apply to a pool that is much larger.

Regarding the effects of grid size, it is unfortunate that finer mesh resolution cannot be reached for practical reasons. This should be fulfilled in order to resolve all turbulences in the domain so that

full confidence in the results produced so far can be gained. The accuracy of the calculated turbulence macro length scale should also be improved. This is to say that the macro length scale check should ideally be conducted in LES simulation instead of RANS simulation.

The fact that the turbulences are not properly resolved close to the surface of combustion may result in underestimation of the gradients in this region. This may be tied to the issue discovered in chapter 4, where the flame burns too cold at the center. It would be beneficial if the cell size in this region could be reduced to the macro length scale of turbulence, which is approximately 0.9 [mm]. Doing so would provide the missing piece of information to the mesh resolution study, which is to see the results produced by a flow field with all the turbulences being correctly resolved, and to either fix, or eliminate one potential factor, for the issue of the simulated flame burning too cold in the center. However, based on current results, this doesn't seem to create a problem, especially if the main focus is located on the 3 [kW/m²] threshold. The results produced with L=211 did not make a big difference with the results produced with L=84. This is an indication that perhaps the mesh used in this region can be coarser, which would be very helpful in reducing the total number of cell count.

Judging from Figure 60, a safe distance for the fire brigade to stand would be roughly 4 meters away from the pool if they were to extinguish a 2 meter diameter pool fire. However, the results presented in this report are all averaged over time, which means that the pulsating behavior of the flame is not reflected in the shown data. There could be moments in time where the safety distance is larger than 4 meters. In order to take this uncertainty into account, a safety factor should be used when translating the data to the actual safety distance used by the fire brigade. Another reason why a safety factor is necessary is the fact that uncertainties, such as the unresolved turbulences in the domain, exist in the data obtained. This implies that the accuracy of results produced should be interpreted with caution and a safety factor should be used when applying these results to the industry.

Ideally, the data generated by CFD should be validated with experiments. This is difficult in the case of large pool fires. It would be ideal if some form of scaling guideline exists so that the behavior of large scale pool fires can be extrapolated from the existing small scale pool fire data. This idea is similar to dimensional analysis in the field of fluid mechanics, where the behavior of a large airfoil can be predicted by testing a smaller airfoil if certain variables such as the Reynolds number can be scaled accordingly. If the crucial factors that affect the behavior of a pool fire can be established and a similar analysis can be developed, it could complement the existing work of CFD and at the same time be a useful analytical tool in CFD analysis.

References

- [1] K. McGratten, S. Hostikka, R. McDermott, J. Floyd, C. Weinschenk and K. Overholt, "NIST Special Publication 1019, sixth edition. Fire Dynamics Simulator User's Guide," National Institute of Standards and Technology. VTT Technical Research Centre of Finland., 2013.
- [2] DMI, Disaster Management Institute, Bhopal, "Types of major chemical/industrial hazards - Fire," DMI, Disaster Management Institute, Bhopal, 2020. [Online]. Available: <http://www.hrdp-idrm.in/e5783/e17327/e27015/e27713/>. [Accessed 11 July 2020].
- [3] M. Girdhar, "Jaipur Fire and its Environmental effects," in *Esri India User Conference*, New Delhi, 2011.
- [4] BS reporter, "Business Standard," IOC Jaipur fire due to lack of safety measures: Probe, 21 January 2013. [Online]. Available: https://www.business-standard.com/article/companies/ioc-jaipur-fire-due-to-lack-of-safety-measures-probe-110020300031_1.html. [Accessed 12 August 2020].
- [5] T. Poinso and D. Veynante, *Theoretical and Numerical Combustion*, third edition, Bordeaux: Aquaprint, 2012.
- [6] P. J. DiNunno, D. Drysdale, C. L. Beyler, W. D. Walton, R. L. Custer, J. R. J. Hall and J. M. Watts, *SFPE Handbook of Fire Protection Engineering*, Quincy: National Fire Protection Association, 2002.
- [7] D. Stroup and A. Lindeman, "Verification and Validation of Selected Fire Models for Nuclear Power. NUREG-1824, supplement 1," United States Nuclear Regulatory Commission, Washington, DC, 2013.
- [8] ANSYS Inc., "ANSYS Fluent Theory Guide 2019 R1," ANSYS Inc., Canonsburg, 2019.
- [9] T. Frank, "When to use bounded Second Order Implicit Time Integration in Fluent?," ResearchGate, 20 December 2019. [Online]. Available: https://www.researchgate.net/post/When_to_use_bounded_Second_Order_Implicit_Time_Integration_in_Fluent. [Accessed 12 July 2020].
- [10] Y. Ferng and C. Lin, "Investigation of appropriate mesh size and solid angle number for CFD simulating the characteristics of pool fires with experiments assessment," *Nuclear Engineering and Design*, vol. 240, no. 4, pp. 816-822, 2010.
- [11] N. Peters, *Turbulent Combustion*, Cambridge: Cambridge University Press, 2000.
- [12] ANSYS Inc., *Lecture 09: Thermal Radiation in combustion*, ANSYS Inc., 2016.
- [13] U.S. Nuclear Regulatory Commission Office of Nuclear Reactor Regulation, "Fire Dynamics Tools: Quantitative Fire Hazard Analysis Methods for the U.S. Nuclear Regulatory Commission Fire Protection Inspection Program," U.S. Nuclear Regulatory Commission Office of Nuclear Reactor Regulation, 2004.

- [14] A. Hamins and A. Lock, "NIST Technical Note 1928: The Structure of a Moderate-Scale Methanol Pool Fire," U.S. Department of Commerce, 2016.
- [15] R. P. Lindstedt and M. P. Meyer, "A Dimensionally Reduced Reaction Mechanism for Methanol Oxidation," *Proceedings of the Combustion Institute*, vol. 29, no. 1, pp. 1395-1402, 2002.
- [16] R. Barlow and J. Frank, "Piloted CH₄/air flames C, D, E, and F-release 2.1," Sandia National Laboratories, 2007.
- [17] H. Pitsch and H. Steiner, "Scalar mixing and dissipation rate in large-eddy simulations of non-premixed turbulent combustion," *Proceedings of the Combustion Institute*, vol. 28, pp. 41-49, 2000.
- [18] H. Zhong and M. F. Modest, "Evaluation of the Planck-mean absorption coefficients from HITRAN and HITEMP databases," *Journal of Quantitative Spectroscopy & Radiative Transfer*, vol. 73, no. 6, pp. 649-653, 2002.
- [19] N. Smith, J. Gore, J. Kim and Q. Tang, "Radiation Models," TNF Workshop, 23 January 2003. [Online]. Available: <https://tnfworkshop.org/radiation/>. [Accessed 3 June 2020].
- [20] K. Wakatsuki, G. Jackson, A. Hamins and M. Nyden, "Effects of fuel absorption on radiative heat transfer in methanol pool fires," *Proceedings of the Combustion Institute*, vol. 31, no. 2, pp. 2573-2580, 2007.
- [21] J. de Ris, "Fire radiation-A review," *Symposium (International) on Combustion*, vol. 17, no. 1, pp. 1003-1016, 1979.
- [22] J. J. Murphy and C. R. Shaddix, "Soot Property Measurements in a Two Meter Diameter JP-8 Pool Fire," *Combustion Science and Technology*, vol. 178, no. 5, pp. 865-894, 2006.
- [23] Neutrium.net, "Concentration Conversions," Neutrium.net, 9 August 2012. [Online]. Available: https://neutrium.net/general_engineering/concentration-conversions/. [Accessed 9 June 2020].
- [24] M. M. Maricq and N. Xu, "The effective density and fractal dimension of soot particles from premixed flames and motor vehicle exhaust," *Journal of Aerosol Science*, vol. 35, no. 10, pp. 1251-1274, 2004.
- [25] R. Heus and E. Denhartog, "Maximum allowable exposure to different heat radiation levels in three types of heat protective clothing," *Industrial Health*, vol. 55, pp. 529-536, 2017.
- [26] ANSYS, *Lecture 06: Finite-rate combustion*, ANSYS, 2016.
- [27] S. B. Pope, *Turbulent Flows*, Cambridge University Press, 2000.
- [28] F. Nicoud and F. Ducros, "Subgrid-scale stress modelling based on the square of the velocity gradient tensor," *Flow, Turbulence and Combustion*, vol. 62, no. 3, pp. 183-200, 1999.
- [29] E. Vasquez and T. Eldredge, "Process modeling for hydrocarbon fuel conversion," in *Advances in Clean Hydrocarbon Fuel Processing*, Woodhead Publishing, 2011, pp. 509-545.

- [30] C. Doan, H. Le, S. Lower and S. Fraser U., "Gibbs (Free) Energy," Chemistry LibreTexts, 19 May 2020. [Online]. Available: [https://chem.libretexts.org/Bookshelves/Physical_and_Theoretical_Chemistry_Textbook_Maps/Supplemental_Modules_\(Physical_and_Theoretical_Chemistry\)/Thermodynamics/Energies_and_Potentials/Free_Energy/Gibbs_\(Free\)_Energy](https://chem.libretexts.org/Bookshelves/Physical_and_Theoretical_Chemistry_Textbook_Maps/Supplemental_Modules_(Physical_and_Theoretical_Chemistry)/Thermodynamics/Energies_and_Potentials/Free_Energy/Gibbs_(Free)_Energy). [Accessed 12 June 2020].
- [31] S. Gordon and B. J. McBride, "Computer Program for Calculation of Complex Chemical Equilibrium Composition, Rocket Performance, Incident and Reflected Shocks, and Chapman-Jouguet Detonations," National Aeronautics and Space Administration, Washington, D.C., 1976.
- [32] M. Bosenhofer, E.-M. Wartha, C. Jordan and M. Harasek, "The Eddy Dissipation Concept-Analysis of Different Fine Structure Treatments for Classical Combustion," *Energies*, vol. 11, no. 7, p. 1902, 2018.
- [33] H. Bao, "Development and Validation of a New Eddy Dissipation Concept (EDC) Model for MILD Combustion," in *Delft University of Technology*, Delft, 2017.
- [34] A. Gerasimov, *Quick Guide to Setting Up LES-type Simulations*, ANSYS , 2016.
- [35] Wikipedia, "2009 Jaipur fire," Wikipedia, March 2020. [Online]. Available: https://en.wikipedia.org/wiki/2009_Jaipur_fire. [Accessed 11 July 2020].

Appendix A. Theoretical background of computer models

A.1 Discretization

ANSYS Fluent is a finite volume based solver. It discretizes general scalar transport equations to algebraic equations through a control-volume-based method so that the equations can be solved numerically. The transport equations are then integrated within each controlled volume, resulting in a discrete equation in each cell. Discretizing the governing equations can be demonstrated with the transport equation of a scalar quantity φ . This equation is an unsteady conservation equation expressed in the integral form for a control volume V

$$\int_V \frac{\partial \rho \varphi}{\partial t} dV + \oint \rho \varphi \vec{v} \cdot d\vec{A} = \oint \Gamma_\varphi \nabla \varphi \cdot d\vec{A} + \int_V S_\varphi dV \quad (A.1)$$

ρ = density

\vec{v} = velocity vector

\vec{A} = Surface area vector

Γ_φ = diffusion coefficient for φ

$\nabla \varphi$ = gradient of φ

S_φ = source of φ per unit volume

After discretization, Eq. A.1 is expressed as

$$\frac{\partial \rho \varphi}{\partial t} V + \sum_f^{N_{faces}} \rho_f \vec{v}_f \varphi_f \cdot \vec{A}_f = \sum_f^{N_{faces}} \Gamma_\varphi \nabla \varphi_f \cdot \vec{A}_f + S_\varphi V \quad (A.2)$$

N_{faces} = number of faces enclosing cell

φ_f = value of φ convected through face f

$\rho_f \vec{v}_f \cdot \vec{A}_f$ = mass flux through the face

\vec{A}_f = area vector of face

$\nabla \varphi_f$ = gradient of φ at face f

V = cell volume

Eq. A.2 is the equation that's applied in each cell. The first term on the LHS is the temporal discretization term and is defined in Appendix A.1.2 [8].

A.1.1 Spatial discretization

ANSYS Fluent stores the discrete value only at the center of a cell. However, the face value is needed in order to execute the calculation, as can be seen from Eq. A.2. This can be demonstrated in the figure below, where the location of cell center is shown as c_0 and c_1 , and the location of face value is shown as f in Figure 61 below.

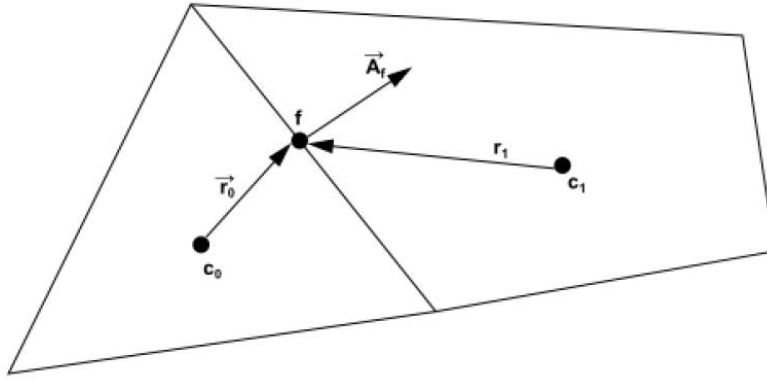


Figure 61: Illustration of discretization of a scalar transport equation

The face value must be interpolated from the cell center. This is achieved through upwinding, meaning that the face value is interpolated from a cell that's upstream, or “upwind”. Multiple schemes are available in Fluent for this purpose [8].

A.1.1.1 Bounded central differencing scheme

The bounded central differencing scheme is based on the central differencing scheme, which calculates the face value φ_f with the expression:

$$\varphi_{f,CD} = \frac{1}{2}(\varphi_0 + \varphi_1) + \frac{1}{2}(\nabla\varphi_0 \cdot \vec{r}_0 + \nabla\varphi_1 \cdot \vec{r}_1) \quad (A.3)$$

the indices 0 and 1 refer to the cells, same as shown in Figure 61. Cell 0 and 1 share the same face f . The vector \vec{r} is the vector that originates from the cell center and ends at the center of face f .

The central differencing scheme is known to produce unbounded solutions which leads to instability in the system. The model corrects this issue with the following expression:

$$\varphi_f = \varphi_{f,UP} + (\varphi_{f,CD} - \varphi_{f,UP}) \quad (A.4)$$

where the subscript UP denotes upwind. In this expression, the first term is treated implicitly, and the second term is treated explicitly.

The bounded central differencing scheme is a blend of the central differencing scheme and the first-order upwind scheme. The central differencing scheme itself is also a blend of central differencing and the second-order upwind scheme, as can be seen in Eq. A.4 [8].

A.1.1.2 QUICK scheme

The QUICK scheme can be used when both faces and cells of upstream and downstream can be identified. The following figure shows an arbitrary one-dimensional control volume to aid the explanation [8]:

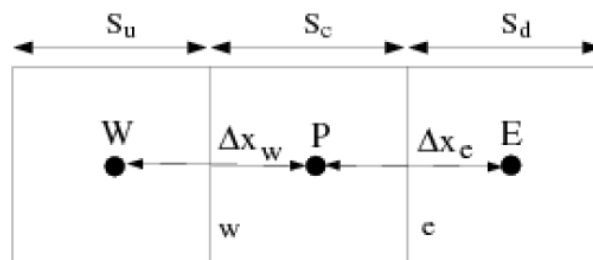


Figure 62: Illustration of a control volume consisting of both upstream and downstream

Assuming that the flow goes from left to right, the QUICK scheme calculates the face value at face e with the following equation:

$$\varphi_e = \theta \left[\frac{S_d}{S_c + S_d} \varphi_P + \frac{S_c}{S_c + S_d} \varphi_E \right] + (1 - \theta) \left[\frac{S_u + 2S_c}{S_u + S_c} \varphi_P - \frac{S_c}{S_u + S_c} \varphi_W \right] \quad (A.5)$$

The first term is a central interpolation, and the second term is the weighted average of second-order-upwind of the variable. When $\theta=1$, the expression is a central interpolation scheme. When $\theta=0$, the expression is a second-order-upwind scheme. θ is normally set to 1/8 in Fluent to avoid solution extrema [8].

A.1.2 Temporal discretization: bounded second-order implicit time integration

Any scalar quantity φ can be discretized in time using the following expression:

$$\frac{\partial \varphi}{\partial t} = \frac{\varphi_{n+\frac{1}{2}} - \varphi_{n-\frac{1}{2}}}{dt} \quad (A.6)$$

$$\varphi_{n+\frac{1}{2}} = \varphi_n + \frac{1}{2} \beta_{n+\frac{1}{2}} (\varphi_n - \varphi_{n-1}) \quad (A.7)$$

$$\varphi_{n-\frac{1}{2}} = \varphi_{n-1} + \frac{1}{2} \beta_{n-\frac{1}{2}} (\varphi_{n-1} - \varphi_{n-2}) \quad (A.8)$$

where the n , $n+1/2$, $n-1/2$, $n-1$, $n-2$ subscripts represent different time levels. The $\beta_{n+\frac{1}{2}}$ and $\beta_{n-\frac{1}{2}}$ are bounding variables for φ at the corresponding time level. Bounding variables could be different variables in different calculation such as the turbulence kinetic energy, dissipation rate, species mass fraction...etc [8].

A.2 LES simulation and the Wall-Adapting Local Eddy-Viscosity (WALE) model

Because of its unsteady nature, RANS simulation cannot capture the details of pool fire. This issue is also briefly discussed in chapter 4.2 where results have shown that RANS simulation is not appropriate for pool fires. In LES simulation, the large eddies are solved directly through the Navier-Stokes equation, and the small eddies are not solved, but modeled. This is done because the number of small eddies in a domain could become prohibitively many to be solved directly, especially close the walls in a domain. The LES simulation is a compromise between the RANS simulation, where eddies through the entire spectrum is modeled, and the DNS, where all eddies are solved.

Since only the large eddies are resolved in LES, the large eddies must be differentiated from the small eddies. The filtering process could be done either through Fourier (wave-number) space or configuration (physical) space. The filtering process can be expressed as the function below:

$$\bar{\phi}(x) = \int_D \phi(x') G(x, x') dx' \quad (A.9)$$

where ϕ is any variable, and the overbar represents the filtered variable. G is the function that determines the scale of filtering. The method used in Fluent is through physical space, which means that those eddies larger than the cell size in the domain are resolved, and those smaller are modeled. This is done by:

$$\bar{\phi}(x) = \frac{1}{V} \int_V \phi(x') dx', x' \in V \quad (A.10)$$

$$G(x, x') = \begin{cases} \frac{1}{V}, & x' \in V \\ 0, & x' \text{ otherwise} \end{cases} \quad (\text{A. 11})$$

V = volume of a computational cell

Similar to RANS where the Reynolds stresses arise during the averaging process, the subgrid stresses (SGS) arise when the filtering process is applied to the equation of conservation of momentum. This stress is unknown and needs to be modeled [27]. The subgrid stress tensor is defined to be

$$\tau_{ij} = \bar{\rho} \widetilde{u_i u_j} - \bar{\rho} \widetilde{\mu_i} \widetilde{\mu_j} \quad (\text{A. 12})$$

Fluent uses the Boussinesq hypothesis to compute the subgrid turbulent stresses, which is given as:

$$\tau_{ij} - \frac{1}{3} \tau_{kk} \delta_{ij} = -2\mu_t \overline{S_{ij}} \quad (\text{A. 13})$$

where μ_t is the subgrid-scale turbulent viscosity and $\overline{S_{ij}}$ is defined as:

$$\overline{S_{ij}} = \frac{1}{2} \left(\frac{\partial \bar{u}_i}{\partial x_j} + \frac{\partial \bar{u}_j}{\partial x_i} \right) \quad (\text{A. 14})$$

which is the deformation tensor for the resolved domain [28].

The model used to model the eddy viscosity in this project is the WALE model. The WALE model uses the following expression to model the eddy viscosity:

$$\mu_t = \rho L_s^2 \frac{(S_{ij}^d S_{ij}^d)^{\frac{3}{2}}}{(\overline{S_{ij} S_{ij}})^{\frac{5}{2}} + (S_{ij}^d S_{ij}^d)^{\frac{5}{4}}} \quad (\text{A. 15})$$

where L_s and S_{ij}^d are defined to be

$$L_s = \min \left(\kappa d, C_w V^{\frac{1}{3}} \right) \quad (\text{A. 16})$$

$$S_{ij}^d = \frac{1}{2} (\overline{g_{ij}^2} + \overline{g_{ji}^2}) - \frac{1}{3} \delta_{ij} \overline{g_{kk}^2}, \quad \overline{g_{ij}} = \frac{\partial \bar{u}_i}{\partial x_j} \quad (\text{A. 17})$$

$$C_w = 0.325$$

where κ is the von Karman constant, d is the closest distance to the wall, \bar{g} is a velocity gradient tensor, and δ_{ij} is the Kronecker symbol [8] [28].

There are a couple reasons why the WALE model is better than the Smagorinsky-Lily model, which is the simplest model available to model the eddy viscosity. In the WALE model, turbulent viscosity goes to zero at the wall, which is not the case for the Smagorinsky-Lily model. Secondly, the WALE model takes both the strain and rotation rates into account, while the Smagorinsky-Lily model only takes the strain rate into account. The WALE model hence agrees with recent findings more, where evidence has shown that the Smagorinsky-Lily model is not properly taking the energy dissipation on a global scale done by the turbulent structures into account [28].

A.3 The probability density function (PDF)

The turbulence-chemistry interaction (TCI) is modeled through a statistical approach called the probability density function for the nonpremixed combustion models in Fluent. During the

modelling of a combustion, the mixture fraction fluctuates with time. The PDF method is a way of quantifying how much fraction of time is the mixture fraction in a certain state. This is depicted in the plot below:

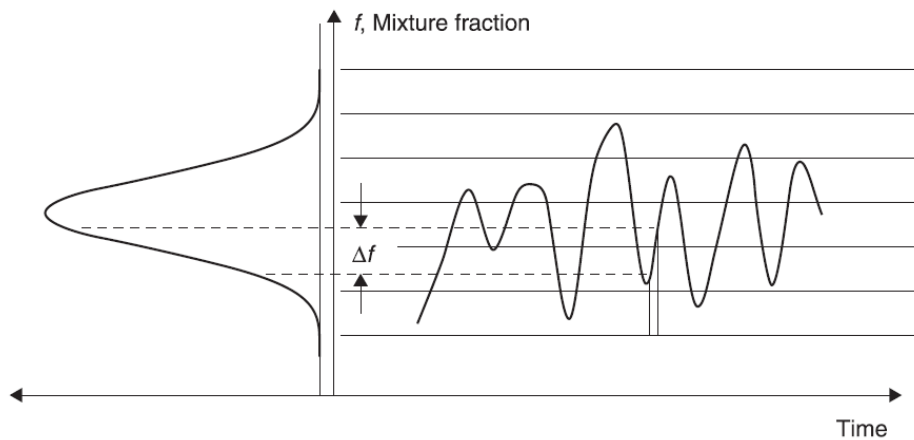


Figure 63: Illustration of probability density function

The right hand side of the plot shows the fluctuation of the mixture fraction, and the left hand side the probability distribution of this fluctuation. When the mixture fraction fluctuates, it would spend a certain fraction of time in the interval Δf . The PDF function $p(f)$ is then a function that expresses how much time the mixture fraction spends in this range.

In an adiabatic system, under the mixture fraction simplification, many scalar quantities such as the mass fraction of species, temperature, density...etc, are only a function of the mixture fraction. Since the PDF function is only a function of the mixture fraction, this means that these scalar values could be calculated solely from the mixture fraction through the PDF method. One biggest advantage of the PDF method is that, since the shape of the function is already assumed, the PDF could be pre-calculated even before the simulation starts. The PDF can then be stored in a look-up table, and the information could be retrieved during the simulation. This is extremely helpful in reducing the calculation time [29].

A.4 Chemical equilibrium model

The CE model calculates the chemical equilibrium of species through the method of Gibbs energy minimization. Gibbs energy is a way of quantifying the available energy in a system. If the Gibbs energy of a system is known, then the reaction that will happen in the system can be predicted. The definition of Gibbs energy is given below:

$$\Delta G = \Delta H - T\Delta S \quad (A.18)$$

ΔG = change in Gibbs energy

ΔH = change in enthalpy

$T\Delta S$ = (temperature) change in entropy

Assuming constant temperature and constant pressure, the direction of chemical reactions can be predicted. When the Gibbs energy is negative (exergonic), the reaction will proceed in the direction written. When it's positive (endergonic), the reaction will proceed in the reverse direction. When the Gibbs energy reaches zero, it means that the system has reached chemical equilibrium [30].

Gibbs energy depends only on the initial and end state of a system. This means that Gibbs energy carries no information regarding the mechanism of reactions, hence also no information

regarding the rate of reaction. This is the reason why the CE model in Fluent is able to perform calculation without any Chemkin code. The only information required is a thermo database, which includes information regarding the Gibbs energy of different species under different condition.

The software calculates the chemical equilibrium using the following expression [31]:

$$\delta G = \sum_{j=1}^n \left(\mu_j + \sum_{i=1}^l \lambda_i a_{ij} \right) \delta n_j + \sum_{i=1}^l (b_i - b_i^o) \delta \lambda_i = 0 \quad (\text{A.19})$$

μ_j = chemical potential (Gibbs free energy) per kg-mole of species j

λ_i = Lagrangian multipliers

a_{ij} = number of kg-atoms of element i per kg-moles of species j

δn_j = number of kg-moles of species j per kg of mixture

b_i = product of δn_j and a_{ij}

b_i^o = assigned number of kg-atoms of element i per kg of total reactants

The a_{ij} , δn_j , b_i , and b_i^o terms are the mass balance constraints in the expression.

As mentioned above, the CE model uses mixture fraction to represent all the chemical species available in the system. However, a method must be developed to reconcile the chemical equilibrium calculation and the mixture fraction. This method is called the Burke-Schumann solution [11].

$$T(Z) = \begin{cases} T_u(Z) + \frac{Q Y_{F,1}}{c_p v'_F W_F} Z, & Z \leq Z_{st} \\ T_u(Z) + \frac{Q Y_{O,2}}{c_p v'_{O_2} W_{O_2}} (1 - Z), & Z \geq Z_{st} \end{cases} \quad (\text{A.20})$$

T_u = initial condition in unburnt mixture

Q = heat of combustion

Y = mass fraction (subscript F and O_2 stand for fuel and oxidant)

c_p = specific heat

v' = stoichiometric coefficient

W = molecular weight

Z = mixture fraction

As can be seen from the expression, the temperature could be calculated just by knowing mainly the mixture fraction, and some other parameters, which could be derived from the mixture fraction. After the temperature is found, it is possible to look up the Gibbs energy available of the corresponding species in the thermo database. The Gibbs energy minimization calculation could be carried out from that point.

A.5 Steady diffusion flamelet model

A flamelet is a concept, where a thin layer of reactive-diffusive flame is placed in a turbulent field. The advantage of the SDF model is that non-equilibrium effects caused by the turbulence could be taken into account, while the complicated chemistry calculation is neglected, since the reactions are assumed to be fast and in equilibrium. For nonpremixed combustion, the flame surface is defined

by the nonreacting scalar, which is the mixture fraction Z . A nonpremixed jet diffusion flame can be seen in Figure 64

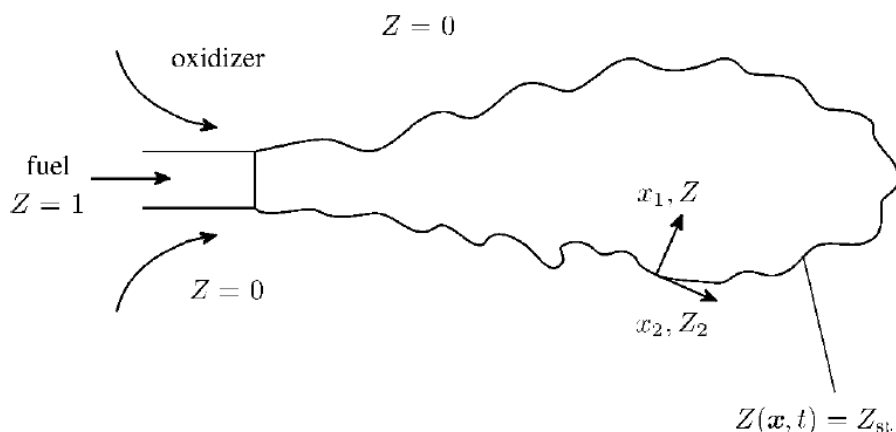


Figure 64: Stoichiometric mixture surface of a turbulent jet diffusion flame

where the flame surface is defined to be in stoichiometric mixture, which can be expressed as

$$Z(x, t) = Z_{st} \quad (A.21)$$

Close to this reactive-diffusing surface, the flamelet can be expressed in the equation

$$\rho \frac{\partial \psi_i}{\partial t} = \frac{\rho \chi}{Le_i} \frac{\partial^2 \psi_i}{\partial Z^2} + \omega_i \quad (A.22)$$

where

ψ_i = reactive scalars: mass fraction of all chemical species and temperature

Le_i = Lewis number

ω_i = chemical source term

χ = scalar dissipation rate

The scalar dissipation rate is expressed as

$$\chi = 2D|\nabla Z|^2 \quad (A.23)$$

where D is the thermal diffusivity. As can be seen, the flamelet equation is a function of the scalar dissipation rate [11]. In the flamelet equation, mixing is entirely controlled by the scalar dissipation rate. The scalar dissipation rate has the unit of an inverse time, which is the same as the strain rate. This indicates that the scalar dissipation rate is directly influenced by the strain rate, which is how the SDF model takes the nonequilibrium effects caused by turbulence into account [5].

The chemical source term ω_i in Eq. A.22 is expressed as

$$\omega_i = W_i \sum_{k=1}^r v_{ik} w_k \quad (A.24)$$

$$w_k = k_{fk} \prod_{j=1}^n \left(\frac{\rho Y_j}{W_j} \right)^{v'_{jk}} - k_{bk} \prod_{j=1}^n \left(\frac{\rho Y_j}{W_j} \right)^{v''_{jk}} \quad (A.25)$$

W_i = mean molecular weight

v_{ik} = stoichiometric coefficient

Y_j = mass fraction

k_{fk}, k_{bk} = rate of forward and backward reaction

The expression of the chemical source term shows the biggest difference between the CE and SDF model, which is the fact that the SDF model takes the chemical mechanism into account, hence requiring a Chemkin code input.

A.6 Eddy-dissipation concept model

Pool fires can also be modeled by solving the species transport equations. This is of course a lot more computationally expensive than modelling through the mixture fraction simplification. However, this is the method that takes the complete story into account, both in terms of mixing and chemical reactions.

When modelling pool fires with the EDC model, conservation equations for every chemical species are solved. This is done through the following equation:

$$\frac{\partial}{\partial t}(\rho Y_i) + \nabla \cdot (\rho \vec{v} Y_i) = -\nabla \cdot \vec{J}_i + R_i + S_i \quad (A.26)$$

R_i = net rate of production of species i by chemical reaction

S_i = rate of creation by addition from the dispersed phase plus any user-defined sources

Y_i = local mass fraction of each species

J_i = mass diffusion

For turbulent flows, ANSYS calculates the mass diffusion with the following expression [8]:

$$\vec{J}_i = -\left(\rho D_{i,m} + \frac{\mu_t}{Sc_t}\right) \nabla Y_i - D_{T,i} \frac{\nabla T}{T} \quad (A.27)$$

Sc_t = turbulent Schmidt number

μ_t = turbulent viscosity

D_t = turbulent diffusivity

The EDC model splits the domain into two regions: reacting and non-reacting. It assumes that reactions only occur within the small turbulent structures, or the fine scale as they are called here [32]. The length scale ξ^* and time scale τ^* of these fine scales are modeled as the following:

$$\xi^* = C_\xi \left(\frac{\nu \varepsilon}{k^2}\right)^{\frac{1}{4}} \quad (A.28)$$

$$\tau^* = C_\tau \left(\frac{\nu}{\varepsilon}\right)^{\frac{1}{2}} \quad (A.29)$$

k = turbulent kinetic energy

ε = rate of dissipation

ν = kinematic viscosity

C_ξ = volume fraction constant = 2.1377

C_τ = time scale constant = 0.4082

In LES simulation, k and ε represent sub-grid scale turbulent kinetic energy and rate of dissipation.

In the EDC model, the source term R_i is modeled as [33]:

$$R_i = \frac{\rho(\zeta^*)^2}{\tau^*[1 - (\zeta^*)^3]} (\tilde{Y}_i - Y_i^*) \quad (\text{A.30})$$

ζ^* = length scale of fine scale

τ^* = time scale of fine scale

Y_i^* = fine scale mass fraction

\tilde{Y}_i is the averaged reactants concentration that takes the mass concentration of both the fine scale and the surroundings into account, which has the following expression:

$$\tilde{Y}_i = (\zeta^*)^3 Y_i^* + [1 - (\zeta^*)^3] Y_i^o \quad (\text{A.31})$$

Y_i^o = surrounding mass fraction

The chemical reactions occur in the time scale τ^* and is governed by the equation provided below [8], which calculates the molar rate of creation or destruction of species i in reaction r ,

$$\hat{R}_{i,r} = \Gamma(v_{i,r}'' - v_{i,r}') \left(k_{f,r} \prod_{j=1}^N [C_{j,r}]^{\eta_{j,r}'} - k_{b,r} \prod_{j=1}^N [C_{j,r}]^{\eta_{j,r}''} \right) \quad (\text{A.32})$$

$C_{j,r}$ = molar concentration of species j in reaction r (kmol/m³)

$\eta_{j,r}'$ = rate exponent for reactant species j in reaction r

$\eta_{j,r}''$ = rate exponent for product species j in reaction r

$v_{j,r}'$ = stoichiometric coefficient for reactant species j in reaction r

$v_{j,r}''$ = stoichiometric coefficient for product species j in reaction r

$k_{f,r}$ = forward rate constant for reaction r

$k_{b,r}$ = backward rate constant for reaction r

After the molar concentration of species in the fine scales are calculated, and since the volume of the fine scale is known, the molar concentration of fine scale can be converted to mass fraction and plugged back into Eq. A.26.

A.7 Discrete ordinates model

The RTE solved by the DO model has the expression given below. This expression is meant for an absorbing, emitting, and scattering medium.

$$\nabla \cdot (I(\vec{r}, \vec{s}) \vec{s}) + (a + \sigma_s) I(\vec{r}, \vec{s}) = an^2 \frac{\sigma T^4}{\pi} + \frac{\sigma_s}{4\pi} \int_0^{4\pi} I(\vec{r}, \vec{s}') \Phi(\vec{s}, \vec{s}') d\Omega' \quad (\text{A.33})$$

where

\vec{r} = position vector

\vec{s} = direction vector

\vec{s}' = scattering direction vector

s = path length

a = absorption coefficient

n = refractive index

σ_s = scattering coefficient

σ = Stefan-Boltzmann constant ($5.669 \times 10^{-8} \text{ W/m}^2\text{-K}^4$)

I = radiation intensity, which depends on the position vector and direction vector

T = total temperature

Φ = phase function

Ω' = solid angle

$(a + \sigma_s)$ = optical thickness

This expression is solved for the mixture material in the DO model. The radiative properties of the different species are calculated through a volume fraction averaging based method [8].

A.8 Weighted sum of gray gas model

In the WSGGM, a single gray absorption coefficient is approximated with the expression:

$$\alpha = -\frac{\ln(1 - \varepsilon_m)}{s} \quad (\text{A.34})$$

where ε_m is the emissivity and s is the path length. The general expression for calculating the total emissivity ε over a distance s is given as follows,

$$\varepsilon_m = \sum_{i=0}^I a_{\varepsilon,i}(T)(1 - e^{-\kappa_i p s}) \quad (\text{A.35})$$

$$s = 3,6 \frac{V}{A} \quad (\text{A.36})$$

where

$a_{\varepsilon,i}$ = emissivity weighing factor for the i^{th} fictitious gray gas

κ_i = absorption coefficient for the i^{th} fictitious gray gas

p = sum of partial pressure of all absorbing gases

$(1 - e^{-\kappa_i p s})$ = gray gas emissivity for the i^{th} fictitious gray gas

V = volume of the domain

A = total surface area of the domain

In Fluent, only CO₂ and H₂O are taken into account for the emissivity calculation [8].

A.9 Moss-Brookes-Hall model

The Moss-Brookes-Hall model is an extension of the Moss-Brookes (MB) model, which solves the transport equation for the normalized radical nuclei concentration b_{nuc}^* and soot mass fraction Y_{soot} :

$$\frac{\partial}{\partial t}(\rho Y_{soot}) + \nabla \cdot (\rho \vec{v} Y_{soot}) = \nabla \cdot \left(\frac{\mu_t}{\sigma_{soot}} \nabla Y_{soot} \right) + \frac{dM}{dt} \quad (\text{A.37})$$

$$\frac{\partial}{\partial t}(\rho b_{nuc}^*) + \nabla \cdot (\rho \vec{v} b_{nuc}^*) = \nabla \cdot \left(\frac{\mu_t}{\sigma_{soot}} \nabla b_{nuc}^* \right) + \frac{1}{N_{norm}} \frac{dM}{dt} \quad (\text{A.38})$$

where

Y_{soot} = soot mass fraction

M = soot mass concentration

b^*_{nuc} = normalized radical nuclei concentration (particles* 10^{-15} /kg) = $\frac{N}{\rho N_{\text{norm}}}$

N = soot particle number density [particles/m³]

$N_{\text{norm}} = 10^{15}$ particles

Unlike the MB model which assumes the soot inception starts with acetylene (for methane flame) or a combination of acetylene and benzene (for higher hydrocarbon), the MBH model calculates the soot inception based on the formation rate of two-ringed (C₁₀H₇) and three-ringed (C₁₄H₁₀) aromatics, acetylene (C₂H₂), benzene (C₆H₆), and phenyl radical (C₆H₅). The soot inception rate has the following expression

$$\begin{aligned} \frac{dN}{dt} = & 8C_{\alpha,1} \frac{N_A}{M_P} \left[\rho^2 \left(\frac{Y_{C_2H_2}}{W_{C_2H_2}} \right)^2 \frac{Y_{C_6H_5} W_{H_2}}{W_{C_6H_5} Y_{H_2}} \right] \exp \left\{ -\frac{T_{\alpha,1}}{T} \right\} \\ & + 8C_{\alpha,2} \frac{N_A}{M_P} \left[\rho^2 \frac{Y_{C_2H_2}}{W_{C_2H_2}} \frac{Y_{C_6H_6} Y_{C_6H_5} W_{H_2}}{W_{C_6H_6} W_{C_6H_5} Y_{H_2}} \right] \exp \left\{ -\frac{T_{\alpha,2}}{T} \right\} \quad (A.39) \\ C_{\alpha,1} = & 127 \times 10^{8,88} [s^{-1}] \\ C_{\alpha,2} = & 178 \times 10^{9,50} [s^{-1}] \\ T_{\alpha,1} = & 4378 [K] \\ T_{\alpha,2} = & 6390 [K] \end{aligned}$$

M_P is the mass of incipient soot particle, which is assumed to be 1200 [kg/kmol] in the MBH model. This is because the model assumes soot particles are composed of 100 carbon atoms. Soot mass density is assumed to be 2000 [kg/m³]. N_A is the Avogadro number, which is $6,022045 \times 10^{26}$ [kmol⁻¹].

The source term for the soot mass concentration is modelled with the following expression

$$\begin{aligned} \frac{dM}{dt} = & M_P C_{\alpha} \left(\frac{X_{\text{prec}} P}{RT} \right)^l \exp \left\{ -\frac{T_{\alpha}}{T} \right\} + C_{\gamma} \left(\frac{X_{\text{SGS}} P}{RT} \right)^m \exp \left\{ -\frac{T_{\gamma}}{T} \right\} \left[(\pi N)^{1/3} \left(\frac{6M}{\rho_{\text{soot}}} \right)^{2/3} \right]^n \\ & - C_{\text{oxid}} C_{\omega,1} \eta_{\text{coll}} \left(\frac{X_{\text{OH}} P}{RT} \right) \sqrt{T} (\pi N)^{1/3} \left(\frac{6M}{\rho_{\text{soot}}} \right)^{2/3} \\ & - C_{\text{oxid}} C_{\omega,2} \left(\frac{X_{\text{O}_2} P}{RT} \right) \exp \left\{ -\frac{T_{\omega,2}}{T} \right\} \sqrt{T} (\pi N)^{1/3} \left(\frac{6M}{\rho_{\text{soot}}} \right)^{2/3} \quad (A.40) \end{aligned}$$

C_{α} = model constant for soot inception rate = 54 [s⁻¹]

C_{β} = model constant for coagulation rate = 1.0 [s⁻¹]

C_{γ} = surface growth rate scaling factor = 9000.6 [kg-m-kmol⁻¹-s⁻¹]

$C_{\omega,1}$ = oxidation model constant = 105.81 [kg-m-kmol⁻¹-K^{-1/2}-s⁻¹]

$C_{\omega,2}$ = oxidation model constant = 8903.51 [kg-m-kmol⁻¹-K^{-1/2}-s⁻¹]

C_{oxid} = oxidation rate scaling parameter = 1

T_{α} = activation temperature of soot inception = 21000 [K]

$T_\gamma =$ activation temperature of surface growth rate = 12100 [K]

$T_{\omega,2} = 19778$ [K]

$\eta_{coll} =$ collisional efficiency parameter = 0.13

The first term accounts for nucleation, second term surface growth. The third and fourth term takes the oxidation into account, one for the oxidation caused by OH, and the other by O₂, respectively [8].

Appendix B. Code of user defined function

B.1 Hooking PMAC of methanol

The plot of PMAC of methanol as a function of temperature is shown in Figure 20(b) in chapter 4.5. This curve is broken down to two segments at 350 [K] and two polynomials are fit to these two segments. These two polynomials are then used in the code in order to represent the curve more accurately. As can be seen in the code, when the temperature is below 350 [K], the first polynomial is used to calculate the PMAC of methanol. When the temperature is above 350 [K], the other one is used. All the k variables represent the constants in these polynomials.

```
#include "udf.h"
#include "materials.h"
#include "pdf_props.h"
#include "pdf_table.h"

DEFINE_WSGGM_ABS_COEFF(user_methanol_PMAC_me, c, t, xi, p_t, s, soot_conc, Tcell, nb, ab_wsggm, ab_soot)
{
    #define SpNo 20

    #if !RP_HOST
    Material *m = THREAD_MATERIAL(t);

    int id_ch3oh = mixture_specie_index(m, "ch3oh");
    real CH3OH_molf;
    real user_methanol_PMAC;
    double x[SpNo], y[SpNo];
    real k1, k2, k3, k4, k5;

    k1 = 0.0001;
    k2 = 0.395;
    k3 = 5e-7;
    k4 = 0.0011;
    k5 = 0.7907;

    Pdf_XY(c,t,x,y);
    CH3OH_molf = x[id_ch3oh];

    /*polynomial for T between 300-350*/
    if (C_T(c,t) < 350) {
        user_methanol_PMAC = p_t*CH3OH_molf*(k1*C_T(c,t)+k2)*101.325;
    }
    /*polynomial for T between 350-1400*/
    else {
        user_methanol_PMAC = p_t*CH3OH_molf*(k3*pow(C_T(c,t),2)-k4*C_T(c,t)+k5)*101.325;
    }

    *ab_wsggm += user_methanol_PMAC;

    #endif
}
}
```

Figure 65: User defined function for adding PMAC of methanol

B.2 The HE model

```
#include "udf.h"
#include "materials.h"
DEFINE_WSGGM_ABS_COEFF(user_wsggm_abs_coeff, c, t, xi, p_t, s, soot_conc, Tcell, nb, ab_wsggm, ab_soot)
{
    #if !RP_HOST
    Material *m = THREAD_MATERIAL(t);

    int ico2 = mixture_specie_index(m, "co2");
    int ico = mixture_specie_index(m, "co");
    real CO2_massf, CO_massf;
    real k1, k2, k3, k4;
    real b1, bT;
    real ysoot;
    real u;
    real asoot;

    k1 = 0.042;
    k2 = 2.83;
    k3 = k1 / k2;
    b1 = 1232.4;
    bT = 4.8e-4;
    k4 = 44/28;

    /*
    Message("ico2=%d",ico2);
    Message("ico=%d",ico);
    */

    CO2_massf = Pdf_Yi(c,t,ico2);
    CO_massf = Pdf_Yi(c,t,ico);

    ysoot = k3*CO2_massf + k3*k4*CO_massf;

    asoot=b1*C_R(c,t)*ysoot*( 1.0+bT*( C_T(c,t)-2000.0 ));

    /*
    Message(" CO2_massf= %E \n C_R= %E \n ysoot=%E \n asoot=%E \n awsggm=%E \n",CO2_massf,C_R(c,t),ysoot,asoot,ab_wsggm);
    */
    *ab_wsggm +=asoot;
    /*
    Message(" awsggm2=%E \n",ab_wsggm);
    */
    #endif
}
```

Figure 66: User defined function for the HE model